Study of the Structural, Magnetic and Electric Properties of Al Substituted NiCuCd Ferrite Nanoparticles

By

Md. Abdul Mannan

A thesis submitted in partial fulfillment of the requirement

for the degree of

MASTER OF PHILOSOPHY IN PHYSICS

DEPARTMENT OF PHYSICS

Chittagong University of Engineering & Technology, Chattogram-4349, Bangladesh

2022

CERTIFICATION

CANDIDATE'S DECLARATION

Declaring that this thesis or any portion of it has not submitted to another institution for the award of a degree or diploma.

_____

(**Md. Abdul Mannan**)

CONTENTS

CHAPTER 4

Experimental Techniques

CHAPTER 5

Results and Discussion

List of Figures

List of Tables

Nomenclature

M	*Magnetization*
M_s	*Saturation magnetization*
H	*Magnetic field*
H_c	*Coercive force*
μ_B	*Bohr magneton*
( )	*Tetrahedral or A-site*
[ ]	*Octahedral or B-site*
θ	*Diffraction angle*
$F(\theta)$	*Nelson-Riley function*
N_A	*Avogadro's number*
a_o	*Lattice constant*
a	*Lattice parameter*
M_W	*Molecular weight*
β_{meas}	*Observed full width at half maximum*
β_o	*Instrumental broadening*
D_{hkl}	*Crystallite size*
D	*Average grain diameter*
ε_o	*Free space permittivity*
ε^*	*Complex dielectric permittivity*
$\varepsilon^/$	*Dielectric constant*
$\varepsilon^{//}$	*Imaginary part of complex permittivity*
$tan\,\delta$	*Dielectric loss tangent*
M^*	*Complex electric modulus*
$M^/$	*Real part of electric modulus*
$M^{//}$	*Imaginary part of electric modulus*
C	*Capacitance*
β	*Full width at half maximum*
VSM	*Vibrating sample magnetometer*
FESEM	*Field emission scanning electron microscope*
XRD	*X-ray diffraction*
PVA	*Poly vinyl alcohol*
Q	*Relative quality factor*
n_B	*Number of magnetic moments*
$Z^{//}$	*Imaginary part of complex impedance*
$Z^/$	*Real part of complex impedance*
Z^*	*Complex impedance*
σ_{AC}	*AC conductivity*
ρ_{AC}	*AC resistivity*
ρ_{DC}	*DC resistivity*

ACKNOWLEDGMENTS

I thank Almighty Allah with all my heart for the accomplishment of this kind of study job.

I am incredibly grateful to Professor Dr. Mohammad Belal Hossen of the Physics Department at CUET, who is my supervisor, for his unwavering support, several discussions, understanding suggestions, vast knowledge, and ultimately for helping design and form the ferrite nanomaterials that are the subject of this dissertation. He is a passionate physicist, and I had the honor of studying both research methods and fundamental physics from him. He is not only my supervisor but also a friend. His unbelievable motivation and guidance helped me to continue and complete my degree.

I want to express my gratitude to the other members of my examination committee for their support and insightful recommendations.

I want to pay special thanks to Professor Dr. Swapan Kumar Roy, Head, Department of Physics, CUET who guided and suggested me positively throughout my degree. I also want to thank Professor Dr. Faruque-Uz-Zaman Chowdhury and Professor (Ret.) Dr. Abdur Rashid from the Department of Physics of CUET.

Additionally, I would like to extend my gratitude to all of the other professors in the Physics Department, CUET paying special thanks to Professor Dr. H.M.A.R. Maruf and Ms. Arjumanara Bagum, Assistant Professor to suggest and help me positively.

I am grateful to Mr. Md. Sohel Rana Technical Officer, CUET postgraduate lab in the Physics Department for his cooperation at the time of sample preparation and for using the Impedance Analyzer.

The Chittagong University of Engineering and Technology's CHSR is funding the current project. This assistance is also recognized. This work is also supported by the Functional Nanomaterials Research Group, Department of Physics, CUET.

Abstract

A series of $Ni_{0.5}Cu_{0.2}Cd_{0.3}Fe_{2-x}Al_xO_4$ (where x = 0.0 to 0.075 in step of 0.015) nanoparticles have been synthesized by sol-gel technique which are further annealed at 700^oC. X-ray diffraction (XRD) and field emission scanning electron microscopy (FESEM) techniques have used to examine the structural and surface morphology of all produced materials. A vibrating sample magnetometer with an applied field of 1.5 T (in $\mu_0 H$) is used to measure the magnetic (hysteresis) characteristics of these ferrite nanoparticles. Using a Wayne Kerr impedance analyzer and the two probe approach, the electrical and dielectric properties have examined in the frequency range of 20 Hz to 15 MHz. The electric conduction mechanism and the resistances at the grain boundaries in ferrite nanoparticles have studied using complicated impedance and modulus spectroscopy techniques. All samples have showed single-phase cubic spinel structures, according to XRD analysis, which shows peaks with greater sharpness and width. Scherrer's formula and FESEM data have used to calculate the crystallite sizes. On the other hand, the results of the Rietveld analysis have used to determine the cation distribution and other structural factors. Maxwell-Wagner space charge polarization and Koop's phenomena have used to explain the low-frequency dispersion behavior of dielectric properties and their consistency in high-frequency domain. It is worth mentioned that the conductivity phenomena show good agreement with dielectric behavior of the synthesized nanomaterials. Cole-Cole plot has used to separate the contribution of grain resistance and grain boundary resistance with observing the predominance of grain boundary resistance. Theories that already exist have used to discuss potential relationships between structural, magnetic, electrical, and dielectric properties.

Chapter 1

Introduction

1.1 Introduction

Ferrites are non-conductive ferrimagnetic compounds. It is generally originated from Fe oxides like as Fe_3O_4 or Fe_2O_3 and other metals oxides. The study of magnetism is the main emphasis in the new era of the nano-scale world. The nano-world needs to reduce the large magnetic circuits to integrate magnetic performance with other characteristics. The main opportunities for ferrite nanoparticles are size and physicochemical behaviors. The synthesis of nanoparticles demands high importance due to their versatile applications in the fields of material science, biomedical, biotechnology, engineering etc. [1-4]. Magnetic spinel ceramics, nickel-containing ferrites have been successfully manufactured and their characterization was widely done because of their enormous multifunctional applications due to their comparatively higher inductive property at higher frequency regions, reasonably low demagnetizing as well as dielectric losses and obviously lower electrical conductivity [5]. Considering research in these fields, a recognized truth could be concluded that when a magnetic cation is substituted by a non-magnetic cation (Here Al^{3+}), it diluted their exchange interaction in addition to the influence of structural, magnetic and electrical characters of every composition. For instance, the light substitution of Fe^{3+} by Al^{3+} in Ni-Cu-Cd ferrites increases both saturation magnetization and electrical resistivity with lower dielectric losses and thereby remarkably increased both electrical and magnetic properties of the ceramics for some optimum compositions [4,7]. Many researchers studied the magnetic characteristics of Ni-Cu-Zn based nanocrystals but for the Ni-Cu-Cd containing properties, which become alternate candidates, are seldom noted [5].

The behavior of ferrite materials can be changed by the chemical composition, substituent, synthesis technique, temperature, etc. and substitution of nonmagnetic Al shows unique characteristics for its (Al^{3+}) inert gas configuration observed by many researchers [6–8]. According to them [6–8], the substitution of a small amount of Al increases both resistivity and magnetization and decreases the dielectric-anisotropy constant. The sol-gel technique is expected to fabricate magnetic nanoparticles. The main attraction of the formation of homogeneous magnetic nanoparticles with their physical properties and controllable size which encouraged the synthesis of excellent magnetic nanoparticles of different compositions with improved quality in terms of phase, nanostructure, magnetization and resistivity etc. The outcome of this research will be essential for technologist and scientists to manufacture various devices for high-frequency applications.

1.2 Literature Reviews

Recently, Kumer et al. [9] reported that ferrites also show like multiferroic properties. There are many researchers who studied the magnetic properties of Ni-Cu-Zn based ferrites but for the Ni-Cu-Cd containing properties, which become alternate candidate are seldom reported [10].

The properties of ferrites can be tuned by the chemical compositions, substituents, synthesis techniques, temperature, etc. and substitution of nonmagnetic Al shows some unique properties due to its (Al^{3+}) noble-gas structure [11–13]. Many researchers [11–13] reported that, light substitution of Al enhanced magnetization, resistivity as well as reduce anisotropy constant, non-stoichiometric ratio, formation of ferrous (Fe^{2+}) ions, dielectric and eddy current losses [14].

Investigation on the basic properties i.e. structural, magnetic and electric properties of

Ni-Cd-Al, Ni-Cu-Zn-Al, Ni-Cu-Cd ferrites are reported by many researchers [14-16]. Batoo et al. [15] synthesized single-phase $Ni_{0.2}Cd_{0.3}Fe_{2.5-x}Al_xO_4$ nanoparticles through sol gel technique. The complex impedance spectra showed dominance of grain boundary resistance. Belavi et al. [16] studied $Ni_{0.95-x}Cd_xCu_{0.05}Fe_2O_4$ and found that M_s increases with Cd content up to x= 0.3. Belal et al. [17] synthesized single-phase $Ni_{0.27}Cu_{0.10}Zn_{0.63}Fe_{2-x}Al_xO_4$ nanoparticles through auto combustion technique. The complex impedance spectra [17] showed dominance of grain boundary resistance and successfully explained the contribution of grain-grain boundary resistance. The contribution of grain resistance to the high frequency region reduces eddy current losses and this property is technologically important for high frequency applications. M. Arifuzzaman, an M. Phil. student successfully synthesized $Ni_{0.7-x}Cu_xCd_{0.3}Fe_2O_4$ ferrite nanoparticles and obtained optimum properties for Cu content x = 0.2.

In this research, sol-gel technique has been used to synthesize $Ni_{0.5}Cu_{0.2}Cd_{0.3}Fe_{2-x}Al_xO_4$ nano particles annealed at 700^{o}C and to study of their electrical and magnetic properties by different experimental techniques such as XRD, dielectric spectra, impedance and modulus spectroscopy, magnetic hysteresis using vibrating sample magnetometer technique.

1.3 Objectives with specific aims and possible outcome

The main objectives of the present research are as follows:

- Synthesis of $Ni_{0.5}Cu_{0.2}Cd_{0.3}Fe_{2-x}Al_xO_4$ (x = 0.00, 0.015, 0.03, 0.045, 0.06, 0.075) ferrite nanoparticles.
- To perform structural characterization of various compositions by x-ray diffraction (XRD).
- Study of the surface morphology and nanostructure (grain size).

- To observe variation of saturation magnetization (M_s) for various composition using Vibrating Sample Magnetometer.
- To investigate frequency-dependent electric and dielectric properties such as complex dielectric constant, ac conductivity, and analysis of complex impedance spectra (Cole-Cole plot) of different compositions.

Possible outcome of the research is as follows:

Sol gel technique is expected to fabricate magnetic nanoparticles. The major interest in the synthesis of uniform magnetic nanoparticles with controllable size and their physical properties has stimulated a search for general schemes to prepare high-quality magnetic nanoparticles of varying compositions and hence materials are expected with better quality in terms of phase pure synthesis, magnetization and resistivity. The results will be helpful for scientists and engineers to manufacture various devices for high-frequency applications.

1.4 Organization of the Thesis

The thesis has been organized in the following way:

Chapter–1 presents a brief introduction of Ni-Cu-Cd and Al based nano-crystalline ferrites, brief of previous works and organization of the thesis.

Chapter–2 deals with detailed theoretical background to study this type of research work. We have classified and described the magnetization term along with class of different materials. Detail in this chapter incorporates background information to assist in understanding the aims and objectives of this investigation, and also reviews recent reports by other investigators with which these results can be compared.

Chapter–3 incorporates with the detail of sample synthesis.

Chapter–4 contains the details of experimental techniques.

Chapter–5 describes the results and discussion of all studies.

Chapter-6 includes the conclusions drawn from the overall experimental results and discussion along with the scopes of future work.

A concise list of publications and conferences related to present research work has been presented at the end.

References:

[1] S. Odenbach, K. H. J. Buschow, Handbook of Magnetic Materials, vol. 16, Amsterdam, North-Holland (2006) 127.

[2] P. Tartaj, M. D. D. Morales, S. Veintemillas-Verdaguer, T. Gonzalez-Carreno, C. J. Serna, J. Phys. D: Appl. Phys. 36 (2003) R182.

[3] M. Faraji, Y. Yamini, M. Rezaee, J. Iran. Chem. Soc. 7 (2010) 1.

[4] C. M. Niemeyer, Angew. Chem. Int. Ed. 40 (2001) 4128.

[5] D. K. Pradhan, Pankaj Misra, Venkata S. Puli, Satyaprakash Sahoo, D. K. Pradhan, Ram S. Katiyar, J. Appl. Phys. 115 (2014) 243904.

[6] A. A. Sattar, H. M. El-Sayed, M. M. El-Tabey, J. Mater. Sci. 40 (2005) 4873.

[7] I. Maghsoudi, H. Shokrollahi, M. J. Hadianfard, J. Amighian, Powder Technol. 235 (2013) 110.

[8] I. H. Gul, Erum Pervaiz, Mater. Res. Bull. 47 (2012) 1353.

[9] K. M. Batoo, S. Kumar, C. G. Lee, Alimuddin, J. Alloy. Compd. 480 (2009) 596.

[10] D. K. Pradhan, Pankaj Misra, Venkata S. Puli, Satyaprakash Sahoo, D. K. Pradhan, Ram S. Katiyar, J. Appl. Phys. 115 (2014) 243904.

[11] A. A. Sattar, H. M. El-Sayed, M. M. El-Tabey, J. Mater. Sci. 40 (2005) 4873.

[12] I. Maghsoudi, H. Shokrollahi, M. J. Hadianfard, J. Amighian, Powder Technol. 235 (2013) 110.

[13] I. H. Gul, Erum Pervaiz, Mater. Res. Bull. 47 (2012) 1353.

[14] M. Belal Hossen, A. K. M. Akther Hossain, J. Magn. Magn. Mater. 387 (2015) 24.

[15] K. M. Batoo, S. Kumar, C. G. Lee, Alimuddin, Curr. App. Phys. 9 (2009) 826.

[16] P. B. Belavi, G. N. Chavan, B. K. Bammannavar, L. R. Naikand R. K. Kotnala, AIP Conf. Proc. 1349 (2011) 1250.

[17] M. Arifuzzaman, M. Belal Hossen, Results in Physics 16 (2020) 102824.

Chapter 2

Background

2.1 Brief History of Magnetism

The term magnetism comes from the word ‘magnesia,' which refers to an island in the Aegean Sea (a portion of the Mediterranean Sea) where Greeks discovered specific stones around 470 B C. One of the most notable peculiar qualities of these stones (lodestones, i.e. lead to) is their ability to attract iron fragments. In the twelfth century, magnets were first used to make compasses, and Chinese people utilized it for navigation. Artificial magnets were made by William Gilbert made by means of rubbing iron pieces against lodestones. Due to the self-magnetic characteristics of the earth, it was discovered in the sixteenth century that a compass always points north-south. John Michell, a British scientist, discovered in 1750 that magnetic poles follow the inverse-square law, and Charles Coulomb confirmed his findings [1]. An electric current can produce a magnetic field [2], which was the great discovery of Hans Christian Oersted in 1820 and then the first electromagnet was made in 1825. The scientific community then learned from Bergmann, Becquerel, and Faraday's discoveries that all matter, including liquids and gases, is affected by magnetism, though only a small number of them react to a noticeably notable amount. Magnets are widely used in both the home and office, and their functions range from holding photos on the refrigerator to generating torque in power-driven motors. The general properties of magnets are well known to most of the people, but the source of magnetism is familiar only to the scientific community. To comprehend the conventional understanding of magnetism, it is crucial to understand both the terms magnetic field and dipole. Energy is a substance found in magnetic fields and is essentially described as a volume of space in which an energy transition takes place. We can detect and measure this Physical systems migrate toward configurations with lower energy

levels, and we can observe and measure this shift in energy inside that volume of space. A magnetic pole is the point on a substance where a magnetic field can be felt escaping or entering. The term "dipole" refers to a pair of equal and opposite electric charges or magnetic poles that are spaced apart by a modest amount. There have never seen any single instances of magnetic poles; they are always discovered in pairs. In the presence of magnetic fields, magnetic dipoles undergo torque. A bar magnet is a good example of a dipole where north and south poles exist in two opposite ends. When a magnet is divided in half, two new magnets or dipoles are produced from the original. Up to the atomic level, this segmentation and the production of dipoles can continue. As a result, the fundamental unit of matter (atom) is where magnetism comes from.

2.2 Effect of Nanostructured Materials

Nanotechnology includes the exploitation and utilization of nanostructured materials and devices. Materials having dimensions ranging from a few nm to 100 nm are usually referred to as nanocrystalline materials [3]. Any form of nanomaterial shape is possible, including spherical dots, rods, tubes, plates, and thin films [4]. The structural, chemical and electromagnetic properties can be changed surprisingly when the dimensions of any materials are reduced to nm size from their bulk sizes [5]. The difference between the properties of nano-structured materials and their bulk counterpart is explained on the basis of the high surface-to-volume ratio and the interaction of atoms lying at the surface, which is one important property of a nano-structured material compared to bulk materials [6].

In recent years, research on nano-crystalline materials has remained active work [7, 8]. Diffusivity, mechanical strength, sintering temperature, alloying capability, and plasticity are the most crucial size-dependent physical features of nanomaterials.

Additionally, the electro-magnetic characteristics of nanocrystalline materials, which are very size dependant, include resistivity, dielectric loss tangent, dielectric constant, saturation magnetization, coercivity, and relative permeability. Controlling the structure and content of nanocrystalline materials can therefore greatly enhance the performance of the final product.

2.3 Magnetism and the Source of Magnetism

Physical processes that are mediated by magnetic fields are referred to as electromagnetic phenomena, one of which is magnetism. All materials are susceptible to magnetism, albeit some are more so than others. The strongest effects are seen in permanent magnets constructed of iron-based materials. All materials are made up of atoms which are composed of electrons, protons and neutrons. Since electrons are constantly moving around the core, massive positive nucleus, which is made up of protons and neutrons, and carries a negative electrical charge, they can produce a magnetic field.

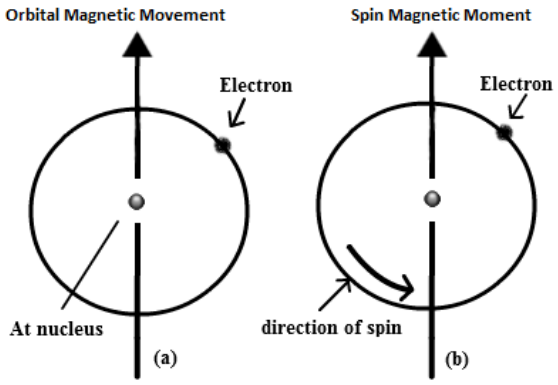

Fig.2.1. Demonstration of the magnetic moment associated with (*a*) an orbiting electron and (*b*) a spinning electron [9].

The magnitude of this magnetic field can be used to compute the magnetic moment. An electric charge in motion results in the creation of a magnetic field. Similar to the electric field, the magnetic effect can be attributed to so-called magnetic dipoles in a permanent magnet or be traced back to electrical currents that are flowing (Oersted, 1819).

Consequently, both the electron magnetic moment and the spin magnetic moment of elementary particles are the sources of magnetism. A magnetic moment is caused by an electron's magnetic moment, which is influenced by its intrinsic spin and charge characteristics and is depicted in figure 2.1.

As a result, the electron spin and currents related to the electrons' orbital motion are the two sources of the atomic magnetic moment [10] and the spin-orbit interaction connects them. In a magnetic field, free electrons travel in cyclotron orbits whereas bound electrons experience Larmor precession, which results in orbital diamagnetism. The explanation of magnetism in solids is fundamentally different depending on whether the electrons are concentrated in ion cores or delocalized in energy bands. The free-electron model is seen to be the best place to start for describing magnetism in metals, leading to Pauli paramagnetism and Landau diamagnetism that are temperature independent. On the other hand, isolated, non-interacting electrons show Curie paramagnetism.

The magnetic qualities of significant that are mostly attributable to the atom's electrons, and the mobility of the electrons causes the creation of magnetic moments. Although the nucleus also has a little magnetic moment, it is negligible in comparison to the electron's and has no impact on the overall magnetic properties. The magnetic moments of the nuclei are typically thousands of times smaller than those of the electrons, and as a result, the effects of the nuclear magnetic moments on the magnetization of materials are much smaller than those in other contexts, primarily nuclear magnetic resonance and magnetic resonance imaging.

In general, an ion with an even number of electrons cancels its spins or moments while an ion with an odd number of electrons has uncompensated spins. For example, the trivalent Fe ion has a moment that is equal to five uncompensated spins, as illustrated in Fig. 2.2. [11].

	K	Ca	Sc	Ti	V	Cr	Mn	Fe	Co	Ni	Cu	Zn
4s	↑	↑↓	↑↓	↑↓	↑↓	↑	↑↓	↑↓	↑↓	↑↓	↑	↑↓
3d	-	-	1	2	3	5	5	5	5	5	5	5
	-	-	-	-	-	-	-	1	2	3	4	5
Net (3d)	-	-	1	2	3	5	5	4	3	2	0	0

Fig. 2.2: The 4s orbital fills before the 3d orbital when a new proton is added to the nucleus in isolated atoms with unbalanced magnetic spins.

Thus, a magnetic field interacts with electrons in such a way as to induce a magnetic moment, which opposes the applied magnetic field.

2.4 Magnetic Materials

Any substance that can be magnetized by the application of an external magnetic field is considered to be a magnetic material. The orbital and spin motions of the electrons within each material's atom are related to its magnetic characteristics. When a magnetic field is applied, magnetic materials can be categorized according to differences in their internal and external flux and changes in their magnetization M or magnetic induction B. M and B are connected to H by two numbers: the permeability χ and susceptibility μ

$$\chi = M/H \text{ and } \mu = B/H$$

In SI system, the permeability μ defines units of henry/m. Susceptibility measures the rise in magnetic moment brought on by an applied field, whereas permeability measures the relative rise in flux brought on by the presence of the magnetic substance. The following five broad categories can be used to categorize magnetic behavior of magnetic materials.

2.4.1 Diamagnetism

Diamagnetism is material's magnetic characteristics by virtue of which it creates the oppositely directed magnetic field against the applied magnetic field. When electrons are realigned for the external magnetic field, diamagnetism arises. Diamagnetism is an extremely

weak form of magnetism that only manifests when an external field is applied, making it neither a permanent nor a highly strong feature. Fig. 2.3(a) express the atomic pattern for diamagnetic material before and after applied a magnetic field.

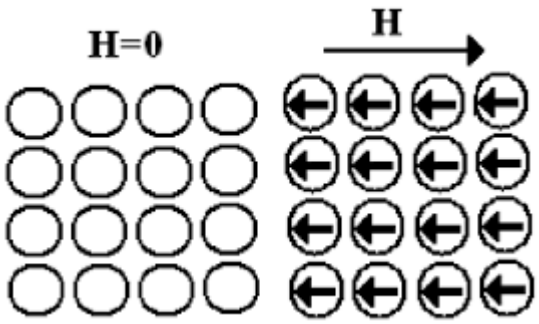

Fig. 2.3 (a) A diamagnetic material's atomic dipole configuration with and without an external magnetic field.

2.4.2 Paramagnetism

The tendency of a material to be magnetic under the influence of an external magnetic field of magnetic dipoles is known as paramagnetism; otherwise, the substance is non-magnet. Fig. 2.3(b). In the absence of a magnetic field, atomic dipoles are randomly dispersed in a paramagnetic environment.

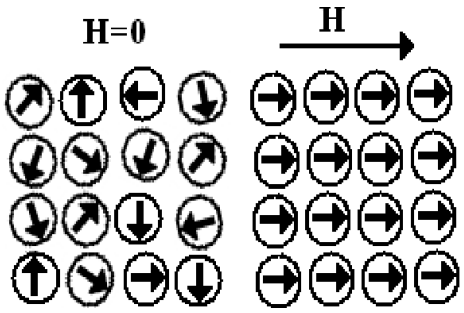

Fig. 2.3(b) A paramagnetic material's atomic dipole configuration with and without an external magnetic field.

2.4.3 Ferromagnetism

The phenomenon by which a material can display a spontaneous magnetization is termed as ferromagnetism and it is one of the most powerful types of magnetism. It appears in the majority of magnetic behavior observed in everyday life and serves as the foundation for all permanent magnets. Fe, Ni, Co, and their alloys are examples of traditional ferromagnetic materials with substantial magnetic moments. The dipolar interactions in these materials encourage parallel alignment of the magnetic dipole vectors, as a result in a material with net magnetization without an external magnetic field. The schematic diagram of an atomic dipole configuration for ferromagnetic material shown in Fig. 2.4 (a-b).

In ferromagnetic materials becomes paramagnetic above the Curie temperature and moments alignment is decreased at high temperature, whose susceptibility decreases with temperature and follows the Curie-Weiss law

$$\chi = C/T - \theta \qquad (2.1)$$

where C denotes Curie constant and θ represents Curie temperature of the material. Under this temperature, ferromagnets exhibit the property of spontaneous saturation magnetization even in zero fields.

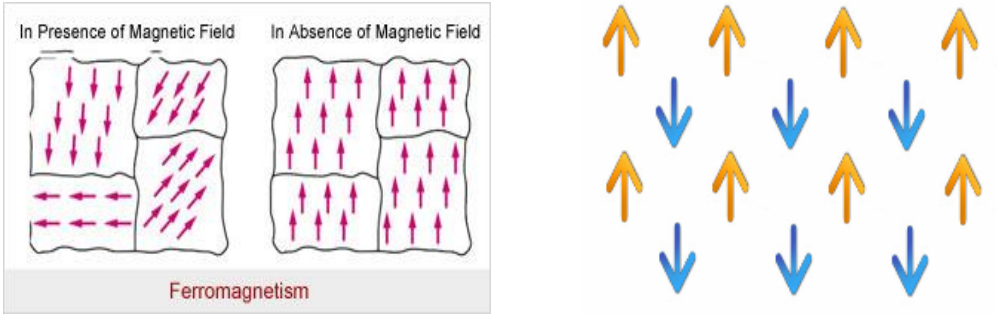

(a) (b)

Fig. 2.4 (a) A ferromagnetic material's atomic dipole arrangement [9] and (b) an antiparallel alignment of spin magnetic moments in an antiferromagnetic material is depicted schematically. [12].

2.4.4 Antiferromagnetism

Magnetic moments in antiferromagnetic materials are self-compensatoryly aligned, resulting in zero total spontaneous magnetization. These materials have magnetic moments at opposite direction for exchange forces of quantum mechanics. Magnetic ordering occurs when the magnetic moments of alternate atoms in a crystal align in opposite directions. As a result, no net magnetization occurred without the application of applied field. Fig. 2.4(b) shows a schematic illustration of the antiferromagnetic behavior in which a crystal sub lattices A and B subdivided as shown in Fig. 2.4(b). The spins in one sub lattice point one way, while the spins in the other point the opposite way.

2.4.5 Ferrimagnetism

In ferromagnetism, the materials have both parallel and anti-parallel molecular fields that align spins to the external magnetic field. In these materials, resulting in a net parallel magnetic field. The relative permeability is greater than 1 for these materials. A schematic diagram exhibiting ferromagnetism is shown in Fig. 2.5. Furthermore, ferrimagnetic substances, like ferromagnetic substances, exhibit significant spontaneous magnetization at room temperature, and this fact alone makes them industrially valuable. Similar to ferromagnetic, They are made up of magnetically saturated domains and exhibit magnetic saturation and hysteresis. Their spontaneous magnetization disappears above Curie temperature (T_c), and they subsequently act as paramagnetic. Ferrimagnetic materials act like ferromagnets, with spontaneous magnetization below the Néel temperature, T_N, and no magnetic order (are paramagnetic) beyond this temperature.

The magnetization compensation point is a temperature below the T_N at which the two sublattices have equal moments, resulting in a net magnetic moment of zero. In garnets and rare earth - transition metal alloys, this compensation point is plainly visible. Furthermore,

ferrimagnets may have an angular momentum compensation point, where the angular momentum of the magnetic sublattices is adjusted. This compensation point is critical for accomplishing high speed magnetization reversal in magnetic memory systems.

Snoek and his colleagues at the Philips research facilities in the Netherlands developed ferrites principally into economically usable magnetic materials between 1933 and 1945.

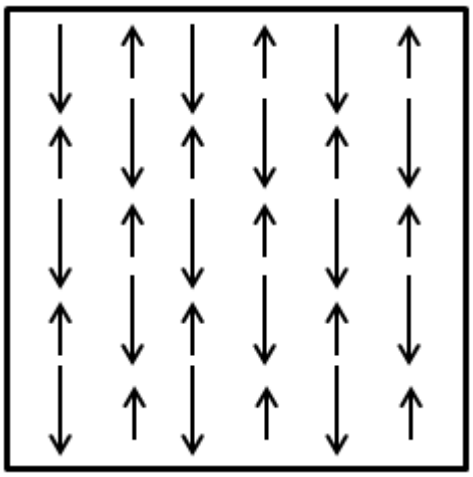

Fig. 2.5: The atomic dipole configuration of ferrimagnetic material.

In 1948, scientist L. Néel revealed the theoretical key to understanding ferrites in a prestigious publication, and the term ferrimagnetism is named after him.

2.4.5.1 Brief History of Ferrimagnetism

Ferrites and magnetic garnets are the most common ferrimagnetic materials [13]. Magnetite (iron (II, III) oxide; Fe_3O_4) known as the oldest magnetic substance, is a good example of ferrimagnet and it was previously categorized as a ferromagnetic before Néel discovered ferrimagnetism and anti-ferromagnetism in 1948[14]. Neel developed his theory of anti-ferromagnetism during the period (1936, 1947) and around the same period Snoek [15] from Holland discovered particularly fascinating features in a new class of oxide materials known as ferrites, which have been successfully exploited at high frequencies.

But, the difficulties have shown for the magnetic moment calculation of a ferrite such as magnetite, Fe_3O_4 or $FeO.Fe_2O_3$. For such formula , the theoretical number 14 of unpaired electrons 5 by Fe^{3+} ions and 4 the Fe^{2+} ions. The theoretical moment should be 14 μ_B, while the measured result was only about 4 μ_B, Néel's idea was then expanded to include ferrites. There were still two distinct lattice sites, as well as the same negative exchange interaction. The difference was that in antiferromagnetics, the moments on the two sites were equal, whereas in ferrites, they were not. As a result, complete cancellation did not occur, and a net moment emerged, which was the difference in the moments on the two sites. This difference is mainly caused by a differential in the quantity of magnetic ions present at the two types of sites. This is known as ferrimagnetism or uncompensated antiferromagnetism. Néel's idea presented in 1948 in an article titled "Magnetic Properties of Ferrites.; “Ferrimagnetism and Anti ferromagnetism”. Snoek published the experimental magnetic characteristics of a significant number of usable ferrites in a book titled "New Developments in Ferromagnetic Materials" the previous year (1936). Ferrimagnetism can be considered a subset of ferromagnetism, and domains can form similarly due to the interactions of the net moments of the lattice that occur throughout the crystal.

2.4.5.2 Properties of Ferrimagnetism

In ferrimagnetic substances, unlike antiferromagnets, the magnetic moments of the A and B sublattices are not equal (as expressed in Fig. 2.6). In a crystalline ferrimagnet, the magnetic atoms (A and B) occupy two types of lattice sites with different crystallographic environments, and each of them is occupied by one of the magnetic species, with ferromagnetic (parallel) alignment between the moments residing on the same sublattice. However, antiferromagnetic (antiparallel) alignment exists between A and B moments. Because the amount of A and B atoms per unit cell, and hence the values of A and B magnetic

moments, are generally different, and nonzero spontaneous magnetization happens at temperatures below Tc, [16-19].

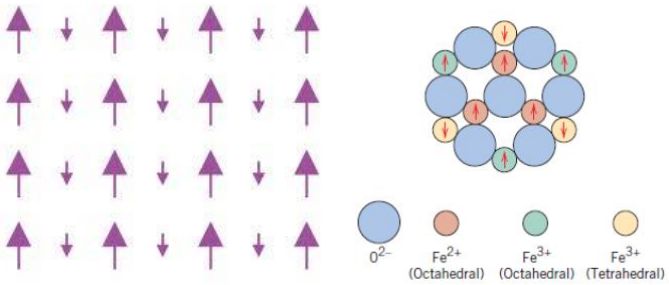

(a) (b)

Fig. 2.6 (a) Spin magnetic moment ordered configurations, (b) The spin magnetic moment arrangement of Fe^{2+} and Fe^{3+} ions in Fe_3O_4 is depicted schematically [20].

Ferrimagnetic materials have a Curie point as well; therefore one would expect paramagnetic behavior above the TC. However, the $1/\chi$ versus T curve will be concave as like as that found in antiferromagnetics because of the negative interaction, nearing an asymptotic value that would lead to a negative extrapolation. There are two essential conditions for magnetic order in solids:

(i) Magnetic moments (spins) should exist in individual atoms.

(ii) There should be exchange interactions that connect them.

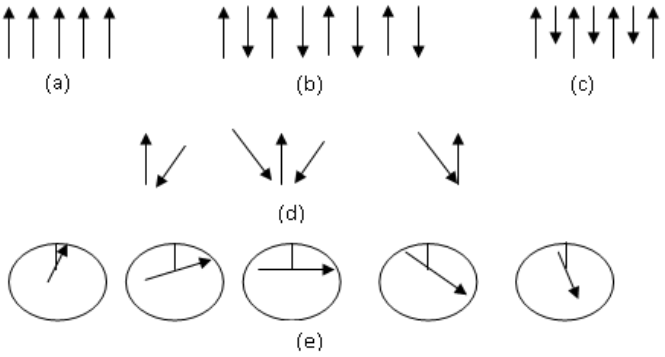

Fig. 2.7 Schematic representation of some magnetic structures (a) ferromagnetic (b) antiferromagnetic, (c) ferrimagnetic (d) triangular or canted; and (e) helical [21].

Because of the electrical wave functions of adjacent atoms overlap, magnetic moments originate in solids. Some transitional metals and rare earths exhibit this condition. The inter-atomic distance and the form of chemical bonds, particularly those between nearest neighbor atoms, are important factors on which exchange interactions rely. Because of the parallel coupling of adjoining atomic moments (spins), the positive exchange dominates, and the magnetic system becomes ferromagnetic below a particular temperature T_C, known as the Curie temperature. The common spin orientations can be determined using the crystal's minimal magneto-crystalline anisotropy energy. Therefore, spontaneous magnetization is important phenomenon to characterize the ferromagnetic substances. But in absence of applied field, in the demagnetized state, a ferromagnetic material exhibits no net magnetization because a ferromagnetic of macroscopic size is divided into a number of small regions called domains, spontaneously magnetized to saturation value, and the directions of these spontaneous magnetization of the various domains are such that the net magnetization of the specimen is zero.

The energy minimization is responsible for the existence of domains. The size and creation of these domains are complicatedly dependent on various aspects such as the shape of the material as well as its magnetic and thermal history. When negative exchange prevails, neighboring atomic moments align antiparallel to each other, and the substance is considered to be anti-ferromagnetic below a specific temperature, T_N, known as the Néel temperature.

2.5 Dielectrics

Materials can also be classified as conductors, semiconductors, insulators, or dielectrics based on their electrical conductivities. Insulators are defined in the context of electrical and electronic engineering as the class of materials through which no current can flow, particularly. An insulating material can be practically termed as dielectric when the material

attains its uniqueness in an electrical system. The major distinction between an insulator and a dielectric is the ability to accomplish the lowest electrical conduction with the highest resistance, resulting in catastrophic breakdown at high electric fields. To work under tremendous strains, additional technical characteristics such as low cost, extended life, chemical inertness, and capacity to endure high temperatures are listed.

2.6 Polarization

Polarization is the process of producing electric dipoles when a dielectric material is subjected to an external field. It is analogous to the polarization of atoms within an applied field.

2.7 Types of Polarization

Polarization is caused by a combination of atomic mechanisms and an externally induced electric field. Polarization comes in four varieties: electrical, ionic, orientation, and space charge. Dielectric materials typically display at least one of the polarizations listed above, depending on the type of material and the mode of external field application. The following polarization types are listed:

1. Electronic Polarization
2. Ionic Polarization
3. Orientation Polarization
4. Interfacial or Space Charge Polarization

Figure 2.8 depicts many forms of polarization.

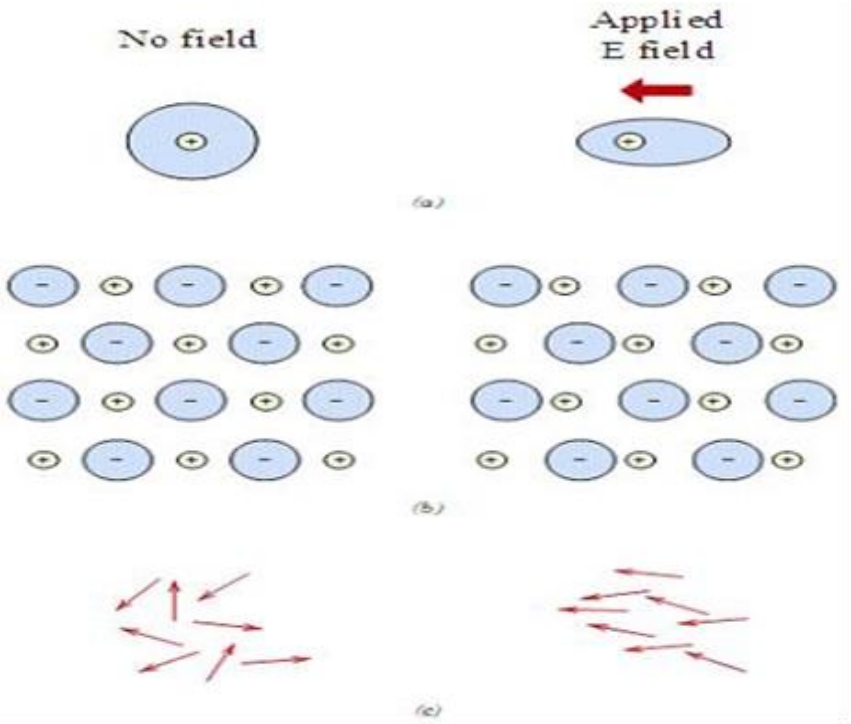

Fig. 2.8 (a) Electronic polarization brought generated by an electromagnetic field warping an atomic electron cloud, (b) Ionic polarization is brought on by the relative motions of electrically charged ions in reaction to an electric field and (c) Orientation polarization results from the response of permanent electric dipoles (arrows) to an applied electric field.

2.8 Dielectric in Alternating Fields

As the frequency is increased further, the permanent dipoles, if existent in the medium, will be unable to follow the field and the donation to static permittivity from this molecular process, the orientation polarization stops; this is common in the radio frequency band (10^6-10^{11} Hz) of the electromagnetic spectrum. At higher frequencies, often in the infrared (10^{11}-10^{14} Hz), the comparatively heavy positive and negative ions are unable to follow the field fluctuations, and the donation to permittivity from the atomic or ionic polarization disappears, leaving just the electronic polarization.

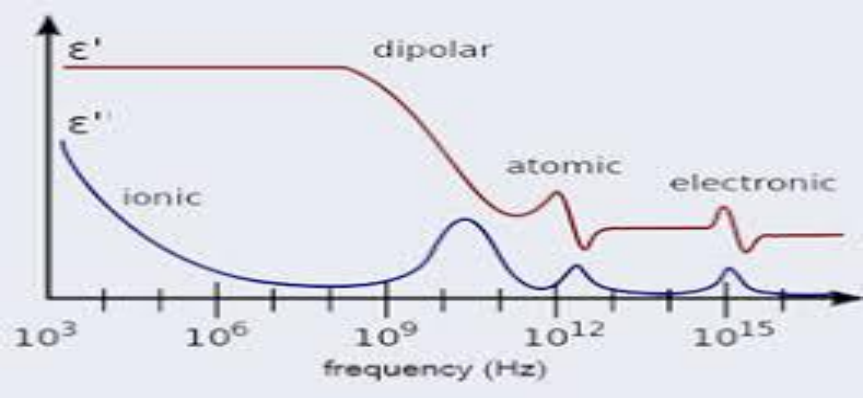

Fig. 2.9 Dielectric response in different frequency ranges.

Thus, the permittivity of dielectric material falls as the frequency approach increasing (Fig. 2.9), and termed as dielectric dispersion.

2.9 Magnetic Domain and Magnetization Process

2.9.1 Origin of Magnetic Domain

A domain is a region within a magnetic substance with uniform magnetization (M). Within a ferromagnetic region, atomic moments are parallelly aligned. The net moments of the antiferromagnetic interactions are spontaneously oriented parallel to each other (even in a ferrite domain, the net moments of antiferromagnetic interactions are spontaneously oriented parallel to one other (even without an applied magnetic field), which is known as spontaneous magnetization or polarization. Typically, domains are formed to reduce magnetostatic energy (Em), which is the magnetic potential energy contained in the field lines (or flux lines as they are usually known) linking the north and south poles outside of the material. Figure 2.10 (a) depicts a single domain with arrows indicating the direction of M and thus the direction of spin alignment in the domain [18].

The parallel order of spins in the entire sample can be promoted via exchange, and anisotropy can steer them in an easy path. In terms of exchange and anisotropy contributions, the crystal is predicted to have a minimum energy state. The E_m decreases significantly provided the

sample is divided into two or more smaller domains as shown in Fig. 2.10(a). There is a tendency to keep splitting to lower the energy of the system until more energy is required to construct the domain border than is decreased by E_m change. As closure domains form (closure domains are more likely to form in cubic anisotropy), (E_m) can be essentially removed. Thus, the boundaries between domains can possess only a small portion of the total energy. The size and geometry of a domain could be chosen by minimizing several sorts of energy. The possible types of those energies are [10];

1. Magnetostatic Energy,
2. Magneto-crystalline Anisotropy Energy,
3. Magnetostrictive Energy,
4. Domain Wall Energy;

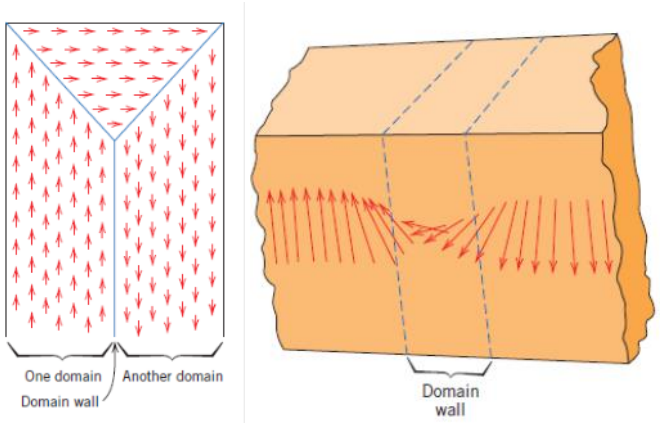

(a) (b)

Fig. 2.10 (a) Domains in a ferromagnetic or ferrimagnetic substance are depicted schematically; (a) The arrows depict atomic magnetic dipoles. All dipoles are aligned within each domain, although the direction of alignment changes from domain to domain and (b) The progressive shift in magnetic dipole orientation that occurs over a domain wall [22].

To separate the magnetic domains, the term ‘domain wall’ is introduced which is used as an interface illustrated in Fig. 2.10(b). It is a transition between various magnetic moments that usually has an angular displacement of 90° or 180°. Individual moments are gradually reoriented across a finite distance by means of domain walls. Domain wall thickness is determined by the anisotropy of the material, which typically spans 100-150 atoms. The difference in magnetic moments between the creation of the domain wall before and after is attributed to the energy of a domain wall whose the value is typically stated in terms of energy per unit wall area. The variation of the domain wall width is caused by two opposing energies: the magneto-crystalline anisotropy energy (E_k) and the exchange energy (J_{ex}), and both of these energies tend to be as low as feasible in order to achieve a more favorable energetic state. Individual magnetic moments aligned along the axes of the crystal lattice achieve the smallest value of E_k, reducing the breadth of the domain wall. J_{ex}, on the other hand, can be reduced as the magnetic moments align parallel to each other, thickening the wall due to their repulsion. Whereas anti-parallel alignment of magnetic moments would pull them closer together, causing the domain wall to thicken. As a result, expected equilibrium condition can be attained between the two and the width of the domain wall can be set.

2.10 Magnetism and Hysteresis

One of the most conspicuous manifestations of magnetism in solids of ferromagnetic materials such as iron or magnetite is spontaneous magnetization, which is frequently associated to hysteresis, a phenomena explored and described by James Ewing in 1881. One of the most important practical properties of any ferromagnetic material is its irreversible nonlinear response of magnetization (M) to an applied magnetic field (H). The hysteresis loop can be used to exemplify this response (Fig. 2.11).

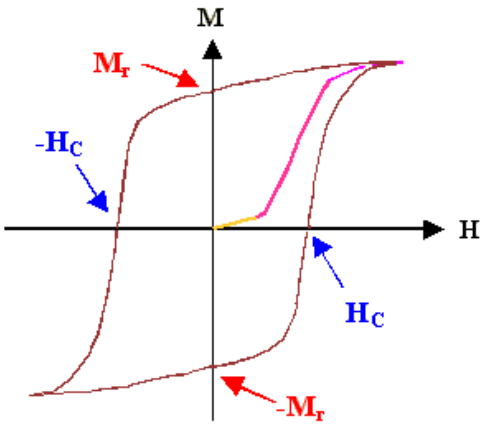

Fig. 2.11 Hysteresis loop [23].

2.11 Ferrites

Ferrites are a type of ferrimagnetic ceramic compound material composed of a modified structure of iron oxides such as hematite (Fe_2O_3) or magnetite (Fe_3O_4) and metal oxides such as CoO, MnO , ZnO, CuO, and NiO. Because of their non-conducting magnetic feature, eddy current and ohmic losses are lower than in ferromagnetic materials. Spontaneous magnetization behavior is exhibited by most of the ferrites below a certain temperature due to their ferromagnetic properties. In the magnetized state of ferrites, the spin magnetic moments are parallel and directed oppositely to each other, resulting in a decrease in magnetization in comparison to ferromagnetic metals. The main advantage of ferrites is their greater versatility in tailoring their electrical and magnetic properties to specific applications. The properties of ferrites are strongly influenced by synthesis conditions, composition, and microstructure [24]. A wide range of compositions are conceivable in ferrites. Controlling the characteristics of ferrites is attainable with good knowledge of crystal structure and site occupation of distinct cations [25].

As compare with the ferromagnetic metals, ferrites possess higher resistivity for intrinsic level of oxygen and metal atoms. As a result, ferrite can now perform applications at higher frequencies in a variety of devices such as microwave devices , transformer cores, computer

memories, credit cards, computer hard drive , telephones, and such as circulators, isolators, and phase shifters, among others. Ferrites have the molecular formula $Me'Fe_{2-x}^{3+}Me_x''O_4$, where Me' represents divalent cations like Fe, Mn, Co, Ni, Cu, Mg, Zn, Cd, or a combination of cations with an average valency of two, and Me″ represents trivalent cations like Cr, Al, La, Sm, or a combination of cations with an average valency of three. The composition value can range between zero and two, however if x is close to two, these oxides can no longer be considered ferrites [26].

Ferrites are categorized into two types based on their magnetic coercivity, or internal magnetism persistence. There are two types of ferrites: soft ferrites and hard ferrites.

2.12 Classification of Ferrites

Based on the crystal structure and magnetic ordering, ferrites can be classified as;

Table 2.1 Classification of ferrites

Types	Structure	GeneralFormula	Examples
Spinel	Cubic	$A^{II}Fe_2O_4$	A^{II}=Mg,Co, Zn, Ni,Cd
Garnet	Cubic	$Ln_3{}^{III}Fe_2O_{12}$	(Ln^{III}=Y,Sm,Eu,Gd,Er
Hexa-ferrite	Hexagonal	$M^{II}Fe_{12}O_{19}$	$BaFe_{12}O_{19}$
Ortho-ferrite	Pervoskite	$LnFeO_3$	Ln=similaras garnets

We intend to discuss the spinel ferrites in detail only because our research work is based on spinel ferrites.

2.12.1 Spinel Ferrites

Because of their vast application potential, spinel ferrite nanoparticles (NPs) are currently under the limelight of nanoscience. The excellent magnetic characteristics of spinel ferrite NPs, which are frequently complemented by other functional qualities such as catalytic

activity, are quite intriguing. Furthermore, the magnetic sensitivity of the NPs can be modified to some extent by particle size and shape.

Structural and electronic flexibility of spinel ferrites is most interesting feature due to the incorporation of wide ranged cations and valence in tetrahedral and octahedral sites. Bragg and Nishikawa determined the spinel structure of ferrites as exhibited by mineral spinel MgAl2O4 in 1915 [27, 28]. In general, the chemical formula for spinel ferrite is MFe_2O_4, where M is a divalent metal ion [29] such as Ni^{2+}, Fe^{2+}, Co^{2+}, Zn^{2+}, Cd^{2+}, Mg^{2+}, or of these ions' combination.

- *Tetrahedral sites*

The interstitial is located in the core of a tetrahedron produced by four lattice atoms in the tetrahedral (A) site. Three anions are in plane, contacting each other; the fourth anion is symmetrically positioned on top, in the center of the three anions. The cation is in the middle of the void formed by these four anions. The tetrahedral position in the FCC lattice is seen in Fig. 2.12.

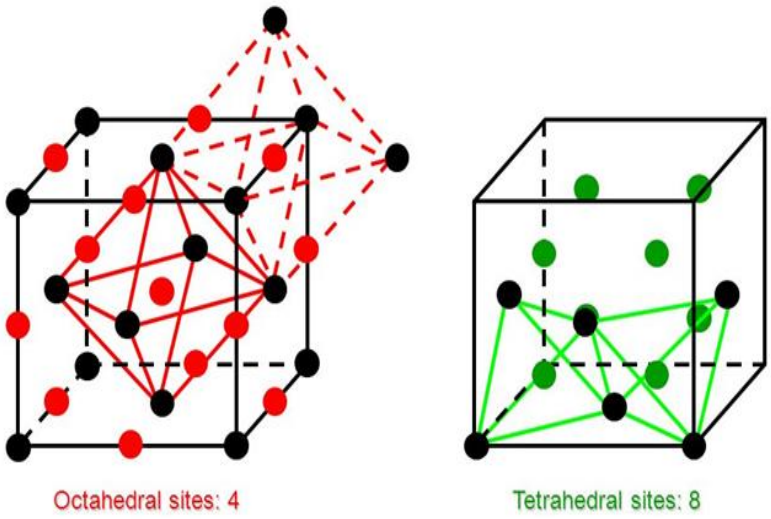

Fig. 2.12 FCC lattice of tetrahedral and octahedral locations

- *Octahedral sites*

The interstitial is at the heart of an octahedron made by 6 lattice anions in an octahedral (B) site. Four anions are in a plane, with the other two anions positioned symmetrically above and below the plane formed by the four anions. Cation fills the vacuum left by six anions in an octahedral structure. Figure 2.12 depicts an octahedral site in an FCC lattice.

2.12.2 Spinel Ferrites Classification

- Because of the distribution of cations on (A) tetrahedral and (B) octahedral sites, spinel ferrites have been divided into three groups.
- *Normal spinel ferrites*

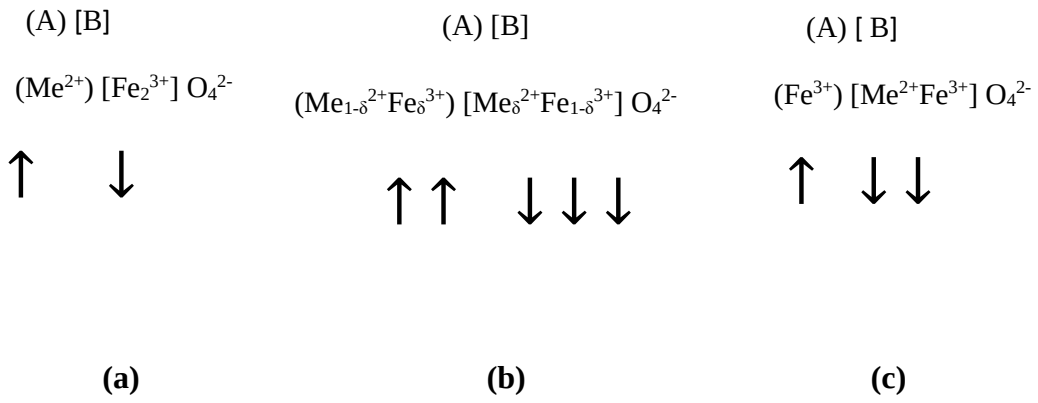

Fig. 2.13 Distribution of cations in spinel ferrites in (a) normal, (b) mixed and (c) inversed spinel ferrites.

The structural formula of such ferrites is $(Me^{2+})\ [Fe_2^{3+}]\ O_4^{2-}$, where Me^{2+} prepares to A sites. This distribution occurs in zinc ferrites $(Zn^{2+})\ [\ Fe_2^{3+}]\ O_4^{2-}$. Figure 2.13(a) shows a schematic representation of this form of spinel ferrite.

- ***Mixed spinel ferrites***

When the cations Me^{2+} and Fe^{3+} occupy both the A and B locations, the structure is called a mixed spinel structure; The structural formula for this ferrite is $Me_{1-\delta}^{2+}Fe_{\delta}^{3+}\ [Me_{\delta}^{2+}Fe_{2-\delta}^{3+}]\ O_4^{2-}$, here δ is the inversion degree. This type of structure is represented by MnFe2O4, which has an inversion degree of = 0.2 and as a result of its structural formula is $(Mn_{0.8}^{2+}Fe_{0.2}^{3+})$

$[Mn_{0.2}^{2+}Fe_{1.8}^{3+}]\ O_4^{2-}$ [30]. Figure 2.13(b) shows a schematic representation of this form of spinel ferrite.

- *Inversed spinel ferrites*

Inversed spinel structure with all Me^{2+} ions in B-positions and Fe^{3+} ions distributed equally across A and B-sites: These ferrites' structural formula is $Fe^{3+}[Me^{2+}Fe^{3+}]\ O_4^{2-}$. The spinel structure of magnetite Fe_3O_4, ferrites $NiFe_2O_4$ and $CoFe_2O_4$ is inversed [28]. In inversed ferrites, one half of the Fe^{3+} is bound to A-sites and the other half to B-sites. Their magnetic moments cancel each other out, and the ferrite's resultant moment is owing to the magnetic moments of bivalent cations Me^{2+} in the B-positions. Figure 2.13(c) shows a schematic representation of this form of spinel ferrite.

2.12.3 *Hexagonal Ferrites*

Went, Rathenau, Gorter, and Van Oostershout 1952 [28] and Jonker, Wijn, and Braun 1956 were the first to notice this. Hexaferrites are ferromagnetic oxides with the formula $MFe_{12}O_{19}$, where M is an element such as barium, lead, or strontium. The oxygen ions in these ferrites have a closely packed hexagonal crystal structure. They have a strong coercivity and are commonly utilized as permanent magnets. They are utilized a lot. Their hexagonal ferrite lattice is comparable to spinel structure with closely packed oxygen ions, but there are also metal ions with the same ionic radii as oxygen ions in some layers. Hexagonal ferrites are generated by the replacement of oxygen ions and have bigger ions than garnet ferrites. The vast majority of these bigger ions are barium, strontium, or lead.

2.12.4 *Garnets*

In 1951, Yoder and Keith [28] stated that replacements can be done in ideal crystal garnet $Mn_3Al_2Si_3O_{12}$. They created the first silicon-free garnet $Y_3Al_5O_{12}$ by replacing $Mn^{II}+Si^{IV}$ with $Y^{III}+Al^{III}$. In 1956, Bertaut and Forret synthesized [30] $Y_3Fe_5O_{12}$ and measured its magnetic

characteristics. Geller and Gilleo produced and studied $Gd_3Fe_5O_{12}$, a ferromagnetic compound, in 1957 [30,31].

The typical formula for a pure iron garnet unit cell is $M_3Fe_5O_{12}$, where M is the trivalent rare earth ion (Y, Gd, Dy). Their cell form is cubic, and their edge length is approximately 12.5 Å. They have an intricate crystal structure. They are significant because of their applications in memory structures.

2.13 Application of Ferrites

Soft ferrites are more easily magnetized and demagnetized than hard ferrites, and as a result, they are widely employed in transformer cores for telecommunication, computer, medical, television, and other electronic systems. Hard ferrites, on the other hand, cannot be easily demagnetized but, once magnetic, can be employed in permanent magnets such as micromotors and loud speakers. Polycrystalline ferrites with a minimum loss factor are excellent choices for high frequency applications. They are appropriate for quality applications as well as low and high frequency applications because to several significant qualities such as saturation magnetization (M_S), coercive force (H_C), initial permeability (i), and losses. It is simple to achieve the best combination of these features for any given application by simply adjusting the compositions, either through the addition of additives or through the various production processes. Depending on the application, most of these factors can be modified to some extent.

2.14 Conclusions

This chapter has covered the fundamentals of ferrites' dielectric, magnetic, electric, and structural properties. Size is an important property of ferrites. Conductivity, dielectric loss tangent, dielectric constant, saturation magnetization, coercivity, and relative permeability are only a few of the electromagnetic properties of nanocrystalline materials that are very with size.

Ferrites with low loss factors are suitable choices for high-frequency applications. Spinel ferrites have structural and electrical flexibility due to the incorporation of a variety of cations and valences in tetrahedral and octahedral positions.

References:

[1] P. G. Hewitt. Conceptual Physics, 7th Ed. Harper Collins College Publishers, NewYork (1993).

[2] B. D. Cullity, "Introduction to magnetic materials, Addison-Wesley Publishing Co." *Inc. Reading MA* (1972).

[3] A. Hengelein, Chem. Rev. 89 (1989) 1861.

[4] M. F. Ashby, T. J. Lu, Metal foams: A survey. Sci. China B 46 (2003) 521.

[5] M. I. Barato, Synthesis, Fictionalization and surface treatment of Nanoparticles, American Scientific: USA, 2003.

[6] C. Q. Sun "Size dependence of nanostructures: Impact of bond order deficiency." *Progress in solid state chemistry* 35.1 (2007): 1-159.

[7] A. S. Edelstein, R. C. Cammarata, Nanomaterial: Synthesis, Properties and Applications. Taylor & Francis: London, 1996.

[8] H. Gleiter, Nanocrystalline Materials. Prog. Mater. Sci. 33 (1989): 223-315.

[9] D. William. Callister, Jr., G. David G. Rethwisch, Materials Science and Engineering: An Introduction, John Wiley & Sons, Inc., 2009.

[10] R. Becker, W. Döring, Ferromagnetismus, Springer, Berlin, 1939.

[11] H. Lawrence, V. Vlack, "Elements of Material Science and Engineering", 6th Ed. Addison- Wesley Co. (Publishers) Ltd., New York, 1989.

[12] A Richard, Flinn, K. Paul, Trojan, Engineering Materials and Their Applications, 4th edition, John Wiley & Sons, Inc., 1990.

[13] S. Hilpert, Ber. Deutseh. Chem. Ges. Bd 2. 42 (1909) 2248.

[14] L. Néel, "Properiětěsmagnětique des Ferrites; Ferrimagnětisme et Antiferromagnětisme", *Annales de Physique*. 3 (1948)137-198.

[15] J. L. Snoek., "Magnetic and Electrical Properties of the Binary System $MOFe_2O_3$" Physica 3 (1936) 463.

[16] K. H. J. Buschow, F. R. De Boer, Physics of Magnetism and Magnetic Materials, Kluwer Academic Publishers, New York, USA, 2004.

[17] A. Goldman, Modern ferrites Technology, 2nd Edition, Pittsburgh, PA, USA, 1999.

[18] R. Valenzuela, Magnetic Ceramics, Cambridge University Press, Cambridge, 1994.

[19] B. D. Cullity, Introduction to Magnetic Materials, Addison-Wesley Publishing Company, Inc., California, 1972.

[20] A. Richard, Flinn, K. Paul, Trojan, Engineering Materials and Their Applications, 4th

edition, John Wiley & Sons, Inc., 1990.

[21] R. Valenzuela, Magnetic Ceramics, Cambridge University Press, Cambridge, 1994.

[22] W. D. Kingery, H. K. Bowen, D. R. Uhlmann, Introduction to Ceramics, 2nd edition, John Wiley & Sons, New York. 1976.

[23] S. Chickazumi, and S. H. Charap, Physics of Magnetism, Krieger Pub. Co., 1978.

[24] D. J. Griffiths, Introduction to Quantum Mechanics, Prentice Hall, New Jersey, 1995.

[25] Jiles D. C. Recent advances and future directions in magnetic materials, Acta MOler. 51 (5907-5939), 2003.

[26] V. A. M. Brabers, "Progress in Spinel Ferrite Research" in Handbook of Magnetic Materials, vol. 8, Edited by K. H. J. Buschow, Elsevier Science B. V, 1995.

.

[27] W. H. Bragg, Phil. Mag. 30 (1915) 305.

[28] K. J. Standley, Oxide Magnetic Materials, 2nd ed., Oxford University Press, 1972.

[29] M. M. Haque, M. Huq, M. A. Hakim, Mat. Chem. Phys. 112 (2008) 580-586.

[30] J. Smith, Wijn H.P.J., Ferrites, Philips Technical Library, Eindhoven, The Netherlands, 1965.

[31] B. D. Cullity, Introduction to Magnetic Materials, Addison-Wesley Publishing Company, Inc., California,1972.

Chapter 3

Synthesis of Nanoparticles

In this chapter, we focused on the procedures and analysis techniques utilized to investigate the various properties of our ferrite nanoparticles. The fabrication of the spinel structure is a common goal for all ferrites. To create ferrite powders, most researchers employ the traditional Ceramic method or Solid-State Reaction technique. There exist various methods to prepare ferrite samples, some are mentioned in the following [1-7]:

1) Sol-gel synthesis
2) Organic precursors
3) Combustion synthesis
4) Spray-drying
5) Freeze-drying
6) Co-precipitation
7) Glass crystallization
8) Micro-emulsion method
9) Hydrothermal method
10) Ball-milling technique
11) Reverse micelles process

The auto combustion process was employed to create our current nano-crystalline ferrites. In the next sections, we go over the specifics of the sample preparation method and measurement techniques.

3.1 Sol-gel Auto Combustion Synthesis

The auto combustion synthesis procedure was utilized to synthesize Al substituted Ni-Cu-Cd ferrite nanoparticles, and this method is regarded a unique way for preparing fine ferrites since it makes use of the intense exothermic reaction between metal nitrate and fuel. Comparative to other synthesis techniques, the advantages of this process are inexpensive precursors, a simple preparation method, low external energy consumption, requirement of simple equipment, cost effectiveness, enhanced particulate characteristics of the product that result in nano-sized, extremely reactive and homogenous [8].

This auto combustion synthesis, also known as self-propagating synthesis, was first developed by Russian scientist Merzhanov, and in recent years, combustion synthesis has not only opened new vistas for the preparation of various novel nano-size oxides and composites, but has also succeeded in continuous synthesis methods of nano-powders.

The advantages of auto combustion method include:

- chemical uniformity is very high;
- excellent purity and crystallinity of the product;
- small particle size and narrow particle size distribution;
- Stoichiometry that is simple to manipulate;
- simple equipment and preparation method;
- processing time is short;
- minimal external energy usage (the process begins at low temperatures) and
- There are no numerous steps involved.

3.2 Synthesis of Ferrite Nanoparticles

The auto combustion synthesis procedure was employed to create Al-replaced Ni-Cu-Cd nanoparticles of ferrite, and this method is regarded as a promising strategy for the manufacture of nanocrystalline ferrite particles. 'AR' ranking of $Fe(NO_3)_3 \cdot 9H_2O$,

$Ni(NO_3)_2.6H_2O$, $Cu(NO_3)_2.3H_2O$, $Cd(NO_3)_2{\cdot}4H_2O$ and $Al(NO_3)_3.9H_2O$ as initial ingredients to fabrication of the samples. To make a solution, we thoroughly mixed stoichiometric proportions of the above basic components and added some ethanol to improve mixture homogeneity. Ethyl alcohol is required for metal ion separation and homogenous structure. Water evaporation eliminates the dew of metal nitrates for the existence of electropositive metal ions and electronegative oxygen ions, resulting in a homogeneous structure for the pioneer elements. AR grade liquid ammonia (25%) was added to control pH7, which also enhances metal ion solubility. The uniform gel created as a result of constant magnetic stirrer stimulation. The resultant solution was then heated continuously at a water bath at 70°C for 24 hours to produce better-dried gel. It was then heated to 200°C to produce fluffy loose powder. The material was prepared in CUET's postgraduate lab (Fig. 3.1,3.2).

(a) (b)

Fig. 3.1 (a) Steam bath and (b) High temperature furnace at postgraduate-lab in physics department at CUET.

The synthesis process of ferrite nano-particles have been illustrated in the **flow chart** shown in the following:

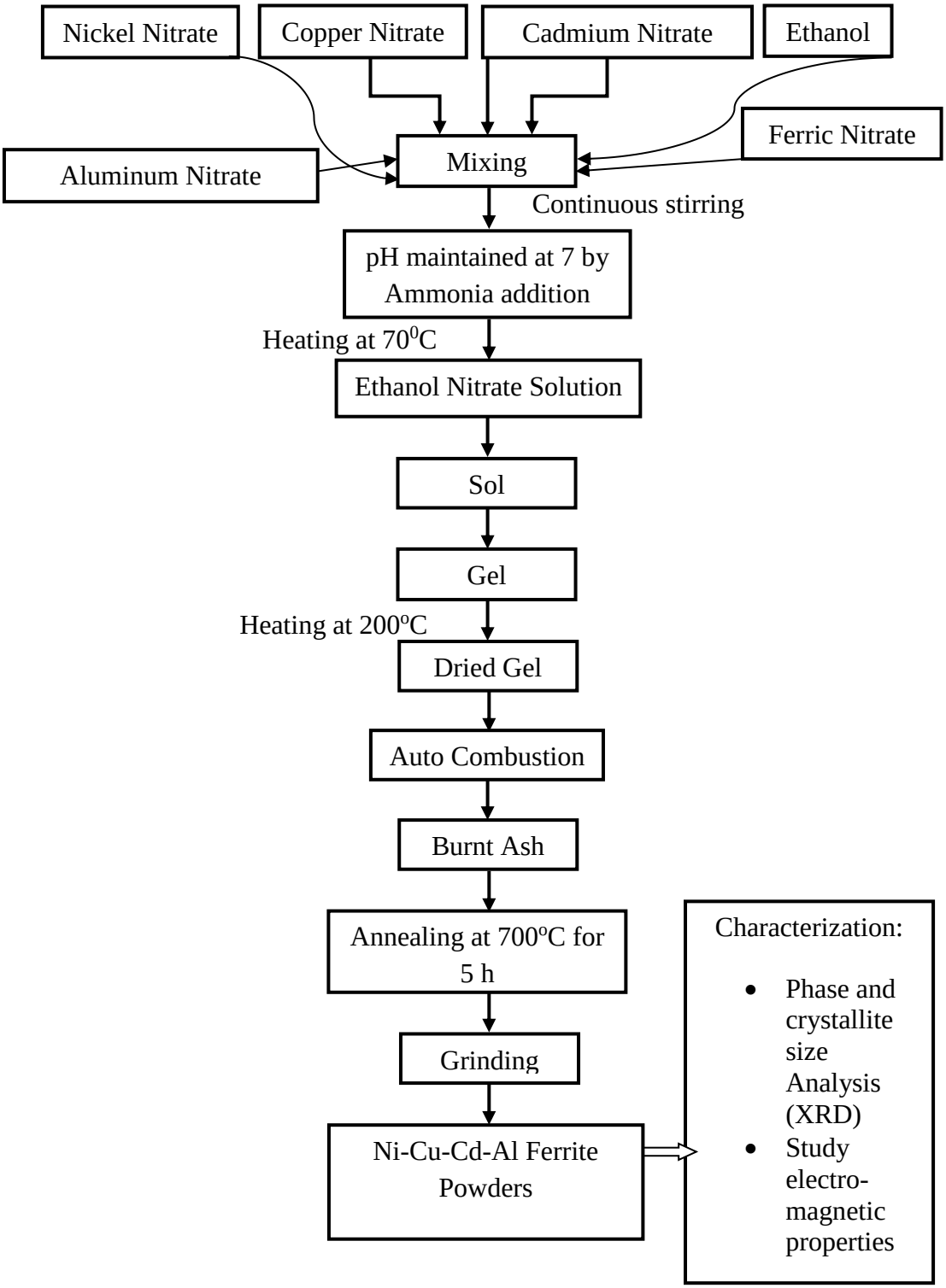

3.3 Annealing

These powders were annealed for 5 hours at 700 ^{o}C to eliminate any undesirable ingredients and to ensure structural homogeneity. The temperature ramps were 10 ^{o}C per minute and 5 ^{o}C per minute heating and cooling. The annealed powder was then milled for 3 hours further. The specimens were crushed into a round disc (pellets) for electric measurements at 5000 psi for about 2 minutes. A uniaxial press was utilized to make parallel plate-shaped capacitors, and two probe connections were guaranteed by putting silver paste to opposing faces. The sample preparation equipment is depicted in Fig. 3.2.

(a) **(b)** **(c)**

(d) **(e)**

Fig. 3.2 (a) Electrical equilibrium, (b) Magnetic stirrer (c) Dry gel (d) After heating at 200 ^{o}C (e) Heating at 700 ^{o}C

3.4 Conclusions

Nanoparticle synthesis is an important step which is discussed in detail in this chapter. The Al substituted Ni-Cu-Cd ferrite nanoparticles fabricated using a sol-gel auto combustion technique. Complete sample preparation was done at CUET's postgraduate lab. To ensure structural homogeneity and the removal of any undesired ingredients from the formulation, sample powders were annealed for five 5hr at 700 ºC. Under high pressure, the samples were shaped into disc (pellet) specimens for various characterization.

References

[1] A. Goldman, Handbook of Modern Ferromagnetic Materials, Kulwer Acad. Pub, Boston. U.S.A (1999).

[2] R. Valenzuela, Magnetic Ceramics, Cambridge University Press. Cambridge (1994).

[3] J. Z. Jiang, P. Wynn, S. Morup, T. Okada, F. J. Berry, Nanostructured Mater. 12 (1999) 737.

[4] H. Li, H.Z. Wu, G.X. Xiao, Powder Technol. 198 (2010) 157-166.

[5] A. Kale, S. R. Gubbala, D. K. Misra, J. Magn. Magn. Mater. 277 (2004) 350.

[6] J. P. Hochepied, J. F. Bonville, M.P. Pileni. J. Phys. Chem. 104 (2000) 905.

[7] M. Atif, S. K. Hasanian, S. K, M. Nadeem. Solid State Comm. 138 (2006) 416.

[8] Z. Yue, L. Li, J. Zhou, H. Zhang, Z. Gui. Mat. Sci. Engg. B, 64 (1999) 68.

Chapter 4

Experimental Techniques

We will explain fundamental experimental methodologies for measuring various lattice characteristics as well as frequency-dependent electric and dielectric properties of ferrite nanoparticles. The FESEM measurement system was used to measure surface morphology and nanostructure. The samples were physically characterized using XRD.

VSM was used to measure magnetic hysteresis. The electrical transport properties were measured using two probe methods and an impedance analyzer. A custom-made sample holder and an impedance analyzer were used to perform dielectric and impedance measurements. The modulus spectroscopy analysis is also thoroughly addressed.

4.1 Experimental Techniques

4.1.1 X-ray Diffraction Analysis

The crystal structure can be determined using XRD. X-ray diffractometer with Cu-K radiation of wavelength = 0.15418 nm was used for structural characterization. Thousands of granules in the powder have random orientations. It is expected that with random orientations, the majority of the distinct atomic planes will lay parallel to the surface in some of the grains. Scanning through different angles would thus correspond to varied atomic spacing. A powdered sample was loaded onto a sample stage for X-ray scanning.

The X-ray powder diffractogram can provide the following information:

- Sample preparation quality and validation
- The reflections' inter-planer spacing (d).
- The amplitudes of the reflections
- The dimensions of the unit cells and the lattice type.

An electronic detector was positioned on the opposite side of the sample from the X-ray tube and rotated the sample through different Bragg's angles to detect the diffracted X-rays. The goniometer recorded the angle (2θ), and the detector recorded the observed X-rays in counts/sec, which was forwarded to the computer.

All samples' XRD patterns were acquired over 2θ range of 15-60^o using a step size of 0.01^o for phase identification and preferred orientations. The X-ray intensity (counts/sec) was plotted against the angle theta (2θ after scanning the sample). Using Bragg's formula, the 2θ for each diffraction peak was transformed to d-spacing; n = 2d Sin, n is the order of diffraction[1].

The formula was used to calculate the lattice parameter for each peak of each sample [2]:

$$a = d\sqrt{h^2 + k^2 + l^2}$$

where h, k, and l are crystal plane indices. The Nelsion-Riley approach was used to obtain the exact lattice parameter for each sample. F(θ) denotes the Nelsion-Riley function[3]:

$$F(\theta) = \frac{1}{2}[(Cos^2\theta/Sin\theta) + (Cos^2\theta/\theta)]$$

The lattice constant 'a' values of all the peaks in a sample are shown against F(θ).The exact lattice parameter 'a_o' is then calculated using the least square fit approachThe real lattice parameter is the point where the least square fit straight line intersects the y-axis (i.e. at $F(\theta)$ = 0).

4.1.2 *Crystallite Size Measurement*

Particle size determination is crucial in ferrite nanoparticles. In the case of fine particles, as particle size is lowered, the XRD lines broaden, indicating that particle size has been reduced. The full width at half maximum (FWHM) of the diffraction peaks provides information about

particle size. When atoms fill all lattice positions and there are no imperfections in the crystal, it is said to be perfect. The broadening of diffraction peaks is caused primarily by three reasons. The influence of small crystallite sizes causes the peaks to expand, and so an examination of peak broadening can be used to discover which crystallite sizes provide more broadening into the diffraction peaks. The crystallite size (DXRD) of the samples was assessed using imaging technology from nano-graphse[4].

Bragg's law, which is provided by 2dSin = $n\lambda$, gives the requirement for constructive interference, reinforcement of X-ray scattering from a crystalline powder. This corresponds to an integral (n) number of X-ray wavelengths (λ) as the path difference of X-ray scattered from parallel crystalline planes separated by d =d_{hkl}. The diffraction angle measured with respect to the crystallographic planes is given here. Bragg scattering occurs at discrete values of 2θ satisfying the Bragg condition for an infinite crystal, i.e. Bragg peaks are δ functionThe peaks of finite-sized crystals are expanded over a variety of angles.

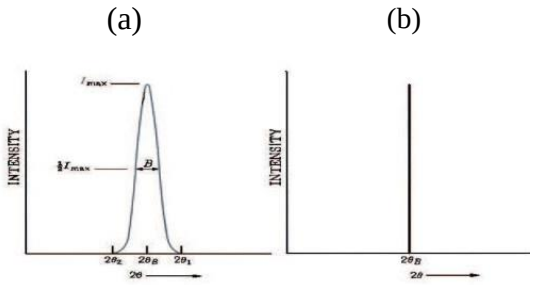

Fig. 4.1 Diffraction curves and the impact of small particle size (Schematic): (a) small particle size and (b) large particle size.

To explain the phenomenon of fine particle widening, imagine a finite crystal with thickness t = md, where m is an integer and d is the distance between crystal planes, i.e. t contains m planes. Considering In Fig. 4.1, the breadth of the peaks or full width at half maximum (FWHM) is provided if the broadened Bragg peak begins at an angle of $2\theta_2$ and ends at $2\theta_1$.

$$\beta = \frac{1}{2}(2\theta_1 - 2\theta_2) = (\theta_1 - \theta_2)$$

Consider the route differences for each of the two angles θ_1 and θ_2 for an X-ray traveling the entire thickness of the crystal. The width β is often expressed in radians. We now create path difference equations for these two angles, which are connected to the crystal's overall thickness rather than the distance between adjacent surfaces.

$$2t\ sin\,\theta_1 = (m+1)\lambda$$

$$2t\ sin\,\theta_2 = (m-1)\lambda$$

By subtraction we get :$D(sin\,\theta_1 - sin\,\theta_2) = \lambda$

$$2t\cos\tfrac{1}{2}(\theta_1+\theta_2)\sin\tfrac{1}{2}(\theta_1-\theta_2) = \lambda$$

But θ_1 and θ_2 are both close nearly equal to θ, so that $\theta_1 + \theta_2 \approx 2\theta$ and $\sin\left(\frac{\theta_1 - \theta_2}{2}\right) \approx \left(\frac{\theta_1 - \theta_2}{2}\right)$. So, the equation can be written as

$$2t\cos\left(\frac{2\theta}{2}\right)\left(\frac{\theta_1-\theta_2}{2}\right) = \lambda$$

Or,

$$2t\cos\theta\left(\frac{\theta_1-\theta_2}{2}\right) = \lambda$$

From above we get,

$$t\beta\ cos\,\theta = \lambda$$

Or, $$t = \frac{\lambda}{\beta\ cos\,\theta}$$

A more precise empirical treatment produces: $t_{xrd} = \frac{0.9\lambda}{\beta\ cos\,\theta}$

This is referred to as Scherrer's formula . The measured width of diffraction curves is used to estimate the particle size of very small crystals. Before estimating the crystallite size, the instrument-induced line widening was removed from the peak width using the following formula:

$$B^2 = B^2_{meas} - B^2_{equip}$$

where B_{meas} = entire width measured at half maximum from peak , B_{equip}= instrumental broadening.

4.1.3 Surface Morphology and Nanostructure

The topography, morphology, and composition of the materials can be studied with considerably better resolution using FESEM. The secondary electrons, X-rays, and backscattered electrons are ejected from the sample when a beam of extremely energy electrons strikes it. Following their collection by the detector, these electrons are then transformed into a signal that appears on a screenIn the current investigation, a (JSM-840 scanning electron microscope JEOL) was used to capture the FESEM nano-graph on the surface of the sample. Using a sputter coater, a thin layer of platinum was applied to the non-conductive samples. Using the imaging approach on nano-graphs captured with the FESEM, the average grain sizes of the samples were ascertained. The nature of the nanostructure has a significant impact on the mechanical, chemical, and particularly electrical and magnetic properties of ferrites. The grain boundaries that divide the grains or the interfaces between the crystals are intricate and interactive interfaces.

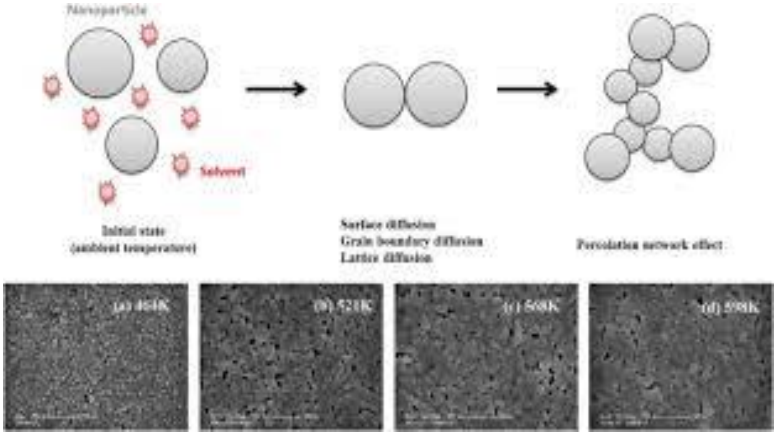

Fig. 4.2: Schematic representation of synthesis.

The area that accommodates the variation in crystallographic orientation between the adjacent grains is known as the grain border. The quantity and spacing of an array of dislocations that make up the grain boundary for some simple designs rely on the angular deviation between the grains. Due to the ionic character of ferrites, which makes up a major portion of the overall boundary energy, dislocation patterns are significantly more complicated than in metals.

The grain boundaries characteristics of low-loss ferrite can be affected by

- Generating an inter-granular layer with high resistivity,
- Serving as a sink for contaminants that could be used as grain growth enhancers and sintering aids.
- Providing a pathway for oxygen passage, which might change the oxidation status of cations close to borders..

Sintering and all other diffusion phenomena depend heavily on interfaces; for example, diffusion along grain boundaries can move 100 times more quickly than across them. Second phases that have segregated are frequently seen near interfaces; in fact, in ceramics, grain boundaries are more susceptible to segregation than their counterparts in metals because segregation can be aided by electrostatic interactions. Grain borders become inhomogeneous when segregation takes place because they have a different chemical makeup from the grains. Magnetic characteristics can be controlled by grain size homogeneity and average grain size (D). Ceramic flaws, in addition to grain boundaries, might obstruct domain wall motion and lessen the magnetic property. Pores, cracks, inclusions, second phases, and residual stresses are a few of these. Additionally, imperfections serve as energy wells that anchor the domain boundaries and demand more activation energy to separate.

4.1.4 Wayne Kerr Precision Impedance Analyzer

The accurate impedance measurement and analysis of a wide range of electronic devices (components and circuits), as well as electronic and non-electronic materials, is substantially supported by the Wayne Kerr impedance analyzer. Additionally, it is an effective tool for contexts including materials research and development (both for electronic and non-electronic materials) as well as circuit design and development.

- Dependable measurement over a broad frequency range of 20 Hz to 15 MHz;
- Effective impedance analysis tools;
- Simple operation and flexible PC connectivity.

The following formula can be used to express the coil's complex impedance Z:

$$Z = R + jX$$

where X for the reactive component and R stands for the resistive component.

4.1.5 Magnetization Measurement

The force the ferrite specimen felt in a gradient of magnetic field has been used to calculate saturation magnetization. The vibrating sample magnetometer (VSM) (Micro Sense, model EV9) illustrated in fig. 4.3 was used to measure it. The measurement of the electromotive force produced by a magnetic sample when it vibrates at a constant frequency while being surrounded by a static, homogeneous magnetic field is the foundation of the VSM theory. In order to prevent movement inside the sample container, a small portion of nano-crystalline materials (10–11 mg) was weighed. The VSM was run at 82 Hz vibration frequency up to 3 T. A Ni standard (spherical) with a known magnetization (M_s= 6.92 emu at 5 kOe) was used to calibrate it. With the temperature chamber in place, the EV9 VSM can reach fields of up

to 21.5 kOe at a sample spacing of 5 mm. Up to one Tesla of fields might be delivered by the VSM. The VSM could identify magnetic moments as small as 0.5 emu.

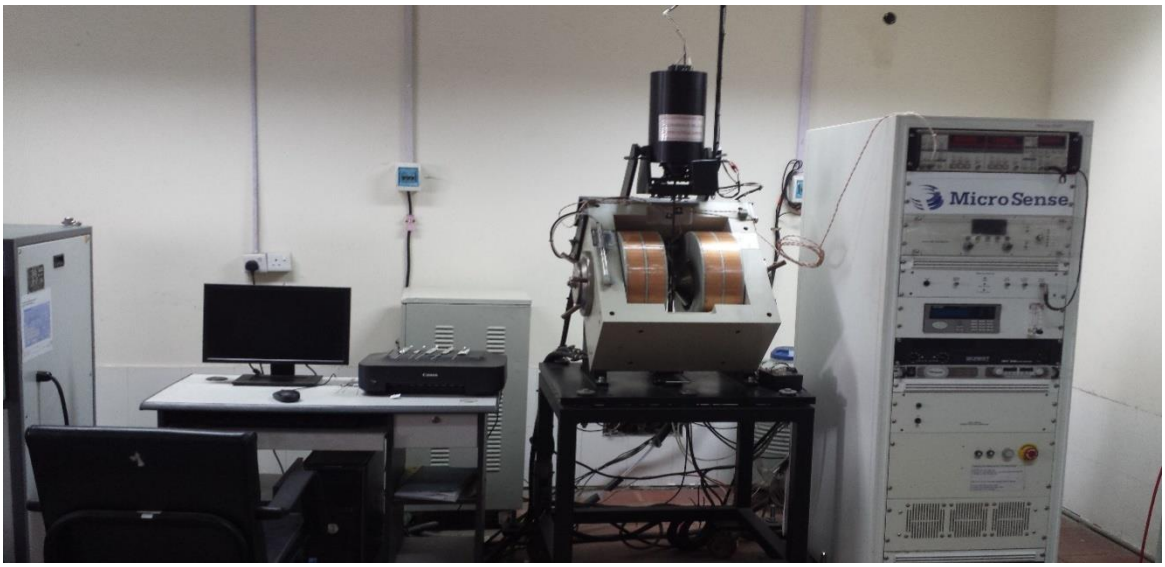

Fig. 4.3: Vibrating sample magnetometer at Atomic Energy Commission, Dhaka.

4.1.6 Study of Transport Properties

4.1.6.1 Dielectric Measurements

There are various polarizations, and each one has a physical mechanism that can be used to explain it. Electronic, ionic, and orientation polarizations are the three fundamental types. When an insulator is exposed to an external electric field, the atoms' electrons are somewhat dislocated from their nuclei. This results in induced dipole moments, which are what give rise to electronic polarization. The electron clouds will be pushed eccentrically towards the direction of the more strongly bound atom when the atoms in a molecule do not share their electrons symmetrically. The ions then pick up charges with the opposite polarity. When an external electric field is present, these net charges have a tendency to shift the ions' equilibrium locations.

A second type of induced dipole moment is produced by the displacement of charged ions or clusters of charged ions relative to one another. It symbolizes the ionic polarization of the molecule's dissimilar partners, which results in permanent dipole moments that continue to exist even in the absence of an external electric field. In an electric field, such dipoles experience a torque that causes them to gravitate toward the field's direction. An orientation (or dipole) polarization may result as a result. These three polarization mechanisms are brought about by charges that are regionally bound in atoms, molecules, or solid structure. Along with all of these, charge carriers typically exist and have the ability to move through dielectrics over a short distance.

An impedance analyzer (6500B) manufactured by Wayne Kerr that was computer-controlled was used to measure dynamic (electrical and dielectric) transport qualities. The two surfaces of each pellet were covered with silver paint as contact material, and the pellet shaped samples were highly polished to remove any contamination from other oxides that may have formed on the surface during sintering. The Wayne Kerr impedance analyzer was used to measure the impedance (real and imaginary components directly) and the dielectric and ac conductivity as a function of frequency at ambient temperature. The formula was used to get the real portion of the dielectric constant [6-7]:

$$\varepsilon^{/} = \frac{Cd}{\varepsilon_o A}$$

where A is the area of the cross-section of the chosen paint patch in m^2, C is the capacitance of the pellet in Farad, d is its thickness in meter (m), and ε_0 is the permittivity constant for empty space.

The sample's imaginary portion of its dielectric constant was determined using, $\varepsilon^{//} = \varepsilon^{/} tan\delta;$ where $tan\delta$ denotes loss tangent of the dielectric. The relation was used to compute the ac conductivity.

$\sigma_{ac} = d/(A*R_{ac})$; here R_{ac} represents the ac resistance.

The majority of materials' electrical conductivity can be characterized as: $\sigma\ (\omega,\ T) = \sigma_{dc}(T) + \sigma_{ac}(\omega,\ T)$; where σ_{dc} is the only factor affecting dc conductivity is temperature. The second factor, which depends on both temperature and frequency, is ac conductivity (σ_{ac}). The empirical formula expresses the frequency-dependent: $\sigma_{ac}(\omega,\ T) = A\omega^{n}$; where A and n are constants that are temperature- and composition-dependent; A has units of σ_{ac}, whereas n has no dimensions.

4.1.6.2 Impedance Spectroscopy

Investigating the electrical characteristics of the complex oxides can be done well with the help of complex impedance spectroscopy. The technique's principal benefits include i) It entails comparatively straightforward electrical measurements that are easily mechanized, ii) Any electrodes can be used to carry out the measurements, iii) The composition, microstructure, flaws, dielectric characteristics, chemical response, etc. of the sample can often be connected with the results and iv) in the majority of polycrystalline samples, the resistance of the grain borders and that of the grains may be easily distinguished. The resistance R and capacitance C of the sample are measured and balanced against variable resistors and capacitors in a Wheatstone-bridge-style device (impedance analyzer or LCR meter) for AC measurements. Impedance spectroscopy is the process of measuring the impedance |Z| and the phase difference (θ) between the voltage and current as a function of frequency for the supplied sample. The impedance plot is a complex plane used to analyze data by graphing the imaginary part of the impedance Z/=|Z| $cos\theta$ versus the real part Z//=|Z|

$sin\theta$. The equivalent circuit is examined using a linear scale impedance plot as shown below. A pure capacitor's impedance plot is a straight line that coincides with the imaginary axis, while a pure resistor's impedance plot is a point on the real axis. The following relation can be used to express the impedance of a parallel RC combination:

$Z^* = Z^{/} - jZ^{//} = R / (1+j\omega RC)$

One obtains after simplification, $(Z^{/} - R/2)^2 + Z^{//2} = (R/2)^2$,

This provides the equation for a circle whose center is at (R/2, 0) and whose radius is R/2. This means that a semicircle with a radius of R/2 will result from a plot of Z' vs. Z// (as a parametric function of Ω The simple circuit's time constant is given as t = RC = 1/m. The characteristic frequency is located at the peak of the semi-circle and corresponds to the sample's relaxation time. The impedance curve in a perfect polycrystalline sample shows an arc at high frequency relating to the sample's bulk property, an arc at low frequency due to the behavior of the grain boundaries, and a spike at the lowest frequency corresponding to the electrode effect.

4.1.6.2 *Modulus Spectroscopy*

The complex modulus spectroscopy study is a useful and potent technique in materials research that provides essential information on the distribution parameters of various nano areas in nano-crystalline materials, such as electrode interface , grain boundary, and grain. By graphing the modulus at various frequencies in a complex plane, distinct mechanisms involved in the relaxation and ac conduction process may be elucidated. This method is also particularly successful in differentiating the contributions of the grain and grain boundary effect. Additionally, the separation of components with identical resistance but varied capacitance can be accomplished with the help of a modulus spectroscopic plot. The electrode effect is reduced, which is another benefit of the electric modulus formalism. Complex

electric modulus formalism has been used for the aforementioned reasons. Studies on dielectric relaxation using the complex modulus M* formalism have been done. From the impedance measurements, the real and imaginary components of the electric modulus were calculated according to the relationship:

$M^{/} = \varepsilon' / (\varepsilon'^2 + \varepsilon''^2) = \omega C_0 Z''$ and $M^{//} = \varepsilon'' / (\varepsilon'^2 + \varepsilon''^2) = \omega C_0 Z'$.

4.2 Conclusions

In this chapter, fundamental experimental methods for determining the lattice parameters and frequency-dependent electric and dielectric characteristics of ferrite nanoparticles are covered in depth. Using the FESEM measurement instrument, measurements of surface morphology and nanostructure were made. The samples' physical characteristics were assessed using XRD. To measure the magnetic hysteresis, a VSM was employed. Using the impedance analyzer, two probe methods were used to measure the structural transport parameters. All the experiments were done with care to satisfy the theoretical ideas.

References:

[1] J. A. Mydosh, Spin Glasses: An Experimental Introduction, Taylor and Francis, London Washington, DC, 1993.

[2] A. K. Nikumbh, A. V. Nagawade, G. S. Gugale, M.G. Chaskar, P.P. Bakare, J. Mater.Sci. 37 (2002) 637.

[3] J. B. Nelson, D. P. Riley. Proc. Phys. Soc. London. 57 (1945)160.

[4] T. L. Templeton, A. S. Arrott, A. E. Curzon, M. A. Gee, X. Z. Li, Y. Yoshida, P. J. Schurer, J. L. Lacombe. J. Applied Phys. 73 (1993) 6728.

[5] A. Goldman,Handbook of Modern Ferromagnetic Materials, Kulwer Acad. Pub, Boston, USA, 1999.

[6] P. A. Shaikh, R. C. Kambale, A. V. Rao, Y. D. Kolekar. J. Alloys. Compd. 482 (1-2) (2009)276.

[7] R. C. Kambale, P. A. Shaikh, C. H. Bhosale, K. Y. Rajpure, Y. D. Kolekar. J. Smart Mat. Structr. 18(8) (2009) 085014.

Chapter 5

Results and Discussion

5.1 Characterization of $Ni_{0.5}Cu_{0.2}Cd_{0.3}Fe_{2-x}Al_xO_4$

The sol gel auto combustion method is used to synthesize nanoparticles of $Ni_{0.5}Cu_{0.2}Cd_{0.3}Fe_{2-x}Al_xO_4$ (x = 0.00, 0.015, 0.03, 0.045, 0.06, 0.075). The synthesized powders are annealed at 700 ℃ for 5hr and study of their structural, magnetic and electrical transport properties. XRD and FESEM techniques are used to study of the nanostructure, surface morphology etc. Electrical transport properties are measured by impedance analyzer, whereas VSM is used to illustrate the magnetic properties.

5.1.1 Physical Properties

5.1.1.1 *Structural Characterization*

Fig. 5.1(a) shows the XRD pattern of all compositions in $Ni_{0.5}Cu_{0.2}Cd_{0.3}Fe_{2-z}Al_zO_4$ annealed at 700 ℃. To study nanostructure, the XRD technique is used, which ensures the prime and deterministic condition of any research. There appear various characteristic diffraction peaks of each composition due to the fundamental reflections originating from the planes of (111), (220), (311), (222), (400), (422), (511) and (440) with no secondary peaks. The most intense peaks appear due to reflection from the plane (311) in each composition. The height of peaks become broader (Fig. 5.1(b)) with increasing Al content in the composition indicating smaller crystallite size, which makes Al an important element to get smaller crystallite as well as to enhance the crystalline properties. The observed sharp peaks comply with the reference value and confirm the structure of spinel formation for every sample and indicate a precise crystalline homogeneous structure [1]. From Fig. 5.1, the appearance of broader peaks represents the nanocrystalline nature of the synthesized powders. The background data shows the crystallite size (D_{XRD}) of all compositions obtained from XRD analysis lies in the nano-

scale range. The D_{XRD} and D_{FESEM} (discuss later) variation with Al content in the samples tabulated in Table 5.1, which show a decreasing trend of *D*.

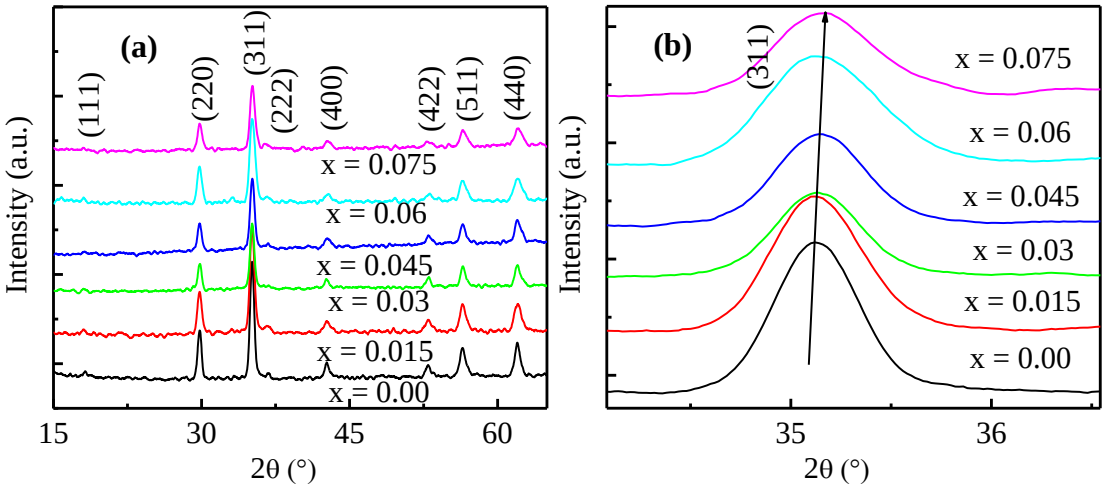

Fig. 5.1 (a) Pattern of XRD and (b) $Ni_{0.5}Cu_{0.2}Cd_{0.3}Fe_{2-x}Al_xO_4$ annealed at 700ºC and prolonged (311) peak. (JCPDS card number 90–09922).

Table 5.1 Lattice constant variation (a_o) and crystallite size of $Ni_{0.5}Cu_{0.2}Cd_{0.3}Fe_{2-x}Al_xO_4$

Al content	Lattice constant (*Å*)	Lattice constant (*Å*) by Rietveld method	χ^2	D_{XRD} (nm)	D_{FESEM} (nm)	D_{W-H} (nm)	Micro Strain
0.00	8.483	8.4751	1.43	21	99	22	0.00196
0.015	8.476	8.4761	1.40	20	77	21	0.00536
0.030	8.466	8.4726	1.22	20	75	20	0.0019
0.045	8.460	8.4723	1.31	20	69	29	0.00871
0.060	8.449	8.4720	1.45	18	61	18	0.00896
0.075	8.443	8.4676	1.23	16	46	16	0.14065

The XRD data of all samples are analyzed by the Rietveld refinement procedure. The outcomes are demonstrated in Fig 5.2. Each of every Rietveld fitted patterns for all samples are sequentially represented in Fig. 5.2(a) to Fig. 5.2(b).

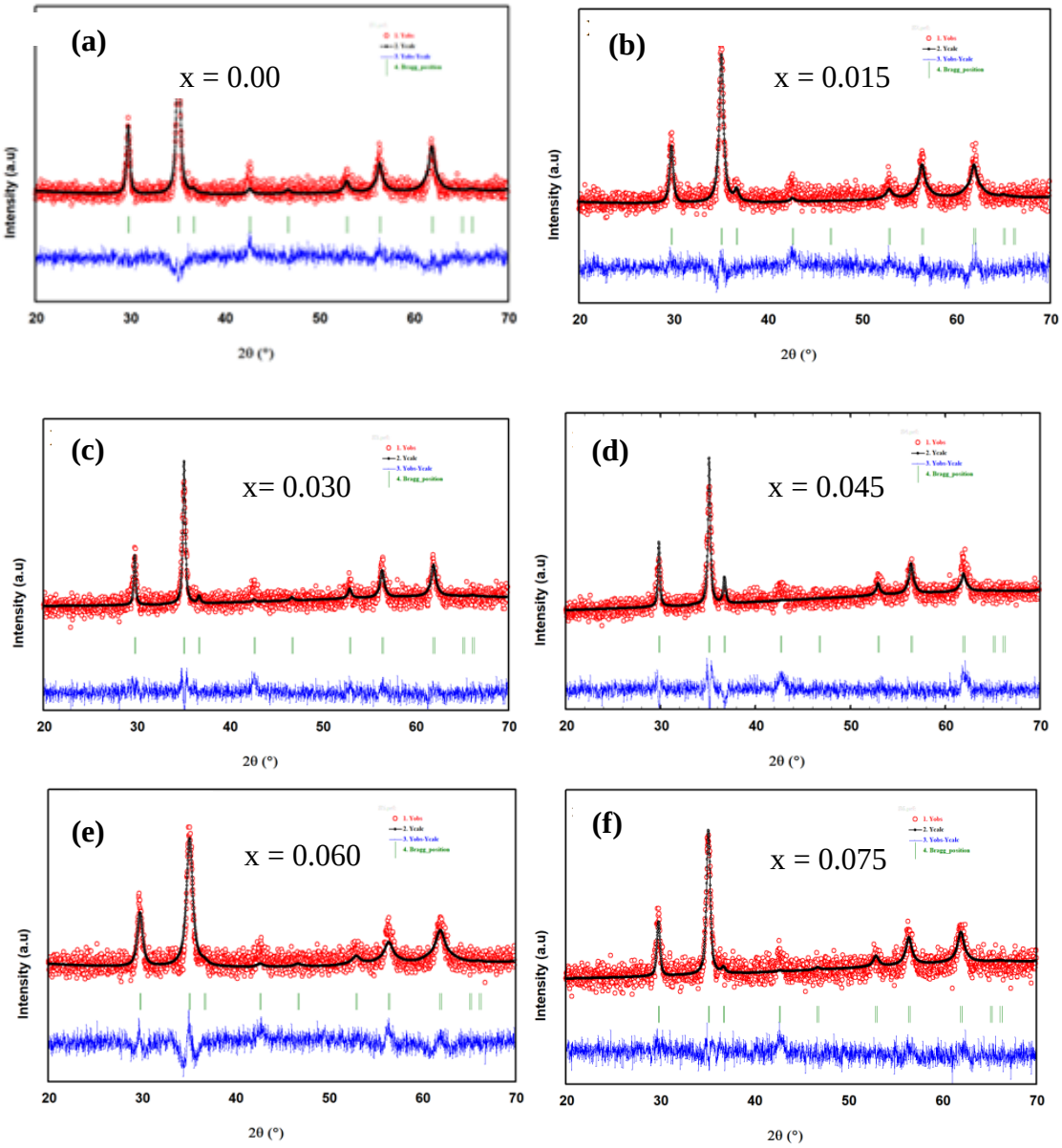

Fig. 5.2 Rietveld refinement of $Ni_{0.5}Cu_{0.2}Cd_{0.3}Fe_{2-x}Al_xO_4$.

This structural analysis of all compositions ensures their characteristics and obtained parameters are also indicated in the graphical representation. As less than 2 values of χ^2 known as the goodness of fit are considered as best fitting, these findings suggest good agreement for the XRD pattern [2]. Besides, cubic phase with space group Fd-3m has been confirmed through the Rietveld refinement. Furthermore, the doping of Al on ferrites reveals some changes in lattice parameters and listed in provided Table with other parameters such as volume and goodness of fit. From Table 5.1 it is evident that the lattice parameter has been

reduced slightly as the amount of Al substitution is increased. As a result, volumes of the unit cell of spinel ferrite structure are decaying by the reduction of Fe^{3+} ions. The reason behind this reduction may be a compressive strain of composition. The variation of microstrain can be seen from the data in Table 5.1. The ferromagnetic characteristics, as well as the magnetic properties of these nanoparticles, can be affected by this parameter [3].

The preferences of cations for A and B site are determined from the outputs of Rietveld Refinement [4] and listed in Table 5.2.

Fig. 5.3 shows the variation in lattice constant (a_0) of $Ni_{0.5}Cu_{0.2}Cd_{0.3}Fe_{2-z}Al_zO_4$ as a function of Al substitution in the compositions. It is observed that the a_0 reduces with rising Al content, which can be interpreted with the difference in ionic radius
between Fe^{3+} (*0.67Å*) and Al^{3+} (*0.55Å*) [5].

Table: 5.2 Distribution of Cation of $Ni_{0.5}Cu_{0.2}Cd_{0.3}Fe_{2-x}Al_xO_4$.

Al content	Composition	Cation Distribution
0.00	$Ni_{0.5}Cu_{0.2}Cd_{0.3}Fe_2O_4$	$(Ni_{0.29}Cu_{0.13}Cd_{0.13}Fe_{0.438})_A[Ni_{0.21}Cu_{0.07}Cd_{0.17}Fe_{1.562}]_BO_4$
0.015	$Ni_{0.5}Cu_{0.2}Cd_{0.3}Fe_{1.985}Al_{0.015}O_4$	$(Ni_{0.27}Cu_{0.13}Cd_{0.13}Al_{0.007}Fe_{0.458})_A$ $[Ni_{0.23}Cu_{0.07}Cd_{0.16}Al_{0.008}Fe_{1.527}]_BO_4$
0.030	$Ni_{0.5}Cu_{0.2}Cd_{0.3}Fe_{1.97}Al_{0.03}O_4$	$(Ni_{0.29}Cu_{0.13}Cd_{0.14}Al_{0.001}Fe_{0.438})_A$ $[Ni_{0.21}Cu_{0.07}Cd_{0.16}Al_{0.029}Fe_{1.532}]_BO_4$
0.045	$Ni_{0.5}Cu_{0.2}Cd_{0.3}Fe_{1.955}Al_{0.045}O_4$	$(Ni_{0.24}Cu_{0.13}Cd_{0.14}Al_{0.005}Fe_{0.485})_A$ $[Ni_{0.26}Cu_{0.07}Cd_{0.16}Al_{0.040}Fe_{1.470}]_BO_4$
0.060	$Ni_{0.5}Cu_{0.2}Cd_{0.3}Fe_{1.94}Al_{0.06}O_4$	$(Ni_{0.29}Cu_{0.14}Cd_{0.13}Al_{0.006}Fe_{0.437})_A$ $[Ni_{0.21}Cu_{0.06}Cd_{0.17}Al_{0.054}Fe_{1.503}]_BO_4$
0.075	$Ni_{0.5}Cu_{0.2}Cd_{0.3}Fe_{1.925}Al_{0.075}O_4$	$(Ni_{0.29}Cu_{0.13}Cd_{0.13}Al_{0.006}Fe_{0.439})_A$ $[Ni_{0.21}Cu_{0.07}Cd_{0.17}Al_{0.069}Fe_{1.501}]_BO_4$

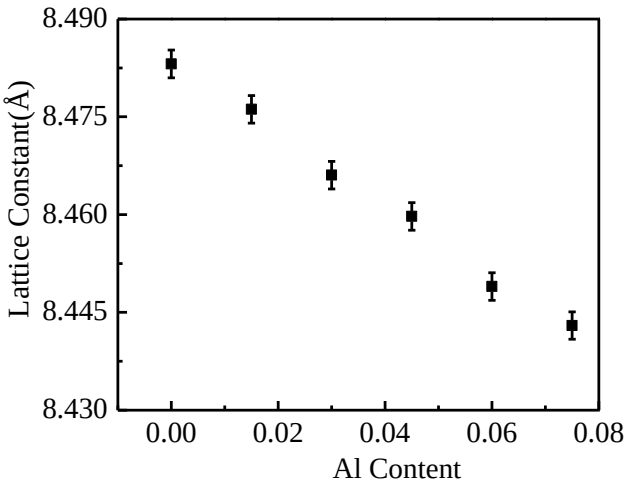

Fig. 5.3 Changes in the lattice constant of $Ni_{0.5}Cu_{0.2}Cd_{0.3}Fe_{2-x}Al_xO_4$ with Al content.

5.1.1.2 *Surface morphology and Nanostructure of* $Ni_{0.5}Cu_{0.2}Cd_{0.3}Fe_{2-x}Al_xO_4$

Fig. 5.4(a) to Fig. 5.4(f) are used to study the surface morphology of the samples with Al content x = 0.00 to x = 0.075 respectively. The surface morphology gives visibly the type of grain growth and the average size of a grain of each composition and can be determined from FESEM analysis and its impacts on physical, electrical and magnetic behaviours of the synthesized nanoparticles [6, 7]. The grain size and grain boundary are two important parameters in nanotechnology that cause exotic properties owing to the limited size and surface impacts. The FESEM nano-graphs of $Ni_{0.5}Cu_{0.2}Cd_{0.3}Fe_{2-z}Al_zO_4$ have been shown in Fig. 5.4. According to the observed morphology, the fine particles in the compositions with narrow size distribution are without any impurity under the annealing process. The grains of various sizes and shapes are detached with grain boundaries with some agglomerations are appeared in Fig. 5.4. Accordingly, the nano-sized grains are spherical and distributed homogeneously. The D_{XRD} measured using FESEM nano-graphs by the imaging technique to be a similar trend and matched well with the XRD results for the studied compositions. The estimated D_{FESEM} [8] lies in the range of (99–46) nm for annealing at 700 ℃.

The separation between grains and grain boundaries is clearly visible for all synthesized samples in annealing temperature. The average grain size i.e., the crystallite size of each composition decreases with the substitution of Al^{3+}. It may be attributed to the difference in melting and boiling point of iron (1535 ℃, 2750 ℃) and aluminium (660.37 ℃, 2467 ℃).

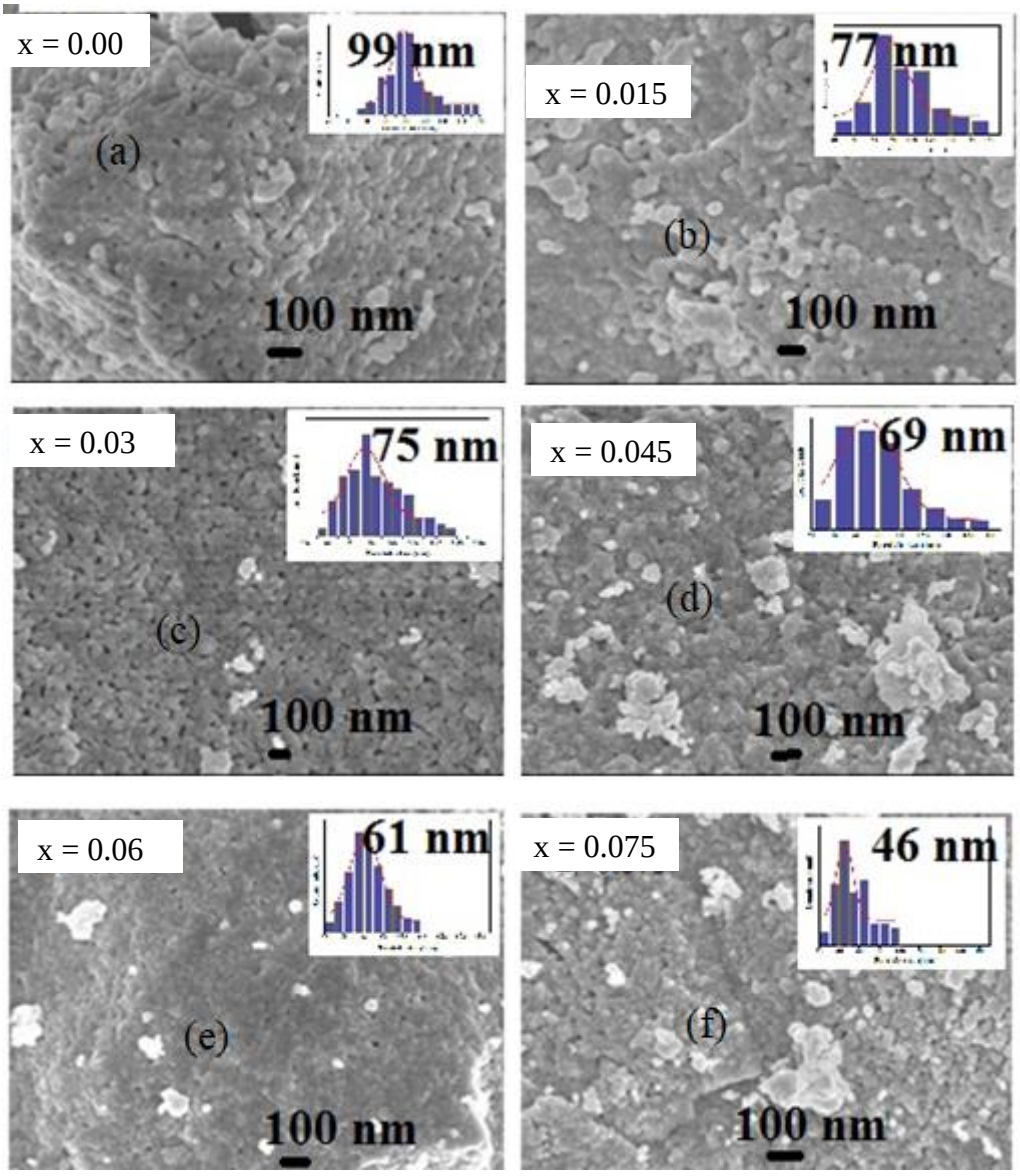

Fig. 5.4 FESEM nano-graphs of $Ni_{0.5}Cu_{0.2}Cd_{0.3}Fe_{2-x}Al_xO_4$ annealed at temperature 700 ℃.

5.1.2 Magnetic Properties

5.1.2.1 Magnetization Hysteresis

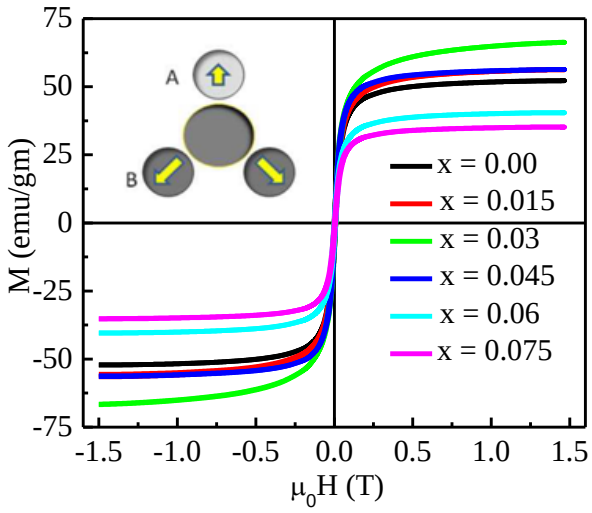

Fig. 5.5 Variation of M with H for various of $\mathbf{Ni_{0.5}Cu_{0.2}Cd_{0.3}Fe_{2-x}Al_xO_4}$.

The magnetic hysteresis behaviour of the synthesized nanoparticles has been observed with VSM with an applied field of 1.5 T (in $\mu_0 H$) at room temperature to reach the value of saturation. The observed hysteresis loops have been presented in Fig. 5.5. The change in magnetization with the applied magnetic field (M-H) for different compositions at room temperature can be observed in Fig. 5.5. It is noticed that the magnetization of all the compositions initially rises sharply along with a rising external field (H) up to 0.25T (in $\mu_0 H$) and then it attains saturation (M_s). The values of M_s with theoretical and experiment magnetic moments for samples are given in Table 5.3. It is also clear from

Fig. 5.5 that M_s increased up to x = 0.03 beyond which it reduces with Al content rises. The same behaviour of soft ferrites with Al substitution can also be observed [9]. This type of variation in M_s with Al^{3+} content can be interpreted based on the distribution of cation with exchange interaction over A- and B- sites which influence the magnetic behaviours of ferrite nanoparticles. By applying Hund's rule with magnetic moment (μ_B) and Al^{3+} ($0\mu_B$), Ni^{2+} ($2\mu_B$), Cu^{2+} ($1\mu_B$), Cd^{2+} ($0\mu_B$) and Fe^{3+} ($5\mu_B$), the cations can be distributed on A site and B

site by considering Table 5.2 where all cations are placed in their respective positions from Rietveld analysis [10]. The total μ_B decreases at the B- site with increasing Al^{3+} content instead of Fe^{3+} in the B-site. The μ_B of Al^{3+} and Fe^{3+} reference value and the change in magnetization at B-site is expected because B-site occupies non-magnetic trivalent Al^{3+} content and therefore the total magnetization $(M_S = M^B - M^A)$ decreases ultimately by diminishing the B-A interaction in these ferrite nanoparticles. As reported in [11] and established in many research-works that any level of Al concentration, Al^{3+} prefers to accumulate them in B-site. So, the total magnetic moment, as well as M_s, are found to be decreased with Al^{3+} substitution beyond the value of x = 0.03 [Fig inset of 5.5], which can be explained on the basis of this migration of Fe^{3+} from B site to A site.

The comparison between theoretical and experimental numbers (n_{th} and n_{ext}) of μ_B with Al^{3+} substitution has been shown in Table 5.3. Assuming anti-parallel interaction, theoretical μ_B is estimated by equation (7),

$$n_{th} = (M_1B - M_1A)\mu_B B \quad \text{.....(7)}$$

for different values of Al^{3+} content using ionic magnetic moment and cation distribution of Cu^{2+}, Cd^{2+}, Al^{3+} and Fe^{3+}. The formula of equation (8), was used to calculate the experimental number μ_B.

$$n_{\exp(\mu_B)} = \frac{M_A X \quad M_B}{5585} \qquad n_{\exp(\mu_B)} = \frac{M_w X M_s}{5585} \quad \text{..... (8)}$$

The deviation between n_{th} and n_{ext} may be due to the reason that the theoretical number of μ_B was calculated at 0 K, but the experimental values of μ_B were determined at room temperature (at 300 K). From Table 5.3, the theoretical magnetron number reduces but the experimental values rise to x = 0.03 and then reduce with the rise in Al^{3+} substitution. From Table 5.3, it is found that the substitution of magnetic Fe^{3+} by nonmagnetic Al^{3+} at B-site is the main cause of linear reduction of M_s. Al^{3+} does do not involve in the swap interaction to the nearest

neighbour ions as it is a nonmagnetic ion, the magnetization reduces at B-site as well as the net saturation magnetization reduce in A-B $M_s = M_B \cos\gamma - M_A$ interaction. We can interpret the enhancement of M_s using the relation; where the M_s firstly increases due to the canting angle decreased. When the canting angle γ appears lower i.e. increases cosγ and magnetization increases at the saturation point up to x = 0.03. It is due to Al^{3+} is smaller in size than Fe^{3+} that is also observed from XRD analysis. Hence, the substitution of smaller ion increases A-B exchange interaction by decreasing the distance between the magnetic cations. As a result, the canting angle decreased [12]. Further increase of Al content, the M_s decreases due to Al^{3+} increases beyond $x \geq .03$ reduces magnetic moment more in the B site compared to the increased exchange interaction. The table 5.3 shows the percentage (%) of magnetization (M_s) and using this M_s, x = 0.03 is 66.36 which is 1.3 times greater than the mother composition, (M_s= 52.2). μ_B shows a similar trend of M_s values.

Fig. 5.6 shows the representative curves of M_s fitted to law of approach to saturation (LAS) for all compositions [5] of present investigated samples from x = 0.00 to x = 0.075 to determine the M_s. The expression for the LAS is given by Eq. (9)

$M = M_s\{1-(8k_1^2/105M_S^2H^2)\}$…… (9)

The values of B and M_s are obtained from the M–H fitted curve and K_1 is called the cubic anisotropic constant which is calculated by Eq. (10),

$k_1 = M_s\sqrt{(105B/8)}$ ……. (10)

where B is anisotropy constant. All observed curves are fitted well with the theoretical LAS curves and fitted parameter M_s is obtained from this method and listed in Table 5.3.

Table 5.3 Magnetic Characteristics like Ms, Ms from LAS and experimental Magnetic Moment

Al Content (x)	Saturation magnetization [Ms(emu/gm)]	Ms (emu/gm) from LAS	Experimental Magnetic moment (μ_B)
0.00	52.2	52.35	2.3503
0.015	56.26	56.82	2.5287
0.030	66.36	67.5	2.9775
0.045	56.29	57.03	2.5213
0.060	40.46	41.05	1.8091
0.075	35.21	35.35	1.5691

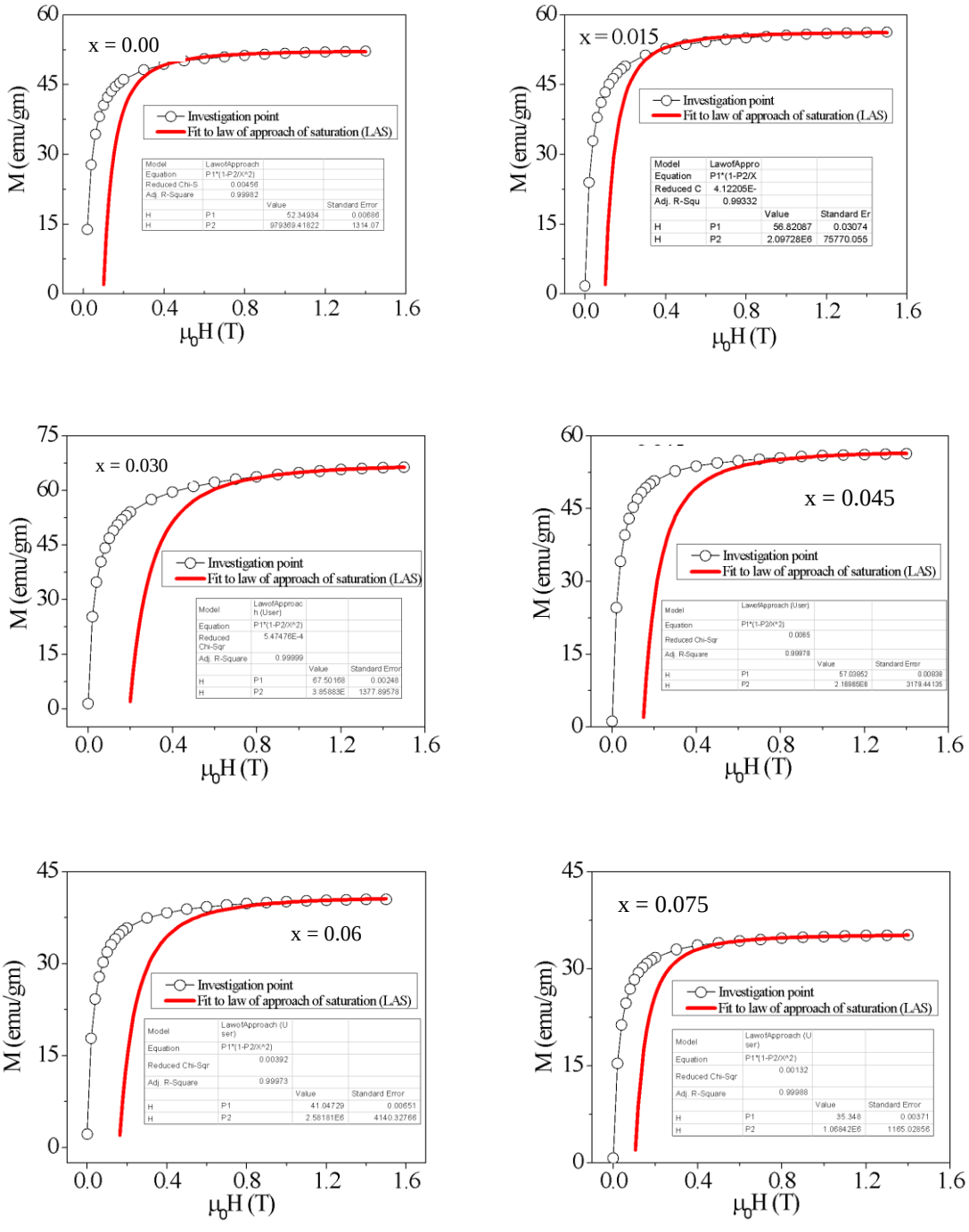

Fig. 5.6 Fitted curves of LAS for all compositions.

5.1.3 Electrical Transport Properties

5.1.3.1 *Dielectric Study*

The reflections in ε′ and ε″ of the dielectric constant of $Ni_{0.5}Cu_{0.2}Cd_{0.3}Fe_{2-z}Al_zO_4$ ferrite nanoparticles with a frequency range of 20 Hz -15 MHz have been shown in Fig. 5.7(a,b). At lower frequencies (in kHz region/of order ~ 10^3), the values of ε′ and ε″ are much higher and the values are so small at high frequencies and become almost distinct from the frequency [13, 14]. Therefore, these materials possess high dielectric values which are due to space charge polarization. The creation of grains with semiconducting nature occurs at the time of synthesis of ferrites nanocrystals, these adjacent grains are separated by thin layers with insulating character and therefore they act as dissimilar dielectric materials. Again, the creation of Fe^{2+} from Fe^{3+} also takes place in these ferrites. It is clear from the observed behaviour of ε′ and ε″ that energy dissipation term decreased rapidly as well as with Al content. Polarization of space charge is caused due to the existence of semiconducting phases as grains in the non-conducting medium as grain boundaries of a dielectric and creates a confined accumulation of charges under the impact of an ac electrical field [15]. Space charge carriers assemble in a dielectric substance brings a fixed time to follow up their axes which is parallel to an ac electric field. With increasing frequency, a point is attained where the carriers of space charge cannot maintain with the field, as the frequency of the field reversal raises and the repetition of their direction goes backwards than the field which causes reduction of dielectric values [15]. The behaviour of the dielectric constant can also be described according to the two-layer model of Maxwell and Wagner. Accordingly [16, 17], the interfacial polarization is due to the dissimilar dielectric structure of the material. This structure is created by large semiconducting grains which are separated by thin intermediate insulating grain boundaries. According to Rankin and Novikova [18], polarization in ferrites is similar to the conduction process. Electronic exchanges between $Fe^{2+} \leftrightarrow Fe^{3+}$ consequences

are confined of electrons in the direction of the applied field, which establishes polarization. As frequency rises, the polarization reduces and then attains a constant value, because it exceeds the specific frequency of the outward field, the electronic interchange between $Fe^{2+} \leftrightarrow Fe^{3+}$cannot go along with the alternating field. This is due to the majority of Fe^{2+} ions, grain boundary defects, oxygen vacancies, voids, interfacial displacement piles etc. [19-21]. Since the frequency rises, the decreasing tendency of the dielectric constant is normal due to which the species donating to the polarizability are found far behind the applied field at upper frequencies [20].

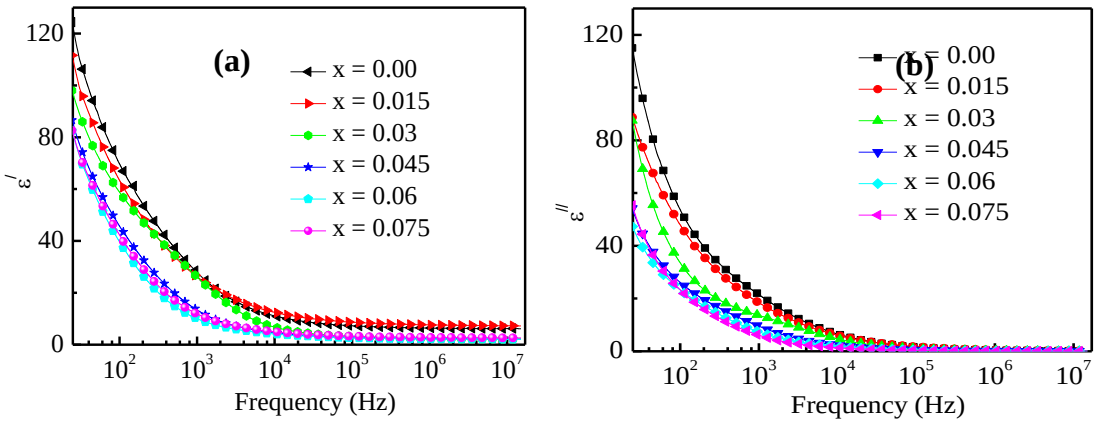

Fig. 5.7 Changes of ε′ (a)and ε″ (b) as based on the frequency for $Ni_{0.5}Cu_{0.2}Cd_{0.3}Fe_{2-x}Al_xO_4$ ferrite nanoparticles annealed at 700 °C.

Fig. 5.8 indicates the change in $tan\delta$ with frequency. The early reduction of $tan\delta$ with increasing frequency could be explained with hopping frequency. Accordingly, when the applied field frequency approaches close to the frequency of the hopping charge carrier, the highest value of $tan\delta$ at a particular frequency is attained. In the assessed frequency (20 Hz–15 MHz), all samples show Debye relaxation. With the Reslescu model, we can explain the features of loss tangent with frequency [21]. The combination of the frequency of the external field and the frequency of the hopping charge of the exchange ions creates a resonance peak or Debye relaxation. A small shift in maxima can be observed at higher frequencies. The peak

height also depends on Al-doping. The nature of this peak can be observed if the applied field frequency is almost equal to the jumping frequency of the electron between Fe^{2+} and Fe^{3+}. Maxima shift toward lower frequency regions with Al-doping, reveals that the possibility of jumping raises. Resistivity increased for the decrease of the Fe^{3+}/Fe^{2+} pairs in the conduction process. Hence the zenith of the peak increases with Al-doping.

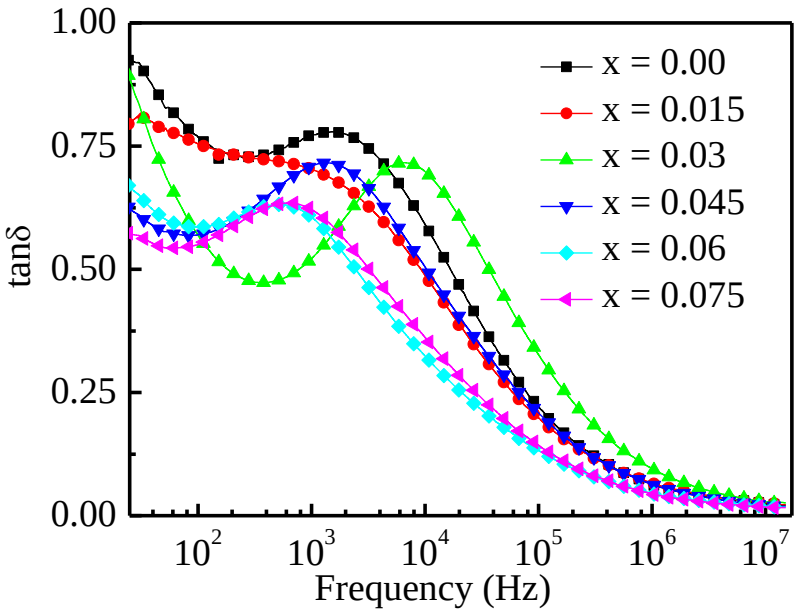

Fig. 5.8 *tanδ* of $Ni_{0.5}Cu_{0.2}Cd_{0.3}Fe_{2-x}Al_xO_4$ with frequency.

5.1.4 AC conductivity

The variation of electrical conductivity as a function of frequency (σ_{ac}) obtained at room temperature has been shown in Fig. 5.9. The σ_{ac} increases with the increase of frequency for all samples. This is a general behaviour of ferrites. Due to the hopping of charge carrier between same elemental ions, electrical conductivity in ferrites mainly depends upon multiple valence states, crystallographic equivalent random distribution at nearest neighbour lattice sites. The distance of hopping between two metals ions on A-sites (0.357 nm) is greater than the distance of hopping between two metal ions on B-sites (0.292 nm). So, hopping on B-sites has more potential than hopping between A- and B-sites. Fe^{3+} at A-sites and Fe^{2+} at B-sites, so A–A sites hopping does not occur [22]. The charges drift under the control of the

applied field, donating to the electrical reaction of the scheme. In the case of hopping conduction which rises with frequency and in the case of band conduction, the conductivity reduces with frequency [23]. The relation between conductivity and frequency is given by equation (11),

$$\sigma_{tot} = \sigma_0 (T) + \sigma (\omega, T) \ldots\ldots\ldots\ldots\ldots\ldots\ldots\ldots\ldots\ldots\ldots\ldots (11)$$

Here, the initial term ($\sigma_0 (T)$) is for band conduction which is the dc conductivity and it does not depend on frequency. The other term ($\sigma (\omega, T)$) is for the hopping method at the B site which is the σ_{ac} and it is a function of frequency. The initial term is mainly significant at high temperature and low frequencies whereas the second term is mainly significant at low temperature and high frequencies. For the 2nd term, it is written as experimental formula [24] as the part of the conductivity as given by equation (12),

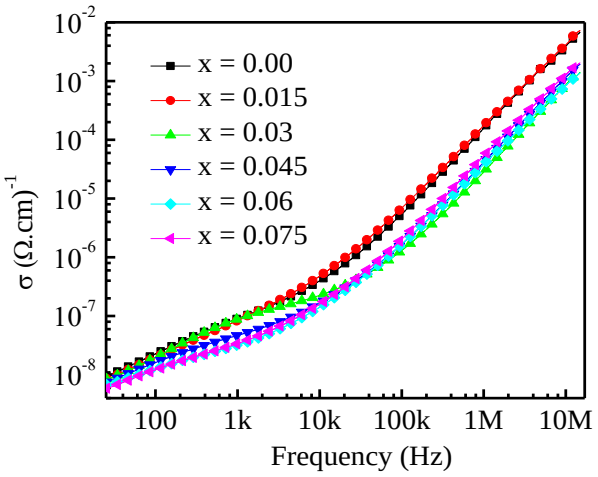

Fig. 5.9 Changes of ac conductivity with frequency.

$$\sigma_{ac} = S\omega^n \ldots\ldots\ldots\ldots\ldots\ldots\ldots\ldots\ldots\ldots\ldots\ldots (12)$$

where S is a constant angular frequency, ω (= 2πf) and "n" is the angular frequency and an exponent respectively. In the region where the conductivity rises firmly with frequency, the electrical transportation is controlled by hopping among infinite groups. The upper frequency cut off region begins with an electrical performance in the sample. The Electron-hopping

model is applicable for explaining the electrical conduction process. The conduction process is owing to the hopping of charge carrier between two nearby B-sites, $Ni^{2+} \Leftrightarrow Ni^{3+}$ or $Fe^{2+} \Leftrightarrow Fe^{3+}$ in the spinel lattice of the samples. If the frequency increases, the rate of hopping will also increase. As a result, increased conductivity is found in samples. In the case of the upper-frequency region, the σ_{ac} increased slowly with frequency for grain regions as the hopping frequency does not support the variations of the external field outside a certain limit of frequency [25]. It is observed that the σ_{ac} reduces with increasing Al content. As Al is a noble gas structure, it always forms trivalent ion for bonded with others and reduces the ferrous ion form i.e. hopping between $Fe^{2+} \Leftrightarrow Fe^{3+}$ decreased remarkably.

An idealized circuit model including distinct electrical components is applicable for impedance analysis in this system. The study is generally performed by matching the impedance data to a comparable circuit for investigating material. It is a very useful investigating technique as grain boundaries and electrode effects arise in this case [26,27]. In the Cole-Cole plot, two adjacent semicircles are seen; the first semicircle with a low-frequency region signifies grain boundary resistance and the second smaller semicircle with a high-frequency region signifies grain resistance. This usually correlates to the presence of dispersal behaviour in relaxation time.

5.1.5 *Impedance Analysis*

Fig. 5.10(a) and Fig. 5.10(b) are represented the real part and imaginary part of complex impedance. For an applied frequency the complex impedance (with real, Z′ and imaginary part, Z") is given by equation (13),

$$Z^*(\omega) = Z'(\omega) + iZ''(\omega) \quad \ldots\ldots\ldots\ldots\ldots\ldots\ldots\ldots\ldots\ldots\ldots\ldots\ldots\ldots (13)$$

$$\text{where, } Z' = R_g/(1+\omega_g C_g R_g)^2 + R_{gb}/(1+\omega_{gb} C_{gb} R_{gb})^2 \quad \ldots\ldots\ldots\ldots\ldots\ldots\ldots\ldots\ldots\ldots\ldots\ldots\ldots\ldots (14)$$

$$\text{and } Z'' = R^2_g/[1+(R_g\omega_g C_g)^2] + R^2_{gb}/[1+(R_{gb}\omega_{gb} C_{gb})^2] \quad \ldots\ldots\ldots\ldots\ldots\ldots\ldots\ldots\ldots\ldots\ldots\ldots\ldots\ldots (15)$$

Here, R_g signifies resistance and C_g signify capacitance for the grain structure and R_{gb} and C_{gb}

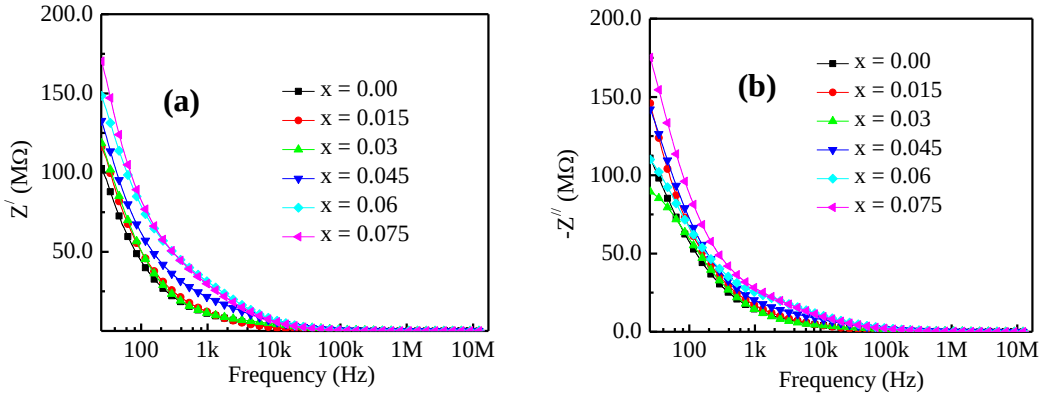

Fig. 5.10 Changes of the real part of impedance (a) and imaginary part of impedance (b) as a function of frequency for $Ni_{0.5}Cu_{0.2}Cd_{0.3}Fe_{2-x}Al_xO_4$.

signify respective parameters for the grain boundary. ω_g and ω_{gb} are the frequencies at the grain semicircular peak and grain boundary semicircular peak respectively in equation (14) and equation (15).

The resistances are computed from the Z' axis interception of circular arcs while capacitances are obtained from the maximum altitude of the circular arcs. In each semicircle, the maximum altitude is Z' = -Z''; so, by using this and the above equations, the capacitance for the grain and capacitance for the grain boundary can be calculated. The relaxation times for grain and grain boundary are given by equation (16) and equation (17) respectively,

$$1/\omega_g = C_gR_g \ldots\ldots\ldots\ldots\ldots\ldots\ldots\ldots\ldots\ldots\ldots\ldots\ldots\ldots (16)$$

$$1/\omega_{gb} = C_{gb}R_{gb} \ldots\ldots\ldots\ldots\ldots\ldots\ldots\ldots\ldots\ldots\ldots\ldots\ldots\ldots (17)$$

Both Z' and -Z'' reduce as the frequency rises. The highest value of impedance is noticed for the composition with maximum Al content (z = 0.075). This means that the conductivity is lowered there. Fig. 5.10 indicates the disparity of sensitive parts with the frequency of impedance for all compositions within room temperature.

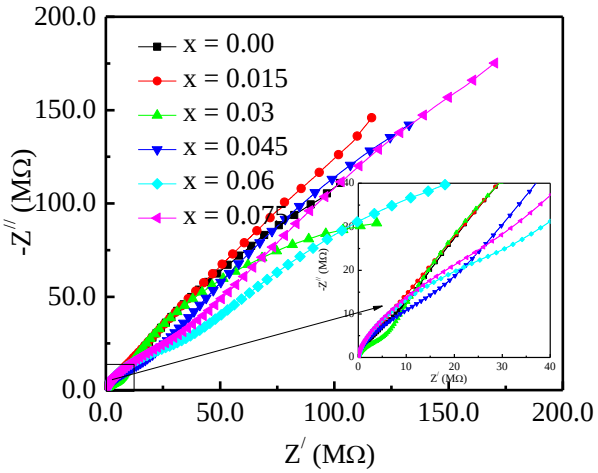

Fig. 5.11 Cole-Cole plots of impedance for$Ni_{0.5}Cu_{0.2}Cd_{0.3}Fe_{2-x}Al_xO_4$ annealed at 700°C.

For separating the contributions from grain boundary and grain, complex impedance plots or Cole-Cole plots are achieved by plotting Z' and -Z''. From Fig. 5.11, it is clear that one full semicircle is for the grain conduction and one incomplete semicircle is for the grain boundary conduction. The resistance of grain boundary is beyond the measurement scale. The Cole-Cole plots for different compositions are shown in Fig. 5.12, where plots of the right column are representing R_{gb} values while plots of the left column are representing R_g values. The relaxation time constant is responsible for the semicircular arc separation. This type of behaviour of impedance spectrum involves the relaxation time distribution in the material. As time constant changes beyond 100 units, imbrications between grain resistance and grain boundary resistance are observed significantly. For grain and grain boundary contributions exhibit two semicircular arcs in the case of large particle size while for small-sized grain a single semicircular arc (though not seen) is found [28,29] and the magnitude of grain contributions can affect the semicircular size. From Cole-Cole fitting process, R_g, Grain Capacitances (C_g), R_{gb}, Grain Boundary Capacitances (C_{gb}) and corresponding relaxation

times (τ_g, τ_{gb}) with exponential powers are calculated and listed in Table 5.4. The semicircular arc at the low-frequency region expresses grain boundary parameters only and the semicircular arc at the higher frequency range expresses grain parameters. Table 5.4 reveals that grain resistances are increased at a higher frequency range while grain boundary resistances are increased at the low-frequency range with Al content. This behaviour is the same for all samples of $Ni_{0.5}Cu_{0.2}Cd_{0.3}Al_xFe_{2-x}O_4$. On the site of grain boundary, imperfections control the transport nature which leads larger contribution of grain boundary in the whole resistance. Hence grains are expected to have smaller concentrations than grain boundaries and thus participate in the impedance of inter-grain regions [11].

Table 5.4 Grain and Grain boundary parameters for $Ni_{0.5}Cu_{0.2}Cd_{0.3}Fe_{2-x}Al_xO_4$

Al content	R_g(MΩ)	R_{gb}(MΩ)	τ_g(ns)	τ_{gb}(ns)	α_g	α_{gb}
0.00	30.03	500	100	10	0.7	0.7
0.015	35.01	692	100	10	0.8	0.8
0.030	40.2	820	100	10	0.5	0.6
0.045	81	4020	100	10	0.6	0.5
0,060	91	1000	100	100	0.7	0.5
0.075	100	980	100	100	0.7	0.7

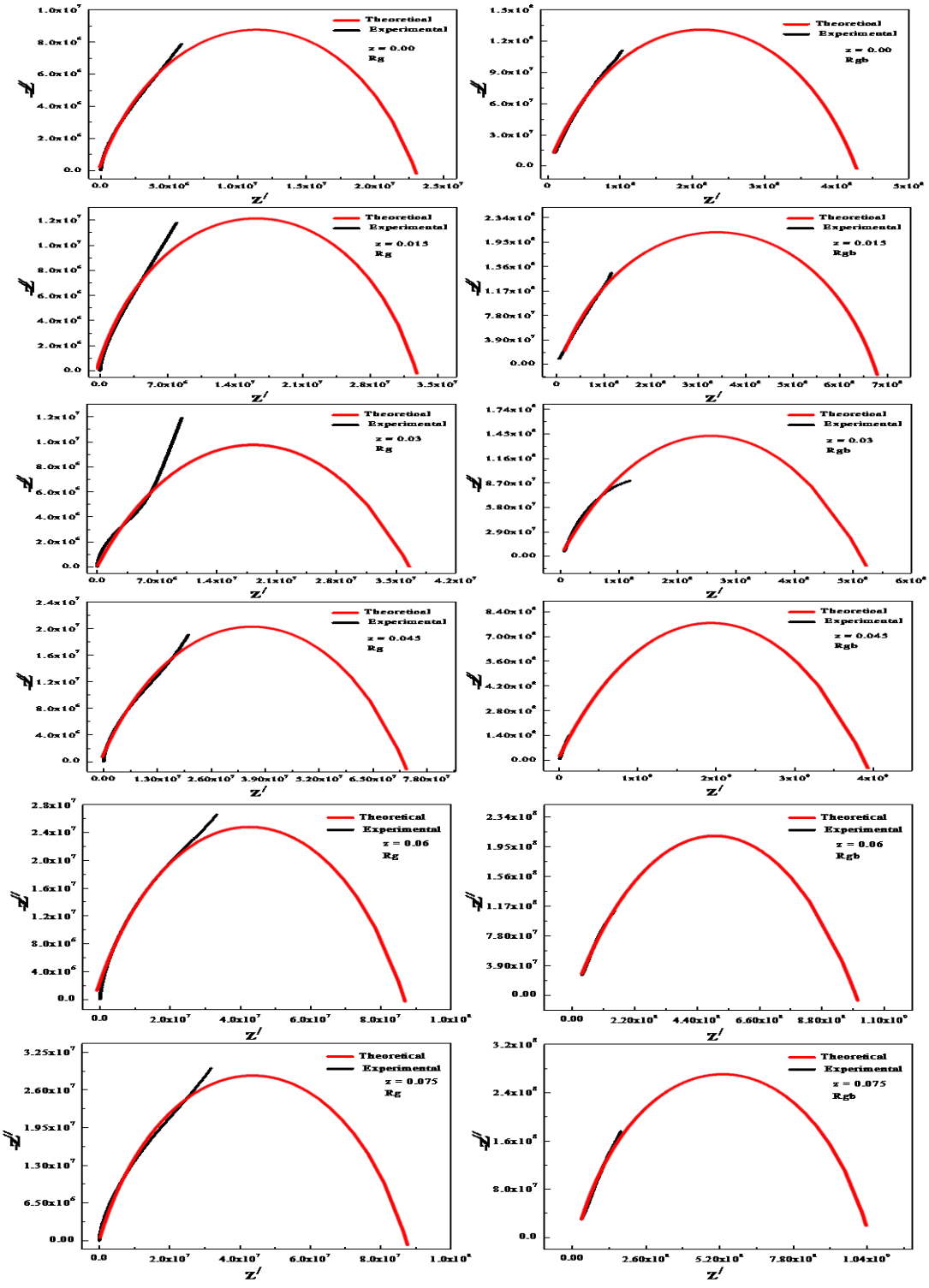

Fig. 5.12 Cole-Cole fitting for grain and grain boundary parameter of $Ni_{0.5}Cu_{0.2}Cd_{0.3}Fe_{2-x}Al_xO_4$.

5.1.6 *Electric Modulus Analysis*

The study of complex modulus is an effective method of investigating the electrical transport properties of the synthesized materials. It is also useful to observe other impacts that appeared

in the sample with the consequence of various relaxation time constants. To ascertain, assess and explain the dynamic characteristics of electrical transport properties (i.e. conductivity, ion hopping rate, time of relaxation etc.) the complex modulus is an important technique. It can discriminate with grain boundary conduction and electrode polarization procedures. In the case of studying various nanocrystalline ceramics, the analysis of electric modulus in the light of relaxation phenomena was also stated previously by many scholars [29-31]. The performance of imperfections can be distinguishable from the electrode effect corresponding to their bulk response employing this complex modulus approach [32]. The electric modulus relates to the electric field relaxation in the substances while the electric displacement stays constant. Generally, frequency-dependent complex electric modulus M^* can show important features like a broad unbalanced peak in the imaginary part and a sigmoidal performance in the real part [33].

For Ni-Cu-Cd-Al ferrite nanoparticles, the variation of frequency-dependent M′ (real part) and M″ (imaginary part) of complex electric modulus has been presented in Fig. 5.13 and Fig. 5.14 respectively. The M′ is very low at lower frequencies and after a particular range of frequency, it increases gradually and reaches its saturation value. The saturation of M′ values detected at the high-frequency side probably owing to the release of space charge polarization [34]. There appears the low value of M′ in lower frequency leading the conduction process due to extended range motion of charge carriers and the electrode polarization contribution in the material [35]. Besides, the M′ increase with the rise in Al content implies the polarization effects become remarkably lower i.e. reduces dielectric losses.

Fig. 5.14 displays the M″ of electric modulus versus frequency at room temperature. It is seen from Fig. 5.14 that M″ displays very lower values at lower frequencies and after a frequency of about 10 kHz, it increases rapidly and attains maximum for all the samples. It also observed that M″ shifts the location of the peak toward the higher frequency side as the Al content

increased. This offers clear information regarding processes of charge transport such as the system of electrical transport, ion dynamics and conductivity relaxation with frequency. The peak indicates the separation between long-range and short-range hopping mechanisms due to electron transfer. Charge carriers are capable to move long distances in frequency region (lower frequency) below the peak maximum whereas they are confined in potential wells and movable over short distances in the high-frequency side at above the peak maximum [36]. This type of modulus analysis suggests us a composition-dependent hopping like the mechanism of conduction in the electrical system. The widening of the peak indicates non-Debye relaxation in the material. The existence of a peak in the spectrum of modulus provides also a clear signal of relaxation of conductivity. The most feasible relaxation time (τ) can be calculated from the maximum frequency (f_{max}) corresponding to the peak maximum in $M^{//}$ versus frequency curve provided the condition $2\pi f_{max} \times \tau = 1$ is satisfied.

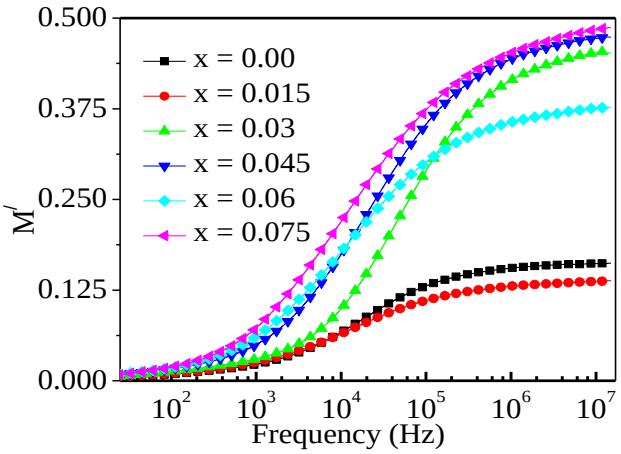

Fig. 5.13 Changes in $M^{/}$ of electric modulus $Ni_{0.5}Cu_{0.2}Cd_{0.3}Fe_{2-x}Al_xO_4$ as a function of frequency.

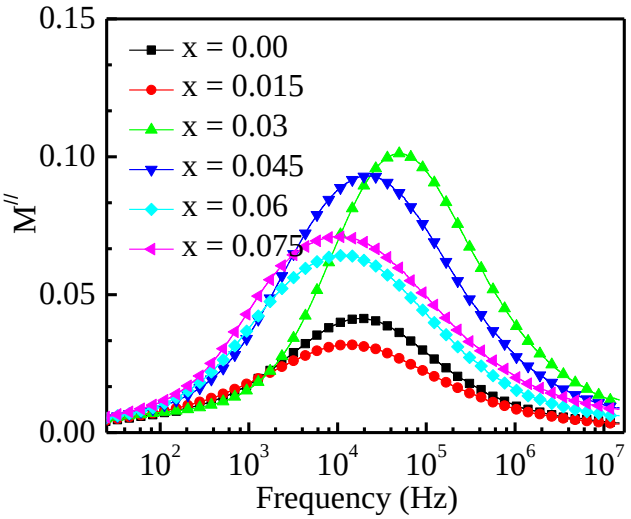

Fig. 5.14 Changes in M″ of electric modulus of $Ni_{0.5}Cu_{0.2}Cd_{0.3}Fe_{2-x}Al_xO_4$ as a function of frequency.

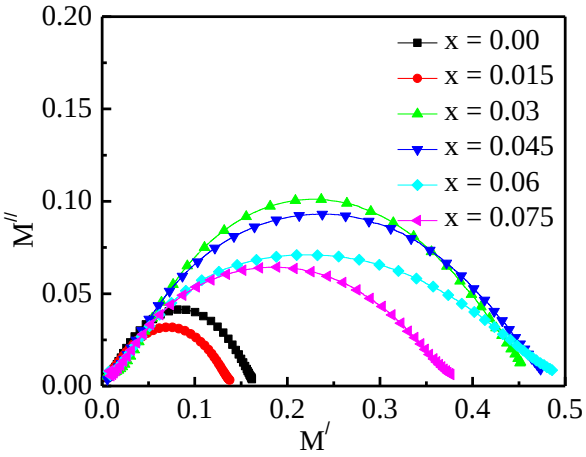

Fig. 5.15 M″ vs. M′ for $Ni_{0.5}Cu_{0.2}Cd_{0.3}Fe_{2-x}Al_xO_4$.

We can distinguish the relaxation of grains and grain boundaries by analyzing the electric modulus plot (M″ vs. M′ spectra) shown in Fig. 5.15. Typical depressed semicircular arcs with no intersecting of peaks have been seen for our synthesized samples, which suggest that the studied ceramic nanomaterials follow the non-Debye behaviour of relaxation time. It is also revealed that the complex modulus plot shows only single semicircles with no secondary circles that suggest the Al substituted Ni-Cu-Cd ferrites are single-phase which also validates the results of XRD data. The diameter of semicircles increases with the rise of Al content in the present series.

We can distinct the relaxation of grains and grain boundaries by analyzing the Cole-Cole plot of electric modulus (M″ vs. M′ spectrum) shown in Fig. 5.15. As shown in above figures, a typical semicircle patterns with no overlapping of peaks have been observed for our synthesized ferrite samples, which suggests the studied ferrite nanomaterials following the non-Debye behavior of relaxation time. It is also revealed that complex modulus plane plots contain only single semicircle with no secondary circles that suggests the Al substituted Ni-Cu-Cd ferrites are of the single phase which also validates the results of XRD data. The diameter of semicircles decreases with the increase of Al content in the samples.

References:

[1] S. Ikram, J. Jacob, M. I. Arshad, K. Mahmood, A. Ali, N. Sabir, N. Amin, S. Hussain, Ceram. Int. 45 (2019) 119-128.

[2] L. Kumar, P. Kumar, A. Narayan, M. Kar, Rietveld analysis of XRD patterns of different sizes of nanocrystalline cobalt ferrite. Int. Nano Lett. 3(1), (2013) 1–12.

[3] M. Arifuzzaman, M. Belal. Hossen "Effect of Cu substitution on structural and electric transport properties of Ni-Cd nanoferrites." *Results in Physics* 16 (2020): 102824.

[4] L. Kumar, M. Kar, "Effect of Ho3+ substitution on the cation distribution, crystal structure and magnetocrystalline anisotropy of nanocrystalline cobalt ferrite." *Journal of Experimental Nanoscience* 9.4 (2014): 362-374.

[5] M. I. Mendelson, Average grain size in polycrystalline ceramics, J. Am. Ceram. Soc. 52(8) (1969)443–446

[6] T. J. Shinde, A. B. Gadkari, P. N. Vasambekar, J. Mater. Sci. Mater. Electron. 21 (2) (2010) 120–124,

[7] M. K. Anupama, N. Srinatha, S. Matteppanavar, B. Angadia, B. Sahoo, B. Rudraswamy, Ceram. Int. 44 (5) (2018) 4946–4954,

[8]. A. K. M. Akhter Hossain, L. M. Rahman, J. Magn. Magn. Mat. 323(2011)1954–1962

[9] P. B. Belavi, G. N. Chavan, B. K. Bammannavar, L. R. Naik, R. K. Kotnala, J. Mat. Chem. Phys. 132(2012) 138-144.

[10] H. S. C. O'Neill, A. Navrotsky, Am. Miner. 68 (1983) 181–194.

[11] O. M. Hemeda, M. M. Barakat, J. Magn. Magn. Mater. 223 (2001) 127.

[12] D. R. Patil, B.K. Chougule, J. Mat. Chem. Phys. 117 (2009) 35.

[13] S. Dagar, A. Hooda, S. Khasa, M. Malik, J. Alloy. Compd. 806 (2019) 737–752

[14] J. C. Maxwell, Electricity and Magnetism, vol. 2, Oxford University Press, New York. (1973) 828.

[15] K. W. Wagner, Ann. Phys. 345 (1913) 817-855.

[16] C. G. Koops, Phys. Rev. 83 (1951) 121.

[17] L. T. Rabinkin, Z. I. Novikova, Acad. Nauk. USSR Minsk. (1960) 146

[18] N. Popandan, P. Balay, A. Narayansamy, J. Phys.: Condens. Matter. 14 (2002) 3221.

[19] I. H. Gul, Erum Pervaiz, Mater. Res. Bull. 47 (2012) 1353-1361.

[20] M. Hashim, Alimuddin, S. E. Shirsath, S. Kumar, R. Kumar, A. S. Roy, J. Shah, R. K. Kotnala, J. Alloy. Compd. 549 (2013) 348.

[21] A. Thakura, P. Mathura, M. Singh, J. Phys. Chem. Solids. 68 (2007) 378.

[22] M. L. S. Teo, L. B. Kong, Z. W. Li, G. Q. Lin, Y. B. Gan, J. Alloys Compd. 459 (2008) 567.

[23] D. Ravinder, K. Vijayakumar, Bull. Mater. Sci. 24 (5) (2001) 505.

[24] V. L. Mathe, K. K. Patanakar, M. B. Kothale, S. B. Kulakarni, P. B. Joshi, S. A. Patil, Pramana, J. Phys. 58 (2002) 1105.

[25] M. Hashim, Alimuddin, S. Kumar, S. Ali, B. H. Koo, H. Chung, R. Kumar, J. Alloys Compd. 511 (2012) 107.

[26] B. K. Kumar, G. P. Srivastava, P. Kishen, Proc. ICF-5(Bombay) (1988) 233.

[27] M. A. Ahmed, M. K. E. Nimar, A. Tawfik, A. M. E. Hasab, J. Magn. Magn. Mater. 98 (1991) 33.

[28] R. C. Kambale, P. A. Shaikh, C.H. Bhosale, K. Y. Rajpure, Y. D. Kolekar, Smart Mater. Struct. 18 (11) (2009) 115028.

[29] J. Liu, C. G. Duan, W. G. Yin, J. Chem. Phys. 119 (2003) 2812.

[30] C. León, M. L. Lucía, J. Santamaría, Phys Rev B 55 (1997) 882.

[31] R. Richert, H. Wagner, Solid State Ionics 105 (1998) 167.

[32] N. G. McCru, B. E. Read, G. Williams, Wiley, New York (1967).

[33] A. Marsha, S. N. Chowdhury, K. Prashad, R. N. P. Choudhary, Phys. B 406 (2011) 3279.

[34] I. Ali, M. U. Islam, M. N. Ashiq, I. Shakir, N. Karamat, M. Ishaque, M. N. Akhtar, H. M. Khan, M. Irfan, M. A. Khan, Ceram. Int. 41 (2015) 8748.

[35] B. V. R. Chowdari, R. Gopalkrishnnan, Solid State Ionics. 23 (1987) 225.

[36] M. F. Mahmood, M. Belal. Hossen, J. Mater. Sci: Mater Electron. 32 (2021) 14248–14273.

Chapter 6

Conclusions

The sol-gel auto combustion technique has been used for the synthesis of $Ni_{0.5}Cu_{0.2}Cd_{0.3}Fe_{2-x}Al_xO_4$ which are further annealed at 700^oC for characterization. By XRD analysis the single-phase cubic spinel structure of all investigated samples with displaying the narrow and high intensity peaks. The lattice constant gradually decreases linearly with increasing of Al content, thus obeying Vegard's law. These phenomena are explained in terms of their ionic radii i.e. Al^{3+} (0.535Å) is smaller than that of Fe^{3+} (0.645Å). The D_{311}, D_{FESEM} and $D_{W\text{-}H}$ have been computed from the Scherer's equation, FESEM observations and Williamson-Hall plot are found in the nano-scale range (16-21) nm, (99-46) nm and (22-16) nm respectively and all cases are decrease with increasing Al content. The grain size decreased with the increase in Al content. This is due to the liquid phase reduction by Al_2O_3 in the composition. The grain growth is due to the presence of capillary forces between the particles. From Rietveld refinement analysis χ^2 values lies in the range 1-2 known as goodness of fit is considered as best fitting which suggest good agreement for the XRD pattern.

All the compositions are found to be in ferromagnetic state at room temperature, which is revealed from the M versus H curve. With the increase in Al^{3+} substitution in the sample up to x = 0.030 M_s increased beyond that it decreases linearly. All observed curves are fitted well with the theoretical LAS curves and fitted parameter support for M_s.

The dielectric constant decreased with the increase of Al content. The value of dielectric constant is much higher at lower frequencies. It is because of the predominance species of space charge polarization as well as Fe^{2+} ions, oxygen vacancies, grain boundary defects, interfacial dislocation pile ups, voids etc. As iron ions exist in both 2+ and 3+ states, can

occupy A as well as B sites and substitution of Al for Fe occupy B site mainly. Thus the hopping of electrons between Fe^{3+} and Fe^{2+} at B sites decreases. As a result, the polarization and hence the dielectric constant decreases with the increase of Al content. The decreasing trend is natural due to the fact that any species contributing to polarizability is found lagging behind the applied field at higher frequencies. So, at very high frequencies, its value is so small that it becomes independent of frequency.

The value of loss factor decreased with the increase in frequency from 20 Hz to 15 MHz. The loss tangent decreased initially with increasing frequency followed by the appearance of a resonance peak in some of the compositions. The initial decrease in tanδ with an increase in frequency may be explained on the basis of Koops' phenomenological model. The peaking nature occurs when the jump frequency of the electrons between Fe^{2+} and Fe^{3+} is equal to the frequency of the applied field.

The complex impedance plots reveal two semicircles described by the intrinsic grain (bulk) and grain boundary (interface) effects. In case of $Ni_{0.5}Cu_{0.2}Cd_{0.3}Fe_{2-x}Al_xO_4$, complex impedance spectra show clearly the contribution of both grain and grain boundary effects in the electrical properties. Both the grain (30.03 to 100 MΩ) and grain boundary (500 to 980 MΩ) resistance increase with increasing Al content. This high value of grain resistance (3 times more than the pure Ni-Cu-Cd) which is contributed to the high frequency region and thus reduces eddy current losses and this property is technologically important for radio frequency applications.

Investigations on impedance spectra and electrical modulus analysis of $Ni_{0.5}Cu_{0.2}Cd_{0.3}Fe_{2-x}Al_xO_4$ show single arc with double semicircle (or its tendency) obtained at room temperature corresponding every composition in both the complex impedance and electric modulus plots suggests the single-phase character of the materials. It is observed that two separate

conduction processes in impedance and modulus spectra attributed to grain and grain boundary effects.

The observed ac conductivity increases linearly with frequency in two different regions. The frequency dependent σ_{ac} can be explained on the basis of Maxwell-Wagner two layers model. At lower frequency, the grain boundaries are more active, hence the hopping frequency of electrons between Fe^{3+} and Fe^{2+} ions is less. At higher frequencies, the conductive grains become more active by promoting the hopping of electrons between Fe^{3+} and Fe^{2+} ions therefore increasing the hopping frequency. Simple synthesis technique, better homogeneity, well crystallized, enhance magnetic, increased resistivity, low dielectric loss tangent and cost-effective Ni-Cu-Cd and Ni-Cu-Cd-Al ferrite nanoparticles are achievements of the present research.

Publication

Dynamic Electric, Modulus and Impedance Study of $Ni_{0.5}Cu_{0.2}Cd_{0.3}Fe_{2-z}Al_zO_4$ Nanoparticles with Magnetization and Rietveld Analysis

M. Abdul Mannan, M. Belal Hossen, ***J Mater Sci: Mater Electron (2021) 32:24524-24539***

J Mater Sci: Mater Electron (2021) 32:24524–24539

Dynamic electric, modulus and impedance study of $Ni_{0.5}Cu_{0.2}Cd_{0.3}Fe_{2-z}Al_zO_4$ nanoparticles with magnetization and Rietveld analysis

M. Abdul Mannan[1] and M. Belal Hossen[1,*]

[1]Department of Physics, Chittagong University of Engineering and Technology, Chattogram 4349, Bangladesh

Received: 5 May 2021
Accepted: 28 August 2021
Published online: 12 September 2021

ABSTRACT

The ferrite nanoparticles of $Ni_{0.5}Cu_{0.2}Cd_{0.3}Fe_{2-z}Al_zO_4$ ($0.00 \le z \le 0.075$ with step 0.015) were synthesized with popular sol–gel method and their physical, magnetic and electrical transport characteristics have been analysed. The X-ray diffraction pattern confirms the precise single-phase spinel structure for every composition as justified by the Rietveld refinement analysis. The Field emission scanning electron microscopy (FESEM) technique reveals surface morphology of the synthesized sample at nanoscale. The FESEM image shows the nanosized (99–46 nm) ferrites with narrow size distribution occupying spherical shapes. To illustrate magnetic characteristics, vibrating sample magnetometer and the law of approach to saturation has been used to analyse (M–H) data in saturation region in order to extract the hysteresis parameters. The intrinsic saturation magnetization (M_s) as well as magnetic moment are found to increase with Al^{3+} substitution up to $z = 0.03$. The dielectric properties (real and imaginary part, loss tangent ($\tan\delta$) and ac conductivity (σ_{ac}) were measured with frequency at room temperature. Both $\tan\delta$ and σ_{ac} were decreased with Al content showing potentiality for high-frequency applications. Complex impedance studies disclose the increase of grain resistance and grain boundary resistance with increasing Al content. Modulus spectroscopy study shows the dynamics of conduction mechanism in the synthesized ferrite nanoparticles.

1 Introduction

Ferrites are defined as non-conductive ferrimagnetic ceramic compounds. It is generally originated from Fe oxides such as Fe_3O_4 or Fe_2O_3 and other metals oxides. The study of magnetism is the main emphasis in the new era of the nanoscale world. The nanoworld needs to reduce the large magnetic circuits to integrate magnetic performance with other characteristics. The main opportunities for ferrite nanoparticles are size and physicochemical behaviours. The synthesis of nanoparticles demands high importance due to their universal applications in the fields of material science, biomedical, biotechnology,

Address correspondence to E-mail: mbhossen@cuet.ac.bd

Springer

https://doi.org/10.1007/s10854-021-06930-2

engineering, etc. [1–4]. Popular magnetic spinel ceramics, nickel-containing ferrites have been successfully manufactured and their characterization was widely done because of their enormous multifunctional applications due to their comparatively higher inductive property at higher frequency regions, reasonably low demagnetizing as well as dielectric losses and obviously lower electrical conductivity [5]. Considering research in these fields, a recognized truth could be concluded that when a magnetic cation is substituted by a non-magnetic cation (Here $Al^{\beta+}$), it diluted their exchange interaction in addition to the influence of structural, magnetic and electrical characters of every composition. For instance, the light substitution of Fe^{3+} by Al^{3+} in NiCuCd ferrites increases both saturation magnetization and electrical resistivity with lower dielectric losses and thereby remarkably increased both electrical and magnetic properties of the ceramics for some optimum compositions [4, 7]. Many researchers studied the magnetic characteristics of NiCuZn-based nanocrystals but for the NiCuCd containing properties, which become alternate candidates, are seldom noted [5]. The behaviour of ferrite materials can be changed by the chemical composition, substituent, synthesis technique, temperature etc. and substitution of non-magnetic Al show rare characteristics for its (Al^{3+}) inert gas configuration showed by many researchers [6–8]. According to them, the substitution of a small amount of Al increases both resistivity and magnetization and decreases the dielectric-anisotropy constant. The sol–gel technique is expected to fabricate magnetic nanoparticles. The main attraction of the formation of homogeneous magnetic nanoparticles with their physical properties and controllable size which encouraged the synthesis of excellent magnetic nanoparticles of different compositions with improved quality in terms of phase, nanostructure, magnetization and resistivity. The outcome of this research will be essential for engineers and scientists to manufacture various devices for high-frequency applications.

2 Experimental technique

The auto-combustion synthesis process was used to synthesize Al replaced Ni–Cu–Cd nanoparticles of ferrite and this method are considered a prosperous technique for the preparation of nanocrystalline ferrite particles. 'AR' ranking of $Ni(NO_3)_2{\cdot}6H_2O$, $Cd(NO_3)_2{\cdot}4H_2O$, $Cu(NO_3)_2{\cdot}3H_2O$, $Fe(NO_3)_3{\cdot}9H_2O$ and $Al(NO_3)_3{\cdot}9H_2O$ as initial ingredients to prepare the samples. We mixed stoichiometric compositions of the above raw materials thoroughly to make a solution and added some ethanol to enhance the homogeneity of the mixtures. Ethyl alcohol is essential for the uniform structure and separation of metal ions. At the time of water evaporation, it abolishes the dew of metal nitrates for the existence of electropositive metal ions and electronegative oxygen ions; so, the pioneer elements get a homogeneous structure. For controlling pH ~ 7, AR grade liquor ammonia (25%) was added which also improves the solubility of metal ions. The homogeneous gel formed with continuous stimulation by a magnetic stirrer. For better-dried gel, the subsequent solution was then heated uninterruptedly at a water bath at 70 °C for 24 h. It was then allowed to heat at 200 °C to get fluffy loose powder. These powders were annealed for 5 h at 700 °C to remove any unwanted ingredient present in the composition and structural homogeneity. The temperature ramps were 10 °C/min for heating and 5 °C/min for cooling. The annealed powder was then further ground for another 3 h. At a pressure of 5000 psi for about 2 min, the specimens were pressed into a round disc (pellets) for electric measurements. For making parallel plate-shaped capacitors, a uniaxial press was used and two probe connections were ensured by applying the silver paste on the opposite faces.

According to Bragg's law, following Eq. (1) is given,

$$2d_{hkl}\sin\theta_{hkl} = n\lambda \tag{1}$$

where d_{hkl} is the crystal layer spacing, n is the integer, λ is the wavelength and θ_{hkl} is the incident angle which is the condition for constructive interference of X-ray scattering [9, 10]. Otherwise, destructive interference will occur. When infinite Bragg's scattering occurs in the crystal at discrete values of 2θ fulfils Bragg's condition. When the widened Bragg's peak ends at $2\theta_1$ and begins at $2\theta_2$ the Full width at half maximum (FWHM) is given by Eq (2),

$$\beta = \frac{1}{2}(2\theta_1 - 2\theta_2) = (\theta_1 - \theta_2) \tag{2}$$

Scherrer's formula is shown in Eq. (3),

$$D_{xrd} = \frac{0.9\lambda}{\beta_{311}\cos\theta_{311}} \quad (3)$$

To evaluate the crystallite size (D_{XRD}) of crystal from the calculated width of (311) peak for every composition of XRD patterns [11], the above equation was used.

Impedance (real and imaginary part), ac conductivity and dielectric constant measurements were carried out by impedance analyzer (Wayne Kerr, 6505B). The real part of dielectric constant (ε') can be obtained by Eq. (4),

$$\varepsilon' = \frac{Cd}{\varepsilon_0 A} \quad (4)$$

where A is area of cross-section, ε_0 is permittivity for vacuum, C is capacitance of circular disc for parallel geometry and d is thickness of the circular disc. All are in S. I. units [12–14]. The corresponding imaginary part (ε'') was measured from Eq. (5);

$$\varepsilon'' = \varepsilon' \tan\delta \quad (5)$$

where tanδ is dielectric loss tangent.

According to the Eq. (6),

$$\sigma_{ac} = d/(A * R_{ac}) \quad (6)$$

where R_{ac} is the ac resistance, the ac conductivity was measured.

3 Results and discussion

Figure 1a shows the XRD pattern of all compositions in $Ni_{0.5}Cu_{0.2}Cd_{0.3}Fe_{2-z}Al_zO_4$ annealed at 700 °C. To study nanostructure, the XRD technique is used, which ensures the prime and deterministic condition of any research. There appear various characteristic diffraction peaks of each composition due to the fundamental reflections originating from the planes of (111), (220), (311), (222), (400), (422), (511) and (440) with no secondary peaks. The most intense peaks appear due to reflection from the plane (311) in each composition. The height of peaks become broader (Fig. 1b) with increasing Al content in the composition indicating smaller crystallite size, which makes Al an important element to get smaller crystallite as well as to enhance the crystalline properties. The observed sharp peaks comply with the reference value and confirm the structure of spinel formation for every sample and indicate a precise crystalline homogeneous structure [15]. From Fig. 1, the appearance of broader peaks represents the nanocrystalline nature of the synthesized powders. The background data shows the crystallite size (D_{XRD}) of all compositions obtained from XRD analysis lies in the nanoscale range. The D_{XRD} and D_{FESEM} (discuss later) variation with Al content in the samples tabulated in Table 1, which show a decreasing trend of D.

The XRD data of all samples are analysed by the Rietveld refinement procedure. The outcomes are demonstrated in Fig. 2. Each of every Rietveld fitted patterns for all samples are sequentially represented in Fig. 2a–b. This structural analysis of all compositions ensures their characteristics and obtained parameters are also indicated in the graphical representation. As less than two values of χ^2 known as the goodness of fit are considered as best fitting, these findings suggest good agreement for the XRD pattern [16]. Besides, cubic phase with space group Fd-3m has been confirmed through the Rietveld refinement. Furthermore, the doping of Al on ferrites reveals some changes in lattice parameters and listed in provided Table with other parameters such as volume and goodness of fit. From Table 1, it is evident that the lattice parameter has been reduced slightly as the amount of Al substitution is increased. As a result volumes of the unit cell of spinel ferrite structure are decaying by the reduction of Fe^{3+} ions. The reason behind this reduction may be a compressive strain of composition. The variation of microstrain can be seen from the data in Table 1. The ferromagnetic characteristics, as well as the magnetic properties of these nanoparticles, can be affected by this parameter [17].

The preferences of cations for tetrahedral (A) sites and octahedral (B) sites are determined from the outputs of Rietveld refinement [18] and listed in Table 2.

Figure 3 shows the variation in lattice constant (a_0) of $Ni_{0.5}Cu_{0.2}Cd_{0.3}Fe_{2-z}Al_zO_4$ as a function of Al substitution in the compositions. It is observed that the a_0 reduces with rising Al content, which can be interpreted with the difference in ionic radius between Fe^{3+} (*0.67 Å*) and Al^{3+} (*0.55 Å*) [19].

Figure 4a–f are used to study surface morphology of the samples with Al content $z = 0.00$ to $z = 0.075$, respectively. The surface morphology gives visibly the type of grain growth and the average size of a grain of each composition and can be determined from FESEM analysis and its impacts on physical, electrical, and magnetic behaviours of the

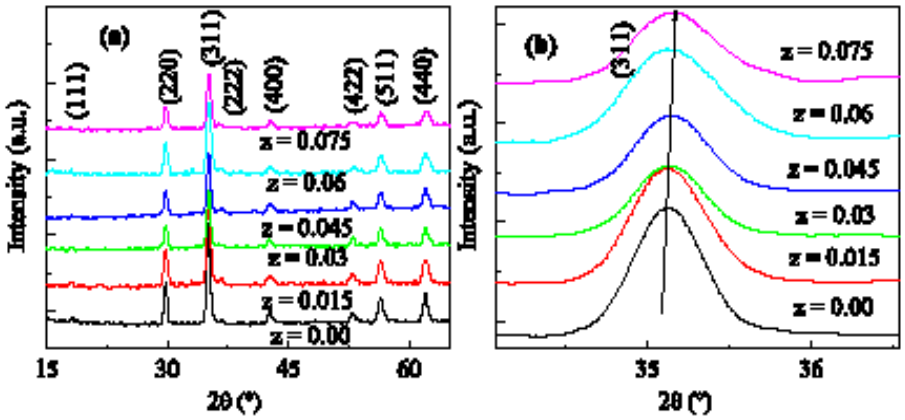

Fig. 1 a XRD pattern and b extended (311) peak of $Ni_{0.5}Cu_{0.2}Cd_{0.3}Fe_{2-z}Al_zO_4$ annealed at 700 °C (JCPDS card number 90–09922)

Table 1 Change in lattice constant (a_o) and crystallite size of $Ni_{0.5}Cu_{0.2}Cd_{0.3}Fe_{2-z}Al_zO_4$

Al content	Lattice constant (Å)	Lattice constant (Å) by Rietveld method	χ^2	D_{XRD} (nm)	D_{FESEM} (nm)	D_{W-H} (nm)	Micro strain
0.00	8.483	8.4751	1.43	21	99	22	0.00196
0.015	8.476	8.4761	1.40	20	77	21	0.00536
0.030	8.466	8.4726	1.22	20	75	20	0.0019
0.045	8.46	8.4723	1.31	20	69	29	0.00871
0.060	8.449	8.4720	1.45	18	61	18	0.00896
0.075	8.443	8.4676	1.23	16	46	16	0.14065

synthesized nanoparticles [20, 21]. The grain size and grain boundary are two important parameters in nanotechnology that cause exotic properties, owing to the limited size and surface impacts. The FESEM nanographs of $Ni_{0.5}Cu_{0.2}Cd_{0.3}Fe_{2-z}Al_zO_4$ have been shown in Fig. 4. According to the observed morphology, the fine particles in the compositions with narrow size distribution are without any impurity under the annealing process. The grains of various sizes and shapes are detached with grain boundaries with some agglomerations are appeared in Fig. 4. Accordingly, the nanosized grains are spherical and distributed homogeneously. The crystallite size measured using FESEM nanographs by the imaging technique to be a similar trend and matched well with the XRD results for the studied compositions. The estimated average grain size [22] lies in the range of (99–46) nm for annealing at 700 °C.

The magnetic hysteresis behaviour of the synthesized nanoparticles has been observed with VSM with an applied field of 1.5 T (in μ_oH) at room temperature to reach the value of saturation. The observed hysteresis loops have been presented in Fig. 5. The change in magnetization with the applied magnetic field (M–H) for different compositions at room temperature can be observed in Fig. 5. It is noticed that the magnetization of all the compositions initially rises sharply along with a rising external field (H) up to 0.25 T.

(in μ_oH) and then it attains saturation (M_s). The values of M_s with theoretical and experiment magnetic moments for samples are given in Table 3. It is also clear from Fig. 5 that M_s increased up to $z = 0.03$ beyond which it reduces with Al content rises. The same behaviour of soft ferrites with Al substitution can also be observed [23]. This type of variation in M_s with Al^{3+} content can be interpreted based on the distribution of cation with exchange interaction over A- and B- sites which influence the magnetic behaviours of ferrite nanoparticles. By applying Hund's rule with magnetic moment (μ_B) and Al^{3+} ($0\mu_B$),

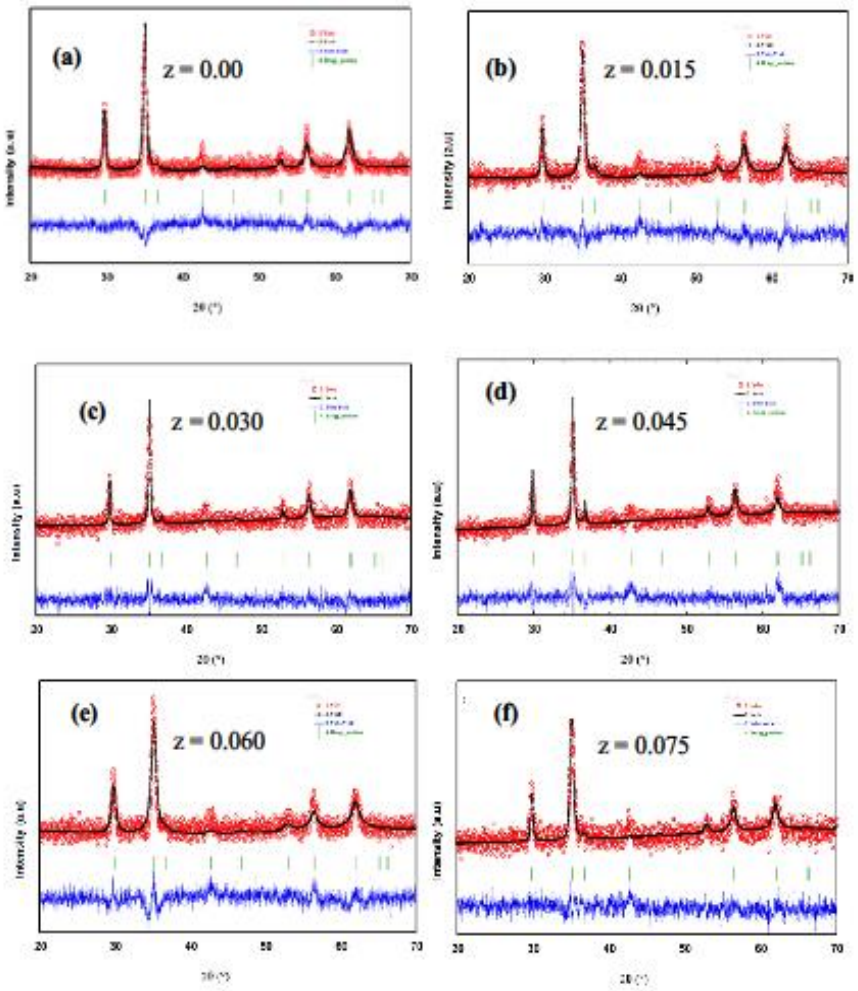

Fig. 2 Rietveld refinement of $Ni_{0.5}Cu_{0.2}Cd_{0.3}Fe_{2-z}Al_zO_4$ a without Al content, b with Al content 0.015, c with Al content 0.030, d with Al content 0.045, e with Al content 0.060 and f with Al content 0.075

Table 2 Cation distributions of $Ni_{0.5}Cu_{0.2}Cd_{0.3}Fe_{2-z}Al_zO_4$

Al content	Composition	Cation distribution
0.00	$Ni_{0.5}Cu_{0.2}Cd_{0.3}Fe_2O_4$	$(Ni_{0.29}Cu_{0.13}Cd_{0.13}Fe_{0.438})_A[Ni_{0.21}Cu_{0.07}Cd_{0.17}Fe_{1.562}]_BO_4$
0.015	$Ni_{0.5}Cu_{0.2}Cd_{0.3}Fe_{1.985}Al_{0.015}O_4$	$(Ni_{0.27}Cu_{0.13}Cd_{0.13}Al_{0.007}Fe_{0.458})_A[Ni_{0.23}Cu_{0.07}Cd_{0.16}Al_{0.008}Fe_{1.527}]_BO_4$
0.030	$Ni_{0.5}Cu_{0.2}Cd_{0.3}Fe_{1.97}Al_{0.03}O_4$	$(Ni_{0.29}Cu_{0.13}Cd_{0.14}Al_{0.001}Fe_{0.438})_A[Ni_{0.21}Cu_{0.07}Cd_{0.16}Al_{0.029}Fe_{1.532}]_BO_4$
0.045	$Ni_{0.5}Cu_{0.2}Cd_{0.3}Fe_{1.955}Al_{0.045}O_4$	$(Ni_{0.24}Cu_{0.13}Cd_{0.14}Al_{0.005}Fe_{0.485})_A[Ni_{0.26}Cu_{0.07}Cd_{0.16}Al_{0.040}Fe_{1.470}]_BO_4$
0.060	$Ni_{0.5}Cu_{0.2}Cd_{0.3}Fe_{1.94}Al_{0.06}O_4$	$(Ni_{0.29}Cu_{0.14}Cd_{0.13}Al_{0.006}Fe_{0.437})_A[Ni_{0.21}Cu_{0.06}Cd_{0.17}Al_{0.054}Fe_{1.503}]_BO_4$
0.075	$Ni_{0.5}Cu_{0.2}Cd_{0.3}Fe_{1.925}Al_{0.075}O_4$	$(Ni_{0.29}Cu_{0.13}Cd_{0.13}Al_{0.006}Fe_{0.439})_A[Ni_{0.21}Cu_{0.07}Cd_{0.17}Al_{0.069}Fe_{1.501}]_BO_4$

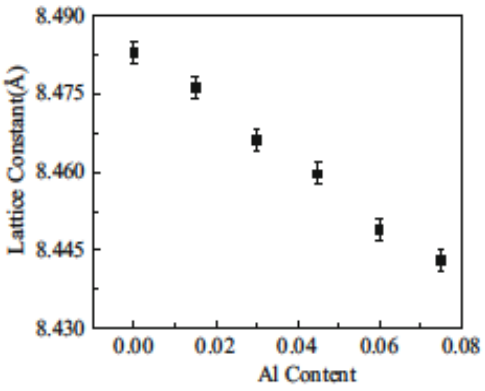

Fig. 3 Variation in lattice constant of $Ni_{0.5}Cu_{0.2}Cd_{0.3}Fe_{2-z}Al_zO_4$

$Ni^{2+}(2\mu_B)$, $Cu^{2+}(1\mu_B)$, $Cd^{2+}(0\mu_B)$ and $Fe^{3+}(5\mu_B)$, the cations can be distributed on the tetrahedral (A) site and octahedral (B) site by considering Table 2 where all cations are placed in their respective positions from Rietveld analysis [24]. The total μ_B decreases at the B- site with increasing Al^{3+} content instead of Fe^{3+} in the B-site. The μ_B of Al^{3+} and Fe^{3+} reference value and the change in magnetization at B-site is expected because B-site occupies non-magnetic trivalent Al^{3+} content and therefore the total magnetization ($M_S = M_B - M_A$) decreases ultimately by diminishing the B–A interaction in these ferrite nanoparticles. As reported in [25] and established in many research works that any level of Al concentration, Al^{3+} prefers to accumulate them in B-site. So, the total magnetic moment, as well as M_s, are found to be decreased with Al^{3+} substitution beyond the value of $z = 0.03$.

The comparison between theoretical and experimental numbers (n_{th} and $n_{ex}t$) of Bohr magnetron (μ_B) with Al^{3+} substitution has been shown in Table 3. Assuming anti-parallel interaction, theoretical μ_B is estimated by Eq. (7),

$$n_{th} = (M_1B - M_1A)\mu_B B \tag{7}$$

for different values of Al^{3+} content using ionic magnetic moment and cation distribution of Cu^{2+}, Cd^{2+}, Al^{3+} and Fe^{3+}. The formula of Eq. (8),

$$n_{exp(\mu_B)} = \frac{M_w \times M_s}{5585} \tag{8}$$

was used to calculate the experimental number μ_B. The deviation between n_{th} and $n_{ex}t$ may be due to the reason that the theoretical number of μ_B was calculated at 0 K, but the experimental values of μ_B were determined at room temperature (at 300 K). From Table 3, the theoretical magnetron number reduces but the experimental values rise to $z = 0.03$ and then reduce with the rise in Al^{3+} substitution. From Table 3, it is found that substitution of magnetic Fe^{3+} ion by non-magnetic Al^{3+} ion at B-site is the main cause of linear reduction of saturation magnetization. Al^{3+} does do not involve in the swap interaction to the nearest neighbour ions as it is a non-magnetic ion, the magnetization reduces at B-site as well as the net saturation magnetization reduce in A–B interaction. We can interpret the enhancement of M_s using the relation $M_s = M_B \cos\gamma - M_A$; where the M_s firstly increases due to the canting angle decreased. When the canting angle γ appears lower, i.e. increases $\cos\gamma$ and magnetization increases at the saturation point up to $z = 0.03$. It is due to Al^{3+} is smaller in size than Fe^{3+} that is also observed from XRD analysis. Hence, the substitution of smaller ion increases A–B exchange interaction by decreasing the distance between the magnetic cations. As a result, the canting angle decreased [26]. Further increase of Al content, the M_s decreases due to the non-magnetic Al^{3+} increases beyond $z \geq 0.03$ reduces magnetic moment more in the B-site compared to the increased exchange interaction. The table shows the percentage (%) of magnetization (M_s) and using this saturation $z = 0.03$ is 66.36 which is 1.3 times greater than the mother sample, ($M_s = 52.2$). $\mu_{B exp}$ shows a similar trend of M_s values.

Figure 6a–f shows the representative curves of M_s fitted to Law of approach to saturation (LAS) for all compositions [27] of present investigated samples from $z = 0.00$ to $z = 0.075$ to determine the M_s. The expression for the LAS is given by Eq. (9),

$$M = M_s\{1 - (8K_1^2/105M_s^2H^2)\} \tag{9}$$

The values of B and M_s are obtained from the M–H fitted curve and K_1 is called the cubic anisotropic constant which is calculated by Eq. (10),

$$K_1 = M_s\sqrt{(105B/8)} \tag{10}$$

where B is anisotropy constant

All observed curves are fitted well with the theoretical LAS curves and fitted parameter M_s is obtained from this method and listed in Table 3.

The reflections in ε' and ε'' of the dielectric constant of $Ni_{0.5}Cu_{0.2}Cd_{0.3}Fe_{2-z}Al_zO_4$ ferrite nanoparticles with a frequency range of 20–15 MHz have been shown in

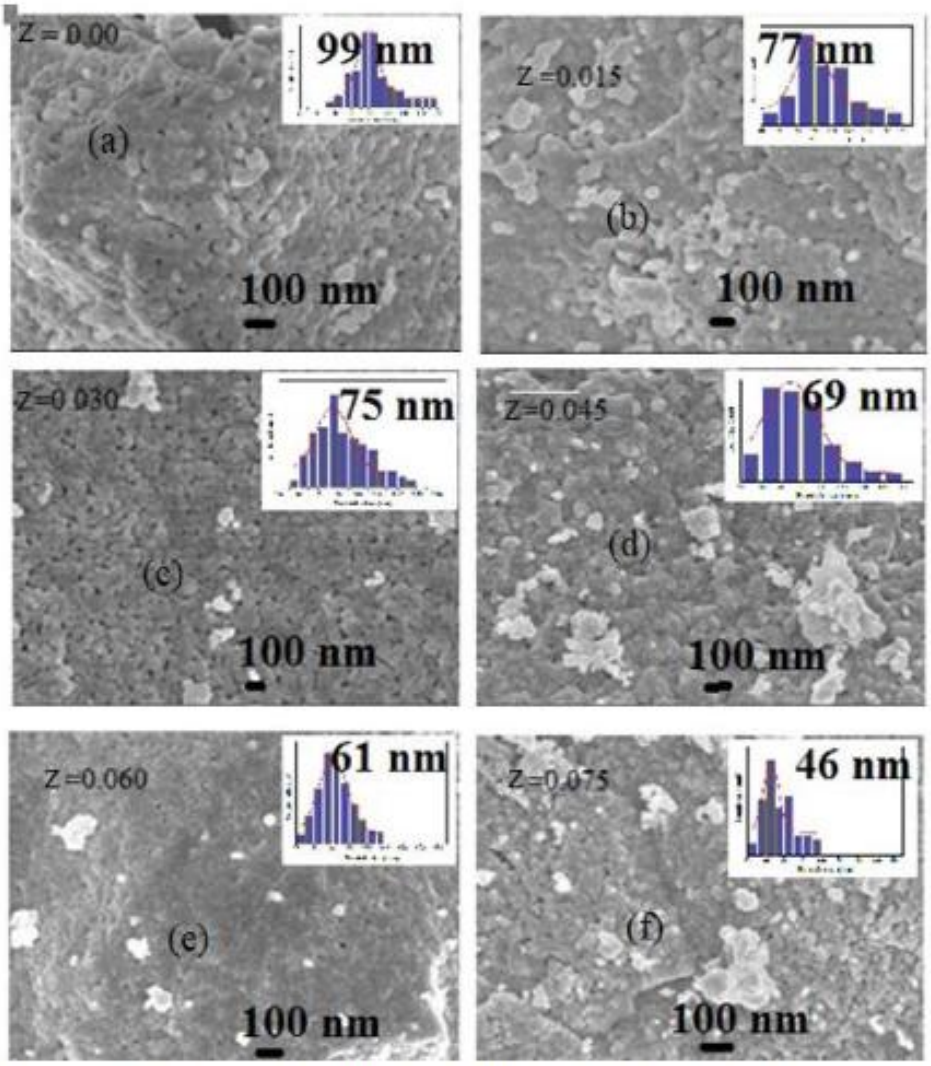

Fig. 4 FESEM nanographs of $Ni_{0.5}Cu_{0.2}Cd_{0.3}Fe_{2-x}Al_xO_4$ annealed at 700 °C **a** without Al content, **b** with Al content 0.015, **c** with Al content 0.030, **d** with Al content 0.045, **e** with Al content 0.060 and **f** with Al content 0.075

Figure 7a, b. At lower frequencies (in kHz region/of order $\sim 10^3$), the values of ε' and ε'' are much higher and the values are so small at high frequencies and become almost distinct from the frequency [28]. Therefore, these materials possess high dielectric values which are due to space charge polarization. The creation of grains with semiconducting nature occurs at the time of synthesis of ferrites nanocrystals, these adjacent grains are separated by thin layers with insulating character and therefore they act as dissimilar dielectric materials. Again, the creation of Fe^{2+} from Fe^{3+} also takes place in these ferrites. It is clear from the observed behaviour of ε' and ε'' that energy dissipation term decreased rapidly as well as with Al content. Polarization of space charge is caused due to the existence of semiconducting phases as grains in the non-conducting medium as grain boundaries of a dielectric and creates a confined

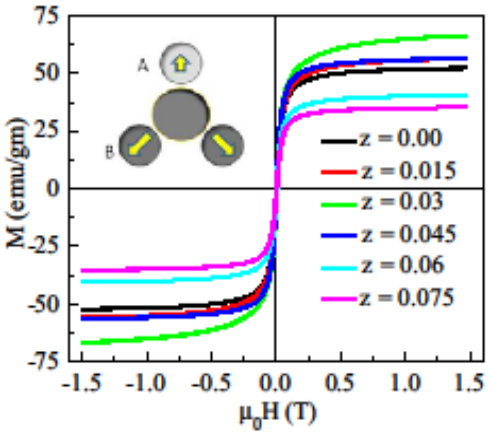

Fig. 5 Variation of M with H for various of $Ni_{0.5}Cu_{0.2}Cd_{0.3}Fe_{2-z}Al_zO_4$ at room temperature

accumulation of charges under the impact of an ac electrical field [29]. Space charge carriers assemble in a dielectric substance brings a fixed time to follow up their axes which is parallel to an ac electric field. With increasing frequency, a point is attained where the carriers of space charge cannot maintain with the field, as the frequency of the field reversal raises and the repetition of their direction goes backwards than the field which causes reduction of dielectric values [29]. The behaviour of the dielectric constant can also be described according to the two-layer model of Maxwell and Wagner. Accordingly [30, 31], the interfacial polarization is due to the dissimilar dielectric structure of the material. This structure is created by large semiconducting grains which are separated by thin intermediate insulating grain boundaries. According to Rankin and Novikova [32], polarization in ferrites is similar to the conduction process. Electronic exchanges between $Fe^{2+} \leftrightarrow Fe^{3+}$ consequences are confined of electrons in the direction of the applied field, which establishes polarization. As frequency rises, the polarization reduces and then attains a constant value, because it exceeds the specific frequency of the outward field, the electronic interchange between $Fe^{2+} \leftrightarrow Fe^{3+}$ cannot go along with the alternating field. This is due to the majority of Fe^{2+} ions, grain boundary defects, oxygen vacancies, voids, interfacial displacement piles etc. [8, 33, 34]. Since the frequency rises, the decreasing tendency of the dielectric constant is normal due to which the species donating to the polarizability are found far behind the applied field at upper frequencies [33].

Figure 8 indicates the change in tanδ with frequency. The early reduction of *tanδ* with increasing frequency could be explained with hopping frequency. Accordingly, when the applied field frequency approaches close to the frequency of the hopping charge carrier, the highest value of tanδ at a particular frequency is attained. In the assessed frequency (20–15 MHz), all samples show Debye relaxation. With the Reslescu model, we can explain the features of loss tangent with frequency [34]. The combination of the frequency of the external field and the frequency of the hopping charge of the exchange ions creates a resonance peak or Debye relaxation. A small shift in maxima can be observed at higher frequencies. The peak height also depends on Al-doping. The nature of this peak can be observed if the applied field frequency is almost equal to the jumping frequency of the electron between Fe^{2+} and Fe^{3+}. Maxima shift towards lower frequency regions with Al-doping reveals that the possibility of jumping raises. Resistivity increased for the decrease of the Fe^{3+}/Fe^{2+} ion pairs in the conduction process. Hence the zenith of the peak increases with Al-doping.

The variation of electrical conductivity as a function of frequency (σ_{ac}) obtained at room temperature has been shown in Fig. 9. The σ_{ac} increases with the

Table 3 Magnetic properties like M_s, M_n from LAS and experimental magnetic moment

Al content (z)	Saturation magnetization [M_s (emu/gm)]	M_n (emu/gm) from LAS	Experimental magnetic moment ($\mu_{B,exp}$)
0.00	52.2	52.35	2.3503
0.015	55.26	56.82	2.5287
0.030	66.36	67.5	2.9775
0.045	56.29	57.03	2.5213
0.060	40.46	41.05	1.8091
0.075	35.21	35.35	1.5691

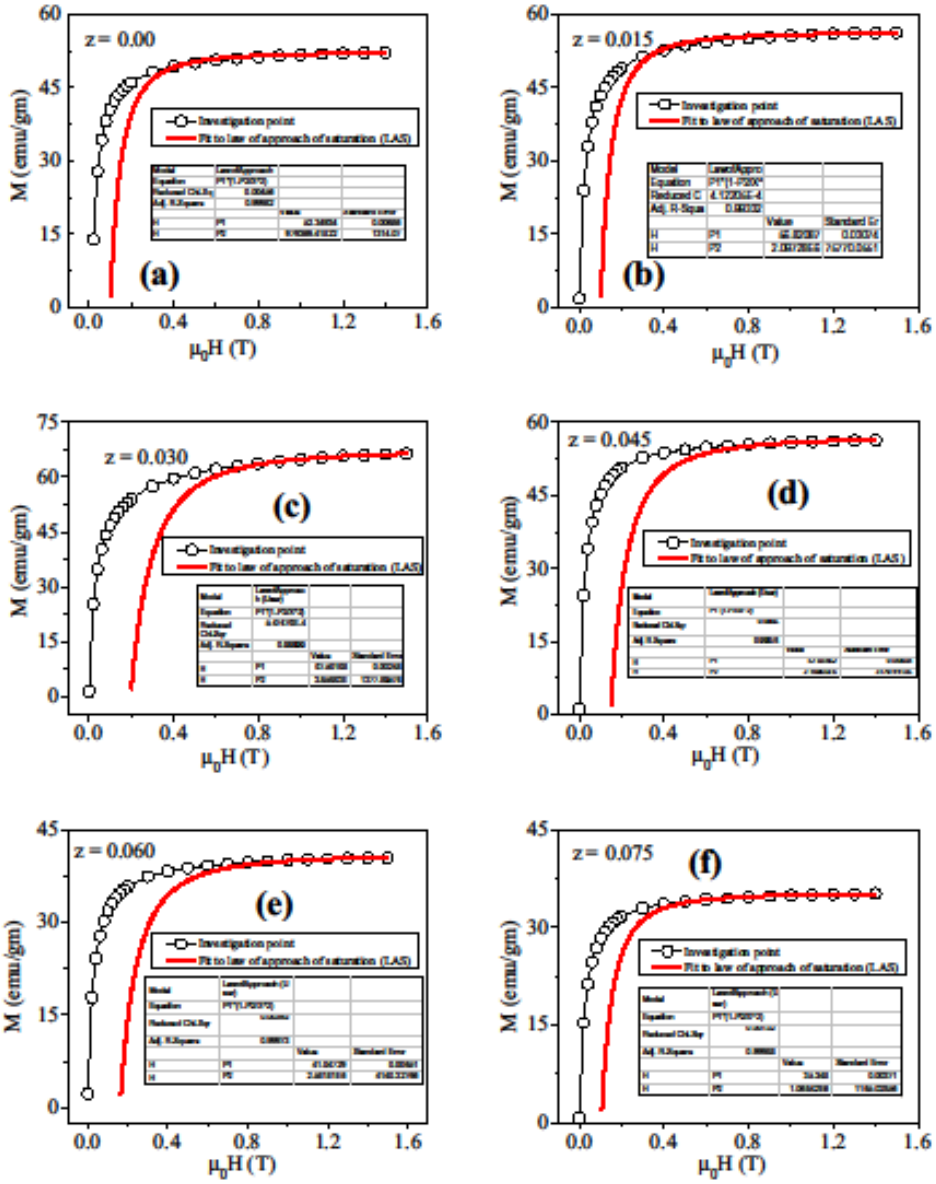

Fig. 6 Fitted curves of LAS **a** without Al content, **b** with Al content 0.015, **c** with Al content 0.030, **d** with Al content 0.045, **e** with Al content 0.060 and **f** with Al content 0.075

increase of frequency for all samples. This is a general behaviour of ferrites. Due to the hopping of charge carrier between same elemental ions, electrical conductivity in ferrites mainly depends upon multiple valence states, crystallographic equivalent random distribution at nearest neighbour lattice sites. The distance of hopping between two metals ions on A sites (0.357 nm) is greater than the distance of

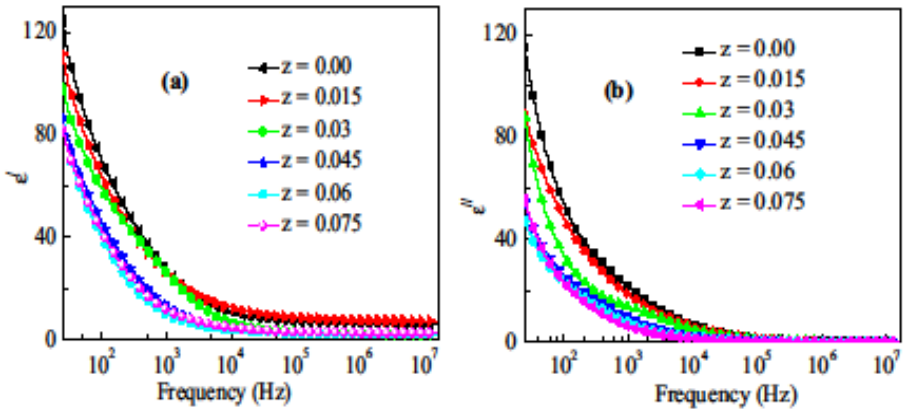

Fig. 7 Variation of a ε' and b ε'' with frequency for $Ni_{0.5}Cu_{0.2}Cd_{0.3}Fe_{2-x}Al_xO_4$

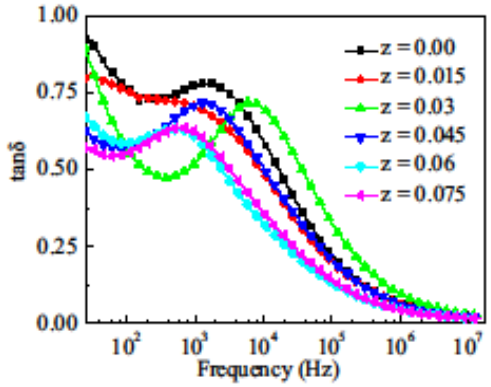

Fig. 8 tanδ of $Ni_{0.5}Cu_{0.2}Cd_{0.3}Fe_{2-x}Al_xO_4$ with frequency

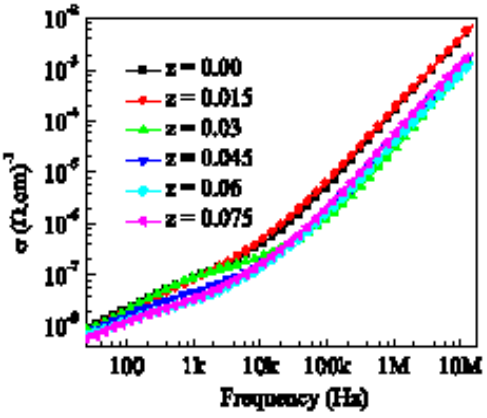

Fig. 9 Variation in conductivity of $Ni_{0.5}Cu_{0.2}Cd_{0.3}Fe_{2-x}Al_xO_4$ with frequency

hopping between two metal ions on B sites (0.292 nm). So, hopping on B sites has more potential than hopping between A- and B sites. Fe^{3+} at A sites and Fe^{2+} at B sites, so A–A sites hopping does not occur [35]. The charges drift under the control of the applied field, donating to the electrical reaction of the scheme. In the case of hopping conduction which rises with frequency and in the case of band conduction, the conductivity reduces with frequency [36]. The relation between conductivity and frequency is given by Eq. (11),

$$\sigma_{tot} = \sigma_0(T) + \sigma(\omega, T) \tag{11}$$

Here, the initial term (σ_0 (T)) is for band conduction which is the dc conductivity and it does not depend on frequency. The other term ($\sigma(\omega,T)$) is for the hopping method at the B-site which is the σ_{ac} and it is a function of frequency. The initial term is mainly significant at high temperature and low frequencies, whereas the second term is mainly significant at low temperature and high frequencies. For the 2nd term, it is written as experimental formula [37] as the part of the conductivity as given by Eq. (12);

$$\sigma_{ac} = S\omega^n \tag{12}$$

where S is a constant angular frequency, ω (= $2\pi f$) and 'n' is the angular frequency and an exponent respectively. In the region where the conductivity rises firmly with frequency, the electrical transportation is controlled by hopping among infinite groups. The upper-frequency cut-off region begins with an electrical performance in the sample. The

electron-hopping model is applicable for explaining the electrical conduction process. The conduction process is owing to the hopping of charge carrier between two nearby B sites, $Ni^{2+} \Leftrightarrow Ni^{3+}$ or Fe^{2+}-Fe^{3+} in the spinel lattice of the samples. If the frequency increases, the rate of hopping will also increase. As a result, increased conductivity is found in samples. In the case of the upper-frequency region, the σ_{ac} increased slowly with frequency for grain regions as the hopping frequency does not support the variations of the external field outside a certain limit of frequency [38]. It is observed that the σ_{ac} reduces with increasing Al content. As Al is a noble gas structure, it always forms trivalent ion for bonded with others and reduces the ferrous ion form i.e. hopping between $Fe^{2+} \Leftrightarrow Fe^{3+}$ decreased remarkably.

An idealized circuit model including distinct electrical components is applicable for impedance analysis in this system. The study is generally performed by matching the impedance data to a comparable circuit for investigating material. It is a very useful investigating technique as grain boundaries and electrode effects arise in this case [39, 40]. In the Cole–Cole plot, two adjacent semicircles are seen; the first semicircle with a low-frequency region signifies grain boundary resistance and the second smaller semicircle with a high-frequency region signifies grain resistance. This usually correlates to the presence of dispersal behaviour in relaxation time.

Figure 10a–b represents the real part and imaginary part of complex impedance. For an applied frequency the complex impedance (with real, Z' and imaginary part, Z'') is given by Eq. (13),

$$Z*(\omega) = Z'(\omega) + iZ''(\omega) \tag{13}$$

$$\text{Where, } Z' = R_g/(1+\omega_g C_g R_g)^2 + R_{gb}/(1+\omega_{gb} C_{gb} R_{gb})^2 \tag{14}$$

$$\text{and } Z'' = R_g^2/[1+(R_g\omega_g C_g)^2] + R_{gb}^2/[1+(R_{gb}\omega_{gb}C_{gb})^2] \tag{15}$$

Here, R_g signifies resistance and C_g signify capacitance for the grain structure and R_{gb} and C_{gb} signify respective parameters for the grain boundary. ω_g and ω_{gb} are the frequencies at the grain semicircular peak and grain boundary semicircular peak respectively in Eqs. (14) and (15).

The resistances are computed from the Z' axis interception of circular arcs, while capacitances are obtained from the maximum altitude of the circular arcs. In each semicircle, the maximum altitude is $Z' = -Z''$; so by using this and the above equations, the capacitance for the grain and capacitance for the grain boundary can be calculated. The relaxation times for grain and grain boundary are given by Eqs. (16) and (17), respectively:

$$1/\omega_g = C_g R_g \tag{16}$$

$$1/\omega_{gb} = C_{gb} R_{gb} \tag{17}$$

Both Z' and $-Z''$ reduce as the frequency rises. The highest value of impedance is noticed for the composition with maximum Al content ($z = 0.075$). This means that the conductivity is lowered there. Figure 10 indicates the disparity of sensitive parts with the frequency of impedance for all compositions within room temperature.

For separating the contributions from grain boundary and grain, complex impedance plots or Cole–Cole plots are achieved by plotting Z' and $-Z''$. From Fig. 11, it is clear that one full semicircle is for the grain conduction and one incomplete semicircle is for the grain boundary conduction. The resistance of grain boundary is beyond the measurement scale. The Cole–Cole plots for different compositions are shown in Fig. 12, where plots of the right column are representing R_{gb} values, while plots of the left column are representing R_g values. The relaxation time constant is responsible for the semicircular arc separation. This type of behaviour of impedance spectrum involves the relaxation time distribution in the material. As time constant changes beyond 100 units, imbrications between grain resistance and grain boundary resistance are observed significantly. For grain and grain boundary contributions exhibit two semicircular arcs in the case of large particle size, while for small-sized grain a single semicircular arc (though not seen) is found [41] and the magnitude of grain contributions can affect the semicircular size. From Cole–Cole fitting process, R_g, Grain Capacitances (C_g), R_{gb}, Grain Boundary Capacitances (C_{gb}) and corresponding relaxation times (τ_g, τ_{gb}) with exponential powers are calculated and listed in Table 4. The semicircular arc at the low-frequency region expresses grain boundary parameters only and the semicircular arc at the higher frequency range expresses grain parameters. Table 4 reveals that grain resistances are increased at a higher frequency range, while grain boundary resistances are increased at the low-frequency range with Al content.

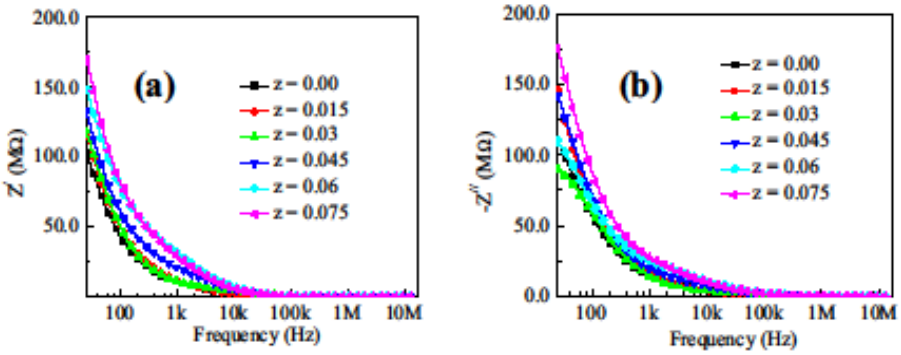

Fig. 10 Variation of a real part of impedance and b imaginary part of impedance as a function of frequency for $Ni_{0.5}Cu_{0.2}Cd_{0.3}Fe_{2-x}Al_xO_4$

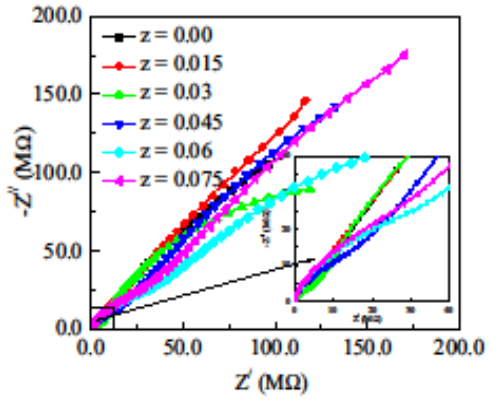

Fig. 11 Cole–Cole plots for $Ni_{0.5}Cu_{0.2}Cd_{0.3}Fe_{2-x}Al_xO_4$

This behaviour is the same for all samples of $Ni_{0.5}Cu_{0.2}Cd_{0.3}Al_xFe_{2-x}O_4$. On the site of grain boundary, imperfections control the transport nature which leads larger contribution of grain boundary in the whole resistance. Hence grains are expected to have smaller concentrations than grain boundaries and thus participate in the impedance of inter-grain regions [25].

The study of complex modulus is an effective method of investigating the electrical transport properties of the synthesized materials. It is also useful to observe other impacts that appeared in the sample with the consequence of various relaxation time constants. To ascertain, assess and explain the dynamic characteristics of electrical transport properties (i.e. conductivity, ion hopping rate, time of relaxation etc.) the complex modulus is an important technique. It can discriminate with grain boundary conduction and electrode polarization procedures. In the case of studying various nanocrystalline ceramics, the analysis of electric modulus in the light of relaxation phenomena was also stated previously by many scholars [42–44]. The performance of imperfections can be distinguishable from the electrode effect corresponding to their bulk response employing this complex modulus approach [45]. The electric modulus relates to the electric field relaxation in the substances, while the electric displacement stays constant. Generally, frequency-dependent complex electric modulus M^* can show important features like a broad unbalanced peak in the imaginary part and a sigmoidal performance in the real part [46].

For Ni-Cu-Cd-Al ferrite nanoparticles, the variation of frequency-dependent M' (real part) and M''(imaginary part) of complex electric modulus has been presented in Figs. 13 and 14, respectively. The M' is very low at lower frequencies and after a particular range of frequency, it increases gradually and reaches its saturation value. The saturation of M' values detected at the high-frequency side probably owing to the release of space charge polarization [47]. There appears the low value of M' in lower frequency leading the conduction process due to extended range motion of charge carriers and the electrode polarization contribution in the material [48]. Besides, the M' increase with the rise in Al content implies the polarization effects become remarkably lower, i.e. reduces dielectric losses.

Figure 14 displays the M'' of electric modulus versus frequency at room temperature. It is seen from Fig. 14 that M'' displays very lower values at lower frequencies and after a frequency of about 10 kHz, it increases rapidly and attains maximum for all the

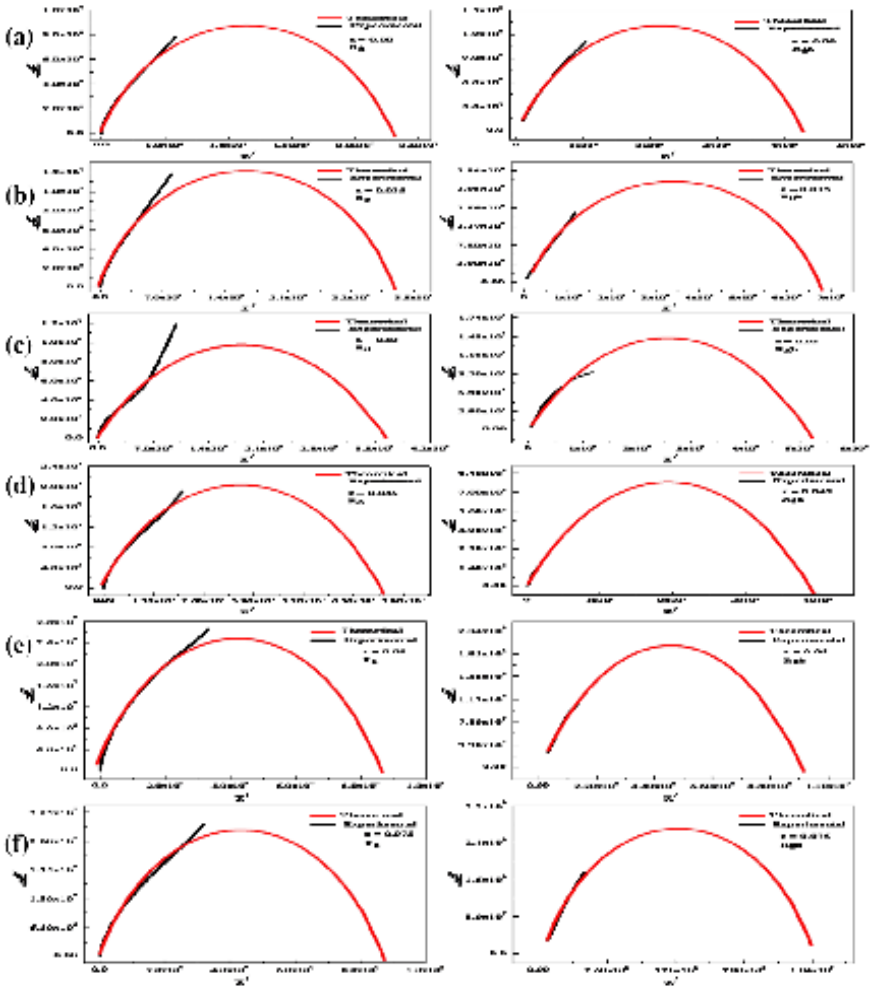

Fig. 12 Cole–Cole fitting for grain (left) and grain boundary (right) parameter of $Ni_{0.5}Cu_{0.2}Cd_{0.3}Fe_{2-z}Al_zO_4$ **a** without Al content, **b** with Al content 0.015, **c** with Al content 0.030, **d** with Al content 0.045, **e** with Al content 0.060 and **f** with Al content 0.075

Table 4 Grain and Grain boundary parameters for $Ni_{0.5}Cu_{0.2}Cd_{0.3}Fe_{2-z}Al_zO_4$ ferrite nanoparticles annealed at 700 °C temperature

Al content (z)	R_g (MΩ)	R_{gb} (MΩ)	τ_g (ns)	τ_{gb} (ns)	α_g	α_{gb}
0.00	30.03	500	100	10	0.7	0.7
0.015	35.01	692	100	10	0.8	0.8
0.030	40.2	820	100	10	0.5	0.6
0.045	81	4020	100	10	0.6	0.5
0.060	91	1000	100	100	0.7	0.5
0.075	100	980	100	100	0.7	0.7

samples. It also observed that M'' shifts the location of the peak towards the higher frequency side as the Al content increased. This offers clear information regarding processes of charge transport such as the

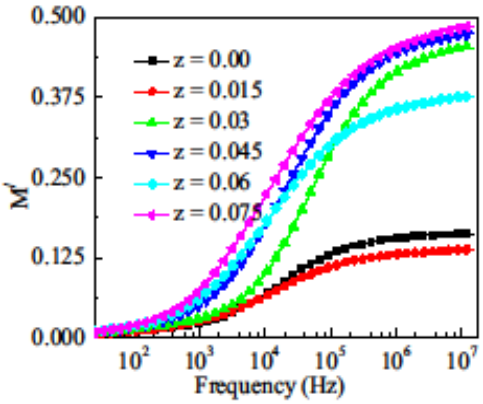

Fig. 13 Variation in M′ of electric modulus of $Ni_{0.5}Cu_{0.2}Cd_{0.3}Fe_{2-x}Al_xO_4$ as a function of frequency

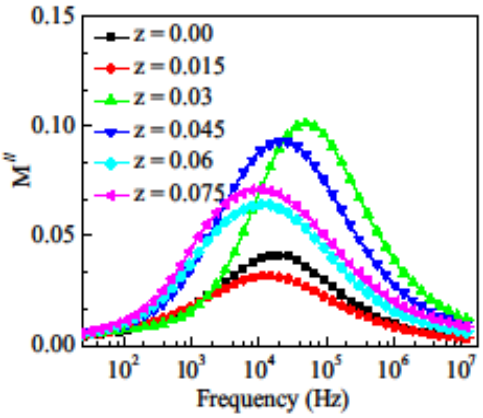

Fig. 14 Variation in M″ of electric modulus of $Ni_{0.5}Cu_{0.2}Cd_{0.3}Fe_{2-x}Al_xO_4$ as a function of frequency

system of electrical transport, ion dynamics and conductivity relaxation with frequency. The peak indicates the separation between long-range and short-range hopping mechanisms due to electron transfer. Charge carriers are capable to move long distances in frequency region (lower frequency) below the peak maximum, whereas they are confined in potential wells and movable over short distances in the high-frequency side at above the peak maximum [49]. This type of modulus analysis suggests us a composition-dependent hopping like the mechanism of conduction in the electrical system. The widening of the peak indicates non-Debye relaxation in the material. The existence of a peak in the spectrum of modulus provides also a clear signal of relaxation of conductivity. The most feasible relaxation time (τ) can be calculated from the maximum frequency (f_{max}) corresponding to the peak maximum in M″ versus frequency curve provided the condition $2\pi f_{max} \times \tau = 1$ is satisfied.

We can distinguish the relaxation of grains and grain boundaries by analysing the electric modulus plot (M'' vs. M' spectra) shown in Fig. 15. Typical depressed semicircular arcs with no intersecting of peaks have been seen for our synthesized samples, which suggest that the studied ceramic nanomaterials follow the non-Debye behaviour of relaxation time. It is also revealed that the complex modulus plot shows only single semicircles with no secondary circles that suggest the Al-substituted Ni–Cu–Cd ferrites are single phase which also validates the results of XRD data. The diameter of semicircles increases with the rise of Al content in the present series.

4 Conclusions

In this research, the technique sol–gel auto-combustion has been used for the successful synthesis of nanocrystalline Al-substituted Ni–Cu–Cd ceramics. XRD study reveals the single-phase homogeneous cubic spinel structure of the compositions. The lattice constant is found to be decreased linearly with Al^{3+} substitution. The D_{311}, D_{FESEM} and $D_{W\text{-}H}$ have been computed from the Scherrer's equation, FESEM observations and Williamson–Hall plot are found in

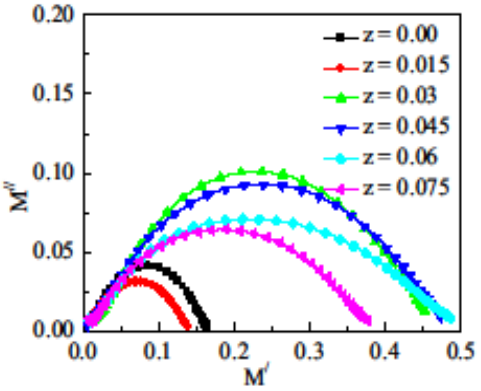

Fig. 15 M″ vs. M′ for $Ni_{0.5}Cu_{0.2}Cd_{0.3}Fe_{2-x}Al_xO_4$

the nanoscale range (16–21) nm, (99–46) nm and (22–16) nm, respectively. In all D_{311}, D_{FESEM} and $D_{W\text{-}H}$ are found to decrease with increasing Al content. The normal dielectric behaviours have been observed in all the samples. tanδ decreases remarkably with increasing Al content. Electric modulus and complex impedance studies reveal the predominance of grains boundary resistance over grains resistance in the materials. The complex impedance spectra contain semicircles with contributions of grain effects and grain boundary effects (R_g, R_{gb}). Both R_g and R_{gb} increased with increasing Al content. The modulus plots show non-Debye actions and are distorted about maximum peak and peaks are significantly broader on the left and right sides of maxima which suggest materials dielectric relaxation. The decrease in the values of Z' and Z'' as well as σ_{ac} with rising frequency indicates that the conductivity of the investigated ferrites rises with frequency. It was also observed that with Al content at higher frequency region conductivity decrease more which interprets intrinsic grain to have high resistivity. The obtained findings are beneficial for researchers and technologists to fabricate various devices for multifunctional purposes as an alternate use of Cd for Zn.

Declarations

Conflict of interest The authors declare that they have no known competing financial interests or personal relationships that could have appeared to influence the work reported in this paper. Also, there is no conflict of interest for this submission.

References

1. S. Odenbach, K. H. J. Buschow (Eds.) (2006) Handbook of magnetic materials, vol. 16, Amsterdam, North-Holland, p. 127
2. P. Tartaj, M.D.D. Morales, S. Veintemillas-Verdaguer, T. Gonzalez-Carreno, C.J. Serna, J. Phys. D Appl. Phys. **36**, R182 (2003)
3. M. Faraji, Y. Yamini, M. Rezaee, J. Iran. Chem. Soc. **7**, 1 (2010)
4. C.M. Niemeyer, Angew. Chem. Int. Ed. **40**, 4128 (2001)
5. D.K. Pradhan, P. Misra, V.S. Puli, S. Sahoo, D.K. Pradhan, R.S. Katiyar, J. Appl. Phys. **115**, 243904 (2014)
6. A.A. Sattar, H.M. El-Sayed, M.M. El-Tabey, J. Mater. Sci. **40**, 4873 (2005)
7. I. Maghsoudi, H. Shokrollahi, M.J. Hadianfard, J. Amighian, Powder Technol. **235**, 110 (2013)
8. I.H. Gul, E. Pervaiz, Mater. Res. Bull. **47**, 1353 (2012)
9. V. Chaudhari, S.E. Shirsath, M.L. Mane, R.H. Kadam, S.B. Shelke, D.R. Mane, J. Alloys Compd. **549**, 213–220 (2013)
10. B.B. Patil, A.D. Pawar, D.B. Bhosale, J.S. Ghodake, J.B. Thorat, T.J. Shinde, J. Nanostruct. Chem. **9**, 119–128 (2019)
11. B.D. Cullity, *Elements of X-Ray Diffraction* (Addison-Wesley, London, 1959)
12. M.Y. Lodhi, K. Mahmood, A. Mahmood, H. Malik, M.F. Warsi, I. Shakir, M. Asghar, M.A. Khan, Curr. Appl. Phys. **14**(5), 716–720 (2014)
13. D.M. Jnaneshwara, D.N. Avadhani, B. Daruka Prasad, H. Nagabhushana, B. M. Nagabhushana, S.C. Sharma, S.C. Prashantha, C. Shivakumara (2014) Spectrochim. Acta Mol. Biomol. Spectrosc. 132: 256–262
14. H. Anwar, A. Maqsood, J. Supercond. Nov. Magn. **25**(6), 1913–1920 (2012)
15. S. Ikram, J. Jacob, M.I. Arshad, K. Mahmood, A. Ali, N. Sabir, N. Amin, S. Hussain, Ceram. Int. **45**, 119–128 (2019)
16. L. Kumar, P. Kumar, A. Narayan, M. Kar, Rietveld analysis of XRD patterns of different sizes of nanocrystalline cobalt ferrite. Int. Nano Lett. **3**(1), 1–12 (2013)
17. M. Arifuzzaman, M.B. Hossen, Results Phys. **16**, 102824 (2020)
18. L. Kumar, M. Kar, J. Exp. Nanosci. **9**(4), 362–374 (2014)
19. M.I. Mendelson, Average grain size in polycrystalline ceramics. J. Am. Ceram. Soc. **52**(8), 443–446 (1969)
20. T.J. Shinde, A.B. Gadkari, P.N. Vasambekar, J. Mater. Sci. Mater. Electron. **21**(2), 120–124 (2010)
21. M.K. Anupama, N. Srinatha, S. Matteppanavar, B. Angadia, B. Sahoo, B. Rudraswamy, Ceram. Int. **44**(5), 4946–4954 (2018)
22. A.K.M. Akhter Hossain, L.M. Rahman, J. Magn. Magn. Mat. **323**, 1954–1962 (2011)
23. P.B. Belavi, G.N. Chavan, B.K. Bammannavar, L.R. Naik, R.K. Kotnala, J. Mat. Chem. Phys. **132**, 138–144 (2012)
24. H.S.C. O'Neill, A. Navrotsky, Am. Miner. **68**, 181–194 (1983)
25. O.M. Hemeda, M.M. Barakat, J. Magn. Magn. Mater. **223**, 127 (2001)
26. D.R. Patil, B.K. Chougule, J. Mat. Chem. Phys. **117**, 35 (2009)
27. S. Dagar, A. Hooda, S. Khasa, M. Malik, J. Alloy. Compd. **806**, 737–752 (2019)
28. J.C. Maxwell, *Electricity and Magnetism*, vol. 2 (Oxford University Press, New York, 1973), p. 828
29. K.W. Wagner, Ann. Phys. **345**, 817–855 (1913)
30. C.G. Koops, Phys. Rev. **83**, 121 (1951)

31. L.T. Rabinkin, Z.I. Novikova, Acad. Nauk. USSR Minsk. 146 (1960)
32. N. Popandan, P. Balay, A. Narayansamy, J. Phys. Condens. Matter. **14**, 3221 (2002)
33. M. Hashim, S.E. Shirsath, S. Kumar, R. Kumar, A.S. Roy, J. Shah, R.K. Kotnala, J. Alloy. Compd. **549**, 348 (2013)
34. A. Thakura, P. Mathura, M. Singh, J. Phys. Chem. Solids **68**, 378 (2007)
35. M.L.S. Teo, L.B. Kong, Z.W. Li, G.Q. Lin, Y.B. Gan, J. Alloys Compd. **459**, 567 (2008)
36. D. Ravinder, K. Vijayakumar, Bull. Mater. Sci. **24**(5), 505 (2001)
37. V.L. Mathe, K.K. Patankar, M.B. Kothale, S.B. Kulakarni, P.B. Joshi, S.A. Patil, Pramana J. Phys. **58**(5 & 6), 1105 (2002)
38. M. Hashim, S. Kumar, S. Ali, B. H. Koo, H. Chung, R. Kumar (2012) J. Alloys Compd. 511: 107
39. B. K. Kumar, G. P. Srivastava, P. Kishen, Proc. ICF-5(Bombay) (1988) 233.
40. M.A. Ahmed, M.K.E. Nimar, A. Tawfik, A.M.E. Hasab, J. Magn. Magn. Mater. **98**, 33 (1991)
41. R.C. Kambale, P.A. Shaikh, C.H. Bhosale, K.Y. Rajpure, Y.D. Kolekar, Smart Mater. Struct. **18**(11), 115028 (2009)
42. J. Liu, C.G. Duan, W.G. Yin, J. Chem. Phys. **119**, 2812 (2003)
43. C. León, M.L. Lucía, J. Santamaría, Phys. Rev. B **55**, 882 (1997)
44. R. Richert, H. Wagner, Solid State Ionics **105**, 167 (1998)
45. N. G. McCru, B. E. Read, G. Williams, Wiley, New York (1967).
46. A. Marsha, S.N. Chowdhury, K. Prashad, R.N.P. Choudhary, Phys. B **406**, 3279 (2011)
47. I. Ali, M.U. Islam, M.N. Ashiq, I. Shakir, N. Karamat, M. Ishaque, M.N. Akhtar, H.M. Khan, M. Irfan, M.A. Khan, Ceram. Int. **41**, 8748 (2015)
48. B.V.R. Chowdari, R. Gopalkrishnan, Solid State Ionics **23**, 225 (1987)
49. M.F. Mahmood, M.B. Hossen, J. Mater. Sci. Mater. Electron. **32**, 14248–14273 (2021)